

**NASA CR-54124**

*e.1*

LOAN COPY: RETURN  
AFWL (WLIL-2)  
KIRTLAND AFB, N M

0062448



TECH LIBRARY KAFB, NM

# **INVESTIGATION OF AN MGD POWER GENERATOR DUCT**

by

**Fredrick H. Shair**

prepared for

**NATIONAL AERONAUTICS AND SPACE ADMINISTRATION**

**Contract NAS 3-4103**

**SPACE SCIENCES LABORATORY**  
**GENERAL  ELECTRIC**  
**MISSILE AND SPACE DIVISION**



## NOTICE

This report was prepared as an account of Government sponsored work. Neither the United States, nor the National Aeronautics and Space Administration (NASA), nor any person acting on behalf of NASA:

- A.) Makes any warranty or representation, expressed or implied, with respect to the accuracy, completeness, or usefulness of the information contained in this report, or that the use of any information, apparatus, method, or process disclosed in this report may not infringe privately owned rights; or
- B.) Assumes any liabilities with respect to the use of, or for damages resulting from the use of any information, apparatus, method or process disclosed in this report.

As used above, "person acting on behalf of NASA" includes any employee or contractor of NASA, or employee of such contractor of NASA, or employee of such contractor prepares, disseminates, or provides access to, any information pursuant to his employment or contract with NASA, or his employment with such contractor.

Requests for copies of this report should be referred to

National Aeronautics and Space Administration  
Office of Scientific and Technical Information  
Attention: AFSS-A  
Washington, D. C. 20546



NASA CR-54124

SUMMARY REPORT  
INVESTIGATION OF AN MGD POWER  
GENERATION DUCT

by

Fredrick H. Shair

prepared for

NATIONAL AERONAUTICS AND SPACE ADMINISTRATION

January 15, 1965

CONTRACT NAS 3-4103

Technical Management

NASA Lewis Research Center

Spacecraft Technology Division

Cleveland, Ohio

N. J. Stevens

GENERAL ELECTRIC COMPANY  
Missile and Space Division  
Space Sciences Laboratory  
P.O. Box 8555, Philadelphia, Pa., 19101

## ABSTRACT

An electron beam and externally applied electric fields were used to increase the plasma electrical conductivity (above the neutral particle temperature Saha equilibrium value) in an MGD generator while maintaining a gas static temperature  $\sim 1500^{\circ}\text{K}$ ; the static pressure was  $\sim 1\frac{1}{2}$  atm. Preliminary experiments were conducted in pure argon, in argon seeded with cesium, and in argon seeded with mercury (metastable mixture). Electron densities were monitored at two positions (on either side of the magnetic field) by means of a 60 KMC microwave interferometer. The duct cross-section was uniform at 1 cm x 3 cm. Based on these preliminary tests the following results were obtained.

1. In the argon-cesium plasma electrical conductivities of  $\sim 12$  mhos/m. were obtained at the electron beam port and the electron "disappearance rate" closely follows a two body recombination expression with the recombination coefficient  $\sim 1.5 \times 10^{10} \text{ cm}^3/\text{sec}$ . Electrical Conductivities were between 50 and 100 times that based upon the neutral gas temperature.
2. In the argon-mercury experiment an intense discharge, created within the magnetic field region, produced several orders of magnitude increase in electron density upstream; a crude calculation shows that this may be caused by photoionization.

## TABLE OF CONTENTS

<u>Section</u>		<u>Page</u>
I	<u>SUMMARY</u>	1
II	<u>INTRODUCTION</u>	2
III	<u>DESCRIPTION OF EXPERIMENTAL FACILITY</u>	4
	A. GENERAL DESCRIPTION OF M-4 MGD FACILITY	4
	B. MOLYBDENUM MESH CORE HEATER	11
	C. COLD CATHODE ELECTRON BEAM	17
	D. MICROWAVE INTERFEROMETER	44
	E. TEST SECTION	48
IV	<u>EXPERIMENTAL RESULTS</u>	52
	A. ARGON SEEDED WITH CESIUM	52
	B. ARGON SEEDED WITH MERCURY (METASTABLE MIXTURE)	63
V	<u>THEORETICAL ANALYSIS</u>	68
	A. COMPATIBILITY EQUATION FOR NON-EQUILIBRIUM IONIZATION	68
VI	<u>CONCLUSIONS</u>	77
VII	<u>BIBLIOGRAPHY</u>	79
VIII	<u>APPENDICES</u>	81
	A. ARGON PURITY	81
	B. NOZZLE COMPOSITION	82
	C. PUMPING SPEEDS REQUIRED FOR ELECTRON BEAM DIFFERENTIAL PUMPING SYSTEM	83
	ACKNOWLEDGMENT	87

## I. SUMMARY

An electron beam and externally applied electric fields were used to increase the plasma electrical conductivity (above the neutral particle temperature Saha equilibrium value) in an MGD generator while maintaining a static gas temperature  $\sim 1500^{\circ}\text{K}$ .

Between 60 and 90 grams/second of argon were heated to near  $1500^{\circ}\text{K}$  by means of a compact molybdenum mesh core heater. Gas velocities ranged up to  $5 \times 10^4$  cm/second. The magnetic field ranged up to 24,000 gauss. A dense pure alumina test section was developed which continually withstood thermal shock and in which no visual attack occurred from the cesium and mercury vapors. The duct cross-section was uniform at 1 cm x 3 cm. Cooling techniques were developed to permit a 0.25 mil thick aluminum window to be used with a 20-m.a. 50-K.v. electron beam. Electron densities were monitored at two positions (on either sides of the magnetic field) by means of a 60 KMC microwave system.

Preliminary experiments were conducted in pure argon, in argon seeded with cesium, and in argon seeded with mercury (metastable mixture). Based upon these preliminary tests the following results were obtained:

1. In the argon-cesium plasma electrical conductivities of  $\sim 12$  mhos/m. were obtained at the electron beam injection port. During this test, both the electron beam and externally applied electric fields were used to pre-ionize. The power input from the electron beam was  $\sim 5$  watts whereas the power input from the applied electric fields was  $\sim 360$  watts when the discharge was established. At a distance of 19 cm. downstream of the electron beam port an electron density  $\sim 3.0 \times 10^{12}$  electrons/cm<sup>3</sup> was measured which corresponds to an electrical conductivity of  $\sim 5$  mhos/m. At a distance 77 cm. downstream of the electron beam port the electron density, (inferred from the applied electric field voltage-current values), was  $\sim 2.5 \times 10^{12}$  electrons/cm<sup>3</sup> which corresponds to an electrical conductivity of  $\sim 3$  mhos/m. At a distance of 157 cm. downstream of the electron beam injection point an electron density was measured  $\sim 1.3 \times 10^{12}$  electrons/cm<sup>3</sup> which corresponds to an electrical conductivity of  $\sim 2$  mhos/m. The total electron "disappearance rate" closely follows a two-body volume recombination expression with the recombinations coefficient  $\sim 1.5 \times 10^{-10}$  cm<sup>3</sup>/sec. The electrical conductivity at the electron beam port (obtained from extrapolation of the "disappearance rate" curve) was  $\sim 6$  mhos/m; this value is in fair agreement with the 12 mhos/m. calculated from the number and energy of electrons entering the duct. The net result of the pre-ionization was to create electrical conductivities within the test section which were between 50 and 100 times the Saha equilibrium value determined from the neutral particle temperature.

With seeding and with both pre-ionization techniques employed, open circuit voltages were increased from 1.8 volts to 7.5 volts, or from 6% to 25% of the (UB1) value. When the electron beam was on, open circuit voltages increased from 4.8 volts to 7.5 volts; this was an increase from 16% to 25% of the (UB1) value.

2. In the argon-mercury experiment an intense discharge (created within the magnetic field region) produced an electron density  $\sim 10^{12}$  electron/cm<sup>3</sup>. This electron density was observed at the microwave port which was  $\sim 55$  cm. upstream of the discharge. This electron density value is an 8 order of magnitude increase over the Saha equilibrium value at  $T_{\text{gas}} \sim 1080^\circ\text{K}$ ; a crude calculation shows that photoionization may be the main mechanism.

## II. INTRODUCTION

In order to operate a closed loop MGD generator with high power density at temperatures compatible with near-future nuclear reactors and with existing "high temperature materials," the electrical conductivity of the plasma must be greatly increased within the generator while maintaining a gas temperature  $\sim 1500^{\circ}\text{K}$ . The plasma electrical conductivity can be greatly increased if a non-equilibrium condition of the electrons can be established; in a non-equilibrium condition, the electron density is greater than that predicted by the Saha equation based upon the neutral particle temperature. Various techniques may be employed to create non-equilibrium ionization (see References 4, 25, and 26).

The purpose of the present study is to make use of electron beams, metastables mixtures, and high pressure glow discharges, to increase the plasma electrical conductivity while maintaining a neutral particle temperature  $\sim 1500^{\circ}\text{K}$ . Between 60 and 90 grams/second of argon were heated to near  $1500^{\circ}\text{K}$  by means of a compact molybdenum mesh core heater. Test times lasted up to 1 hour. Gas velocities ranged up to  $5 \times 10^4$  cm/second in a constant area duct 1 cm x 3 cm. The magnetic field ranged up to 24,000 gauss. Primary goals to be achieved consisted of increasing the plasma electrical conductivity, to  $\sim 10$  mhos/m., with one of the previously mentioned non-equilibrium techniques, and increasing the performance of the MGD generator.



### III. DESCRIPTION OF EXPERIMENTAL FACILITY

#### A. GENERAL DESCRIPTION OF THE M-4 MGD FACILITY

The M-4 MGD Facility consists mainly of the following systems:

1. The Gas Supply System
2. The Gas Heater System
3. The Nozzle and Plenum Chamber
4. The Seed Injection System
5. The Electron Beam System
6. The MGD Test Section
7. The 60 KMC Microwave System
8. The L-158 Magnet
9. Impurity Recording System

A 24,750 ft.<sup>3</sup> bulk supply of high purity argon (see Appendix A) allows full scale runs lasting up to an hour. The flow rate is adequately controlled by means of a Matheson Dual Stage Model F62 Regulator. Argon flow rates, ranging from 60 to 90 grams/second, are measured by means of a Brooks Type 12-1110-6111 Rotameter with a tube size R12M-127-1. The argon is heated to near 800°K by means of two pre-heaters. (The pre-heaters are stainless steel tubes packed with copper filling and heated externally with band heaters.) An electrical resistance heater (discussed below) is then used to raise the argon temperature up to near 1600°K. A motor driven syringe unit is used to provide a known injection rate of seed into the argon stream. Syringes made of glass or stainless steel had to be replaced after each injection and sometimes failed to operate. Polypropylene syringes (costing less than a dollar a piece) have not been visually attacked by the cesium. The seeded argon then passes into a plenum chamber and then through a nozzle. A molybdenum screen is used to provide uniform upstream conditions and to assist in the mixing of the cesium vapor. After 10 runs (each lasting about one hour) a slight amount of cesium attack of the alumina nozzle was visible. However, this did not impair its use. The specific composition of the alumina is presented below in Appendix B. For the subsonic flow, the nozzle is used as a Venturi meter, thus providing an independent check on the mass flow rate into the MGD test section. The generator channel area is constant with dimensions 1 cm x 3 cm. Electron beam injection is ~ 22 cm. downstream of the nozzle throat. (The electron beam is described in detail below.) Pertinent distances are presented in Table I.

TABLE I

Position	Distance, cm
1. Nozzle Throat to Electron Beam Port	22
2. Electron Beam Port to 1st Microwave Station	19
3. Electron Beam Port to 1st Pre-Ionization Electrode	77
4. Electron Beam Port to 2nd Pre-Ionization Electrode	79.5
5. Electron Beam Port to 3rd Pre-Ionization Electrode	82
6. Electron Beam Port to 1st Generator Electrode (Generator electrodes spaced 2.5 cm apart)	84.5
7. Electron Beam Port to 2nd Microwave Station	157

After leaving the nozzle region, the plasma passes by the first microwave station, passes through the test section where a transverse magnetic field exists, and then passes by the second microwave station and is exhausted. The microwave system is discussed below. For convenience, a sketch of the M-4 MGD Facility is shown in Figure 1. A photograph of the facility is shown in Figure 2. The magnet has 6" x 13" rectangular pole faces and a 2" gap. The calibration curve for this magnet is shown in Figure 3. It can be operated for a couple of minutes at 100% overload to create magnetic fields near 29 kilogauss. Flux maps for nineteen and twenty kilogauss are shown in Figure 4. Static and dynamic pressures throughout the nozzle and test section are measured by means of molybdenum probes attached to a mercury manometer bank. Temperatures throughout the facility are recorded on two Dual Pen Minneapolis Honeywell Elektronik 17 Recorders and a General Electric 24 Multipoint Recorder. Shielded Pt/Pt-10% Rh thermocouples measure the neutral particle temperature (see Figure 5). Oxygen and water vapor impurities can be monitored with Beckman Analyzers.

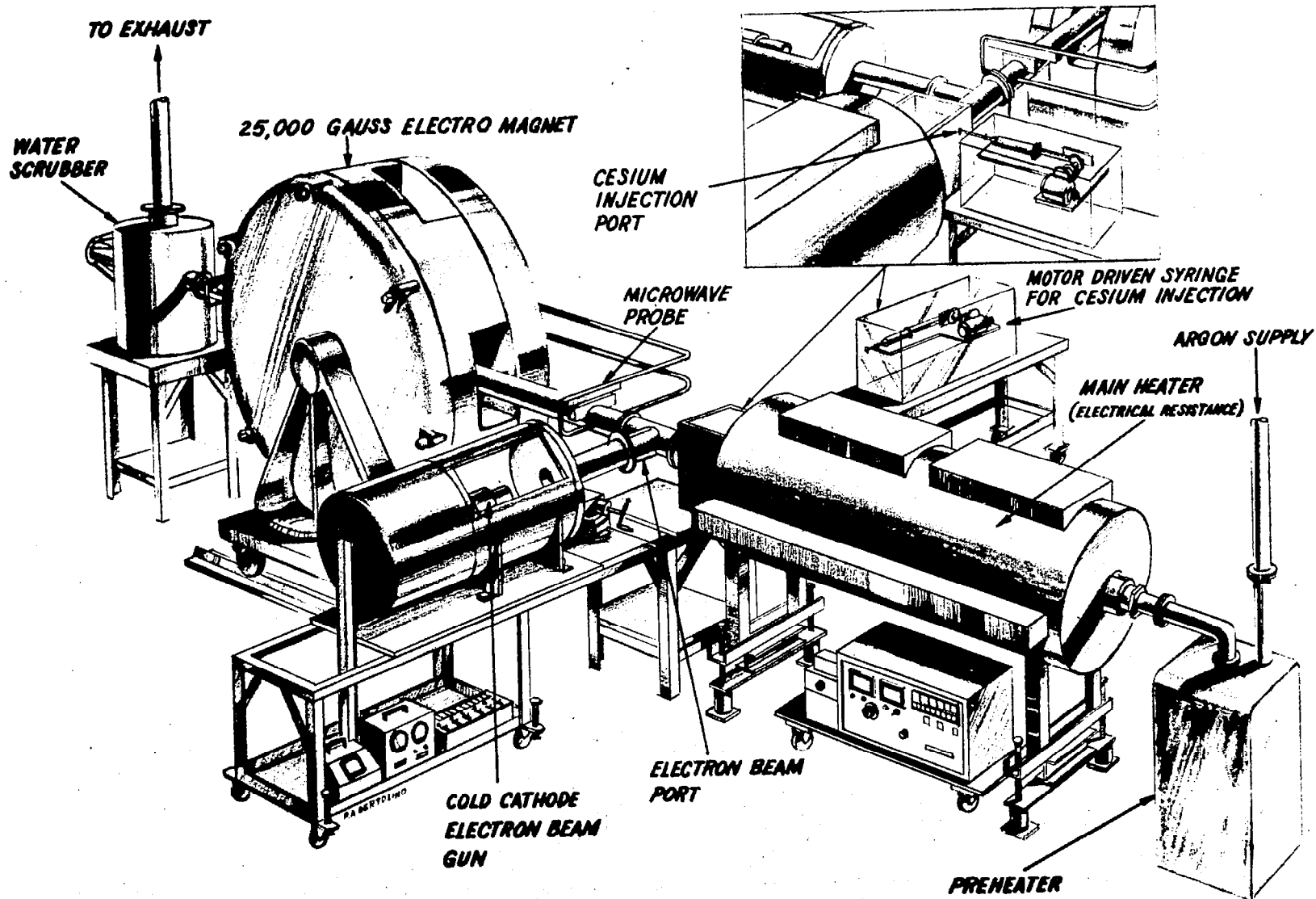


Figure 1. Seeded Gas MGD Facility

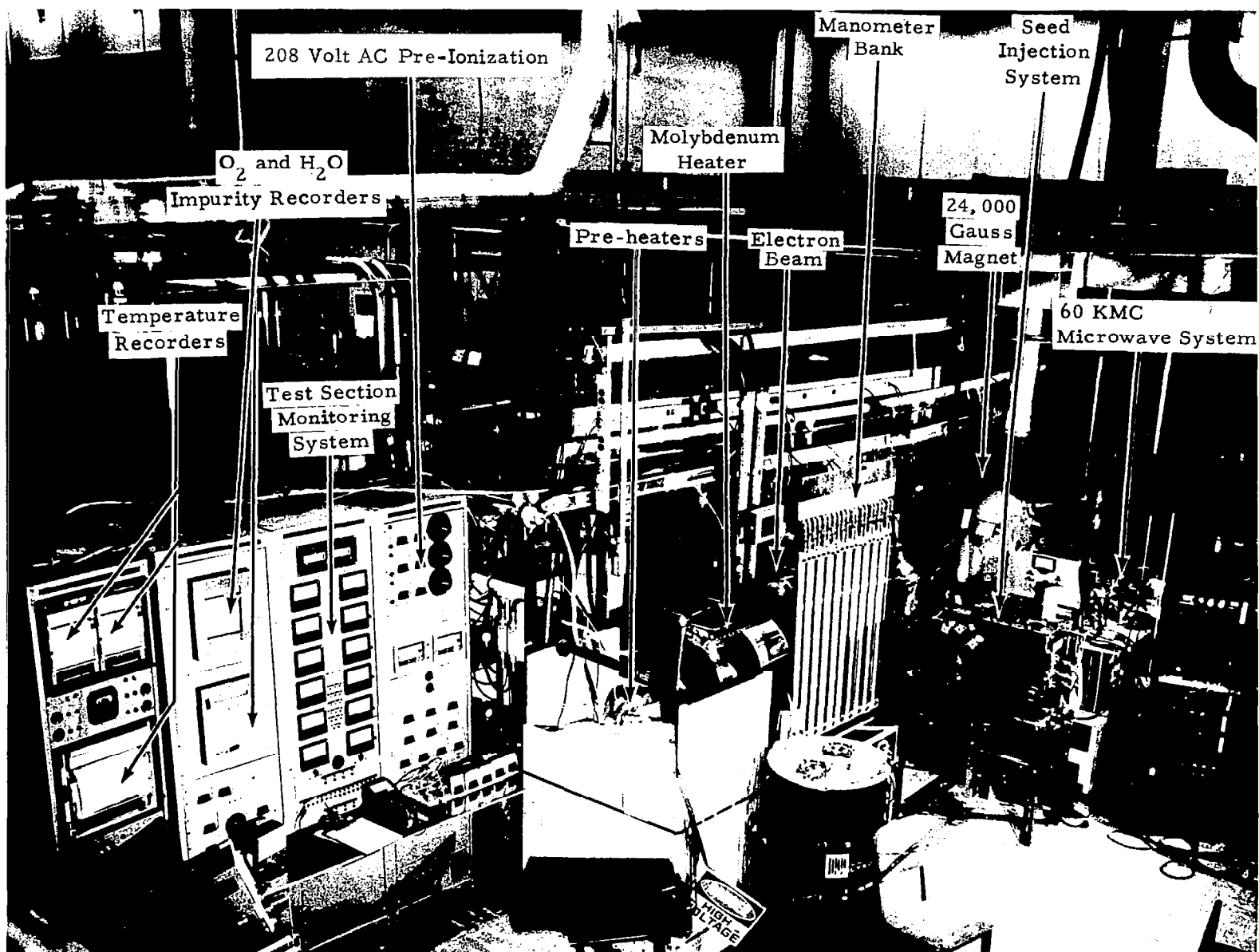


Figure 2. G.E. Seeded Gas MHD Power Generator

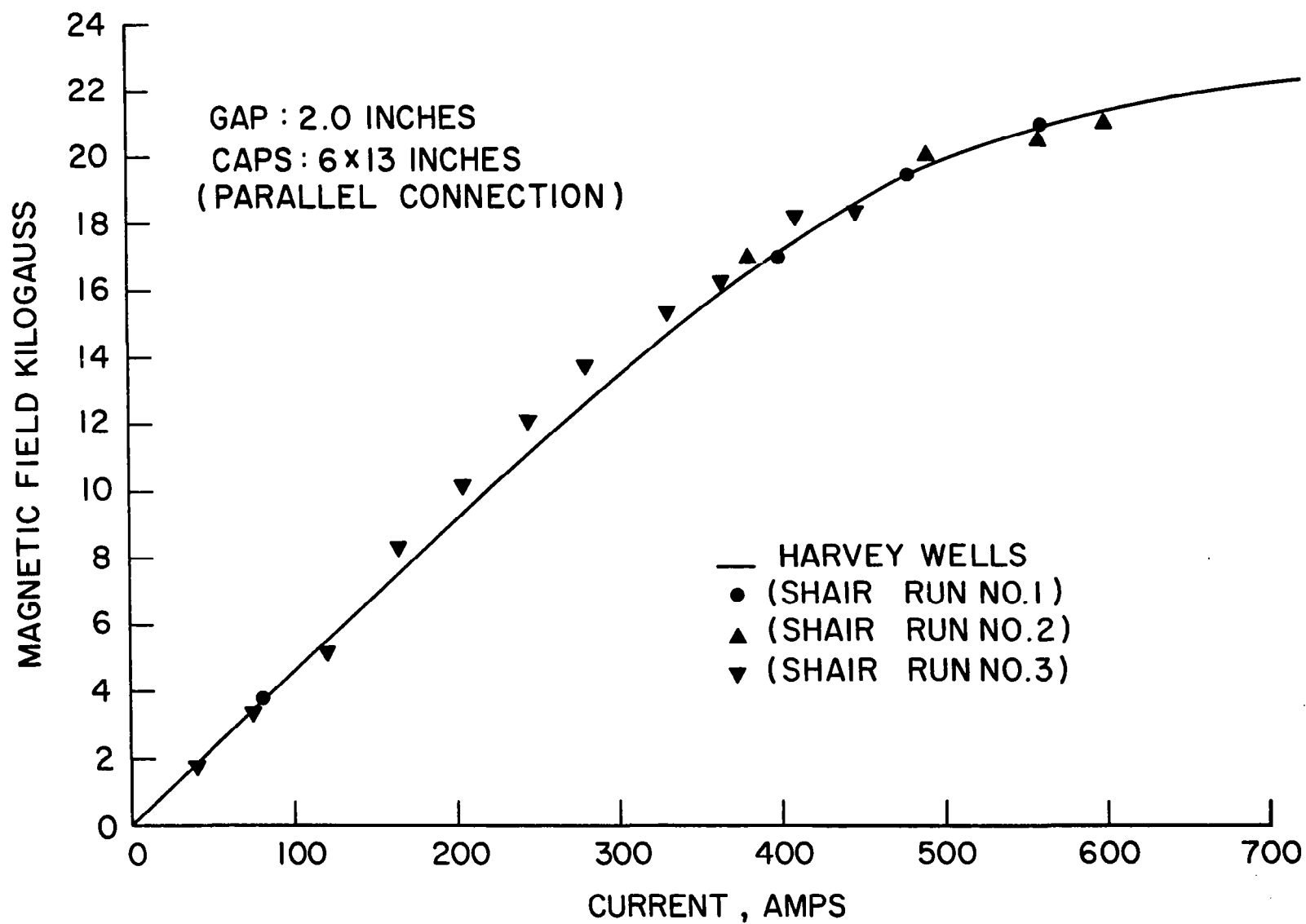


Figure 3. Calibration Curve for L-158 Magnet

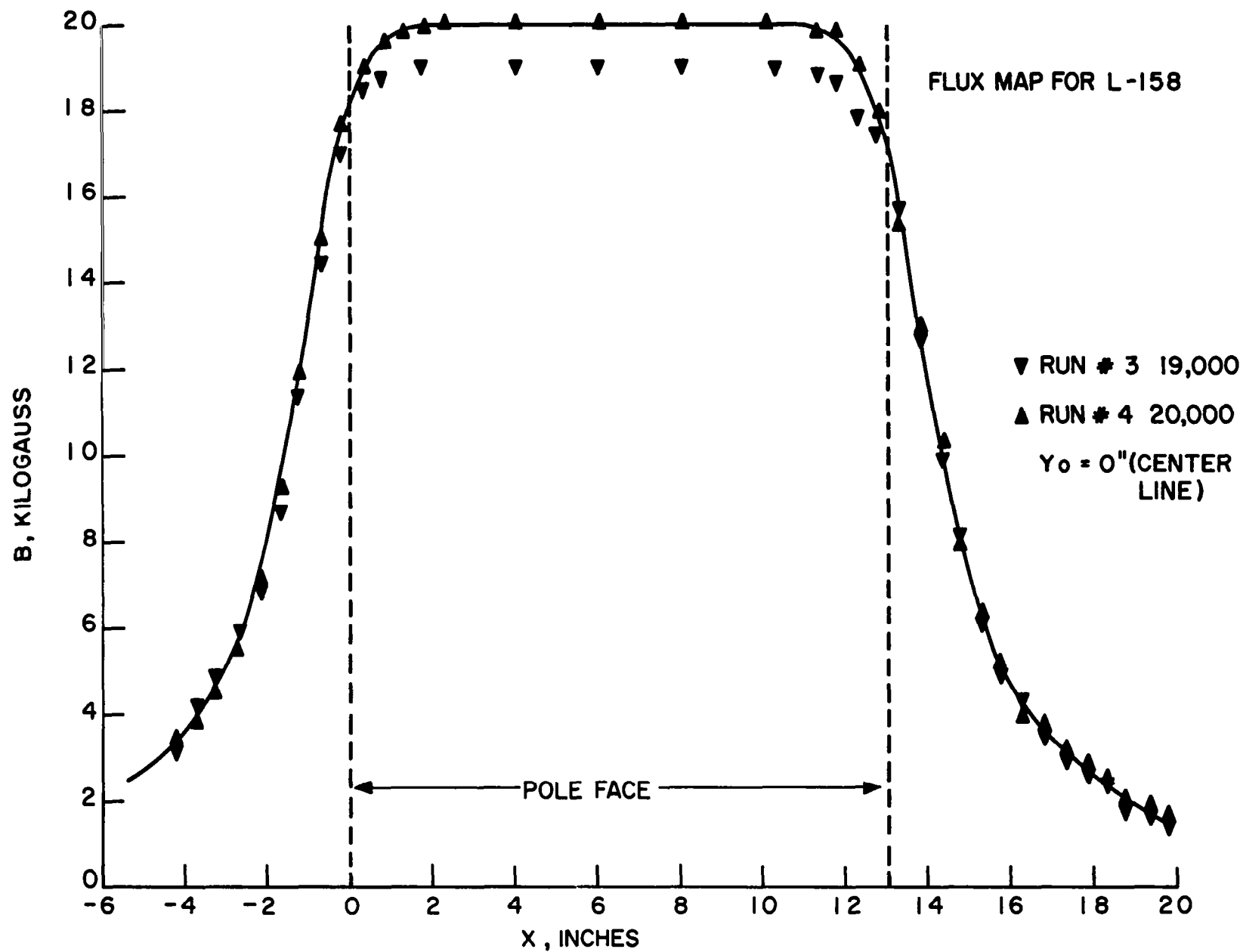
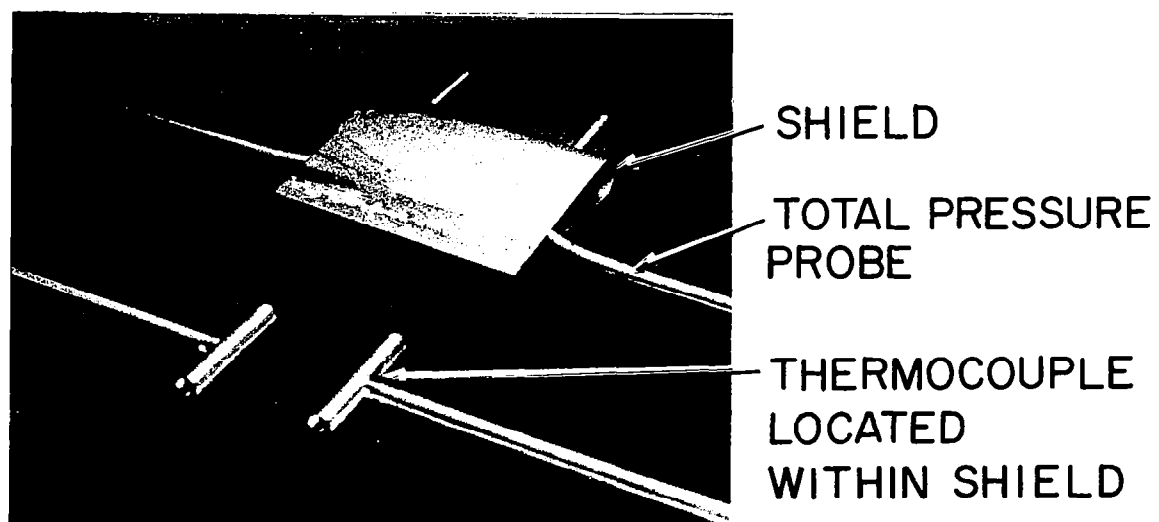


Figure 4. Typical Flux Map for L-158 Magnet



**Figure 5. Shielded PT/PT - 10% Rh Thermocouples Behind Total Pressure Probes**

## B. MOLYBDENUM MESH CORE HEATER

This compact heater has an electrical resistance element which is a molybdenum mesh core through which the argon is forced to flow. A 6 inch by 300 inch roll of molybdenum screen (20 mesh with 7 mil wire) was used to construct a laminated mat 50 inches long and 6 inches wide (see Figure 6); this mat was then rolled tightly along the 6 inch length to form the heater core. Each end of the core was inserted between pre-cut sections of a molybdenum bar which were then welded together in an inert atmosphere. The mesh core, next to each molybdenum bar, was reinforced with 200 feet of 10 mil molybdenum wire. The mesh core was then pulled through a dense alumina tube with an I.D. of 1-1/2 inches. This assembly was in turn placed within a nickel tube which was lined with a porous alumina tube. The electrical leads consist of molybdenum rods which extend through typical pressure fittings and fit into holes (drilled and tapped) within the molybdenum bars. The external end of each molybdenum rod is cooled by means of a water-cooled copper plate. The assembled heater is shown in Figure 7. A bellows expansion is used to absorb variations in length due to thermal expansions and contractions. The power input to the mesh heater is controlled by means of a saturable core reactor and a step-down transformer. In this heater, the area available for heat transfer,  $A$ , is about 250 square feet per cubic foot of heater volume; this value is comparable to that given for "compact" exchangers (see Reference 1). The turbulence created by the mesh core also increases the heat transfer coefficient,  $h$ , by at least a factor of 3, (see Reference 2). Values of  $hA$  in this heater were increased by around a factor of 24 as compared to the same size hollow tube heated externally. The operating characteristics of this particular heater are shown in Figure 8. The experimental scatter in these curves is due primarily to variations in the flow rate of argon. Calculations of the heat conduction losses from a hollow cylinder show this mechanism to be the main source of energy loss; although the heater element is operated at temperatures well in excess of 1000°K, radiation losses in a mesh core heater are negligible. To date, this heater has been operated during 24 experiments, each lasting around an hour. Typical exist argon temperature time curves are shown in Figure 9.

In conclusion, the mesh core heater provides six essential features:

1. The product of the heat transfer coefficient times the area available for heat transfer, can be made extremely large as compared to even "compact" heaters.
2. Thermal shock damage can be eliminated.
3. Energy losses due to conduction and radiation can be minimized.



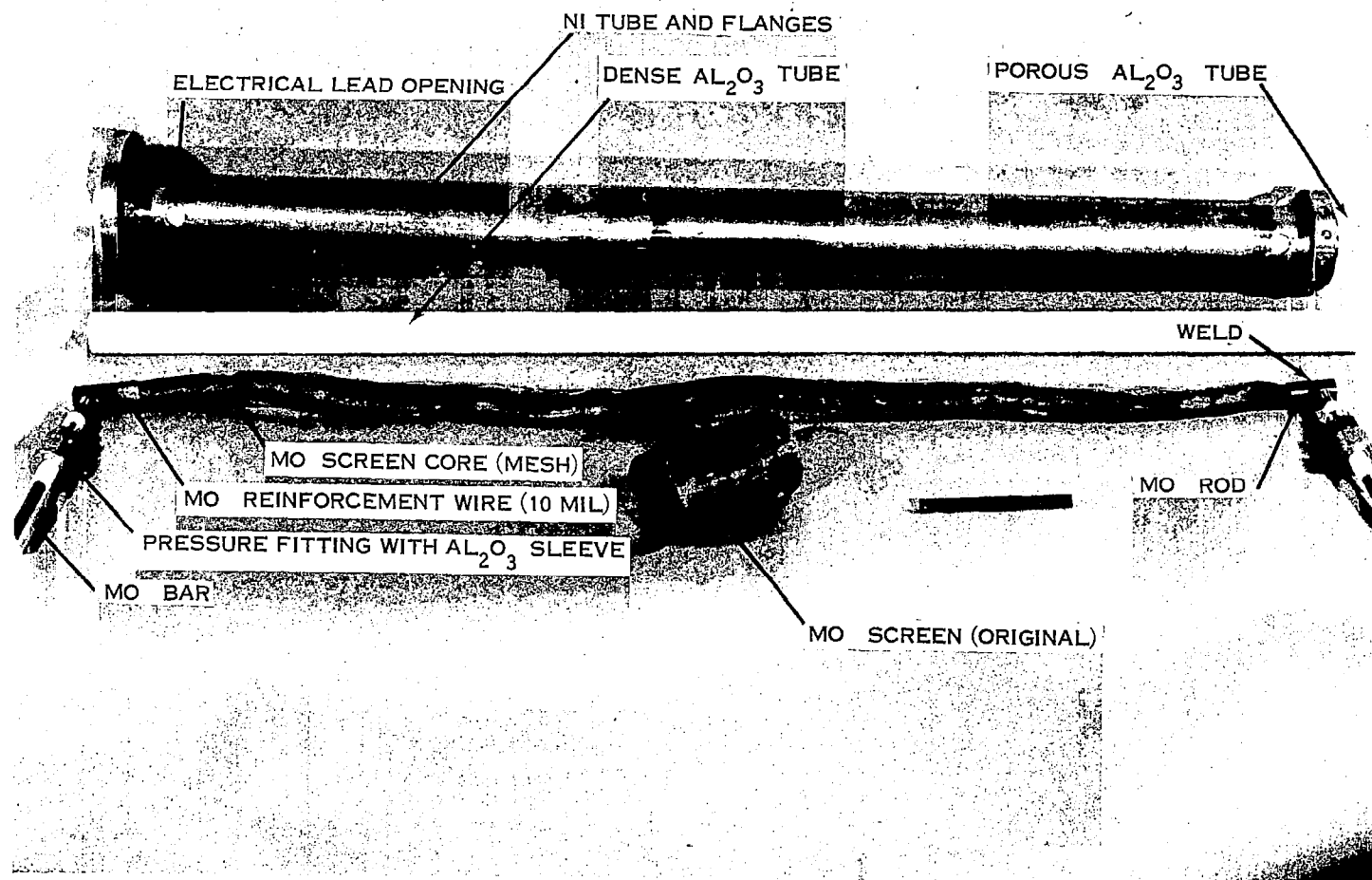


Figure 6. Heater Components

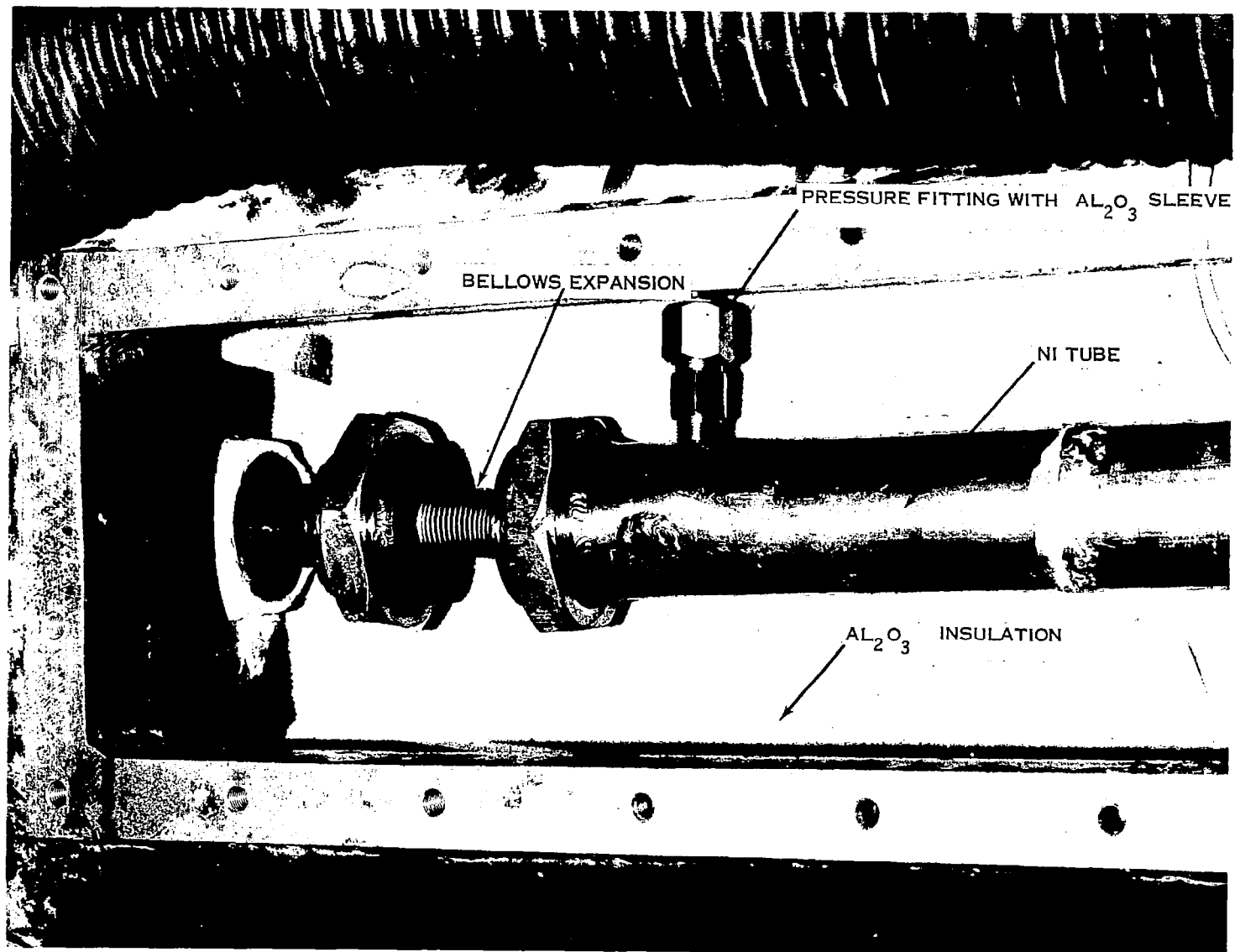


Figure 7. Assembled Heater

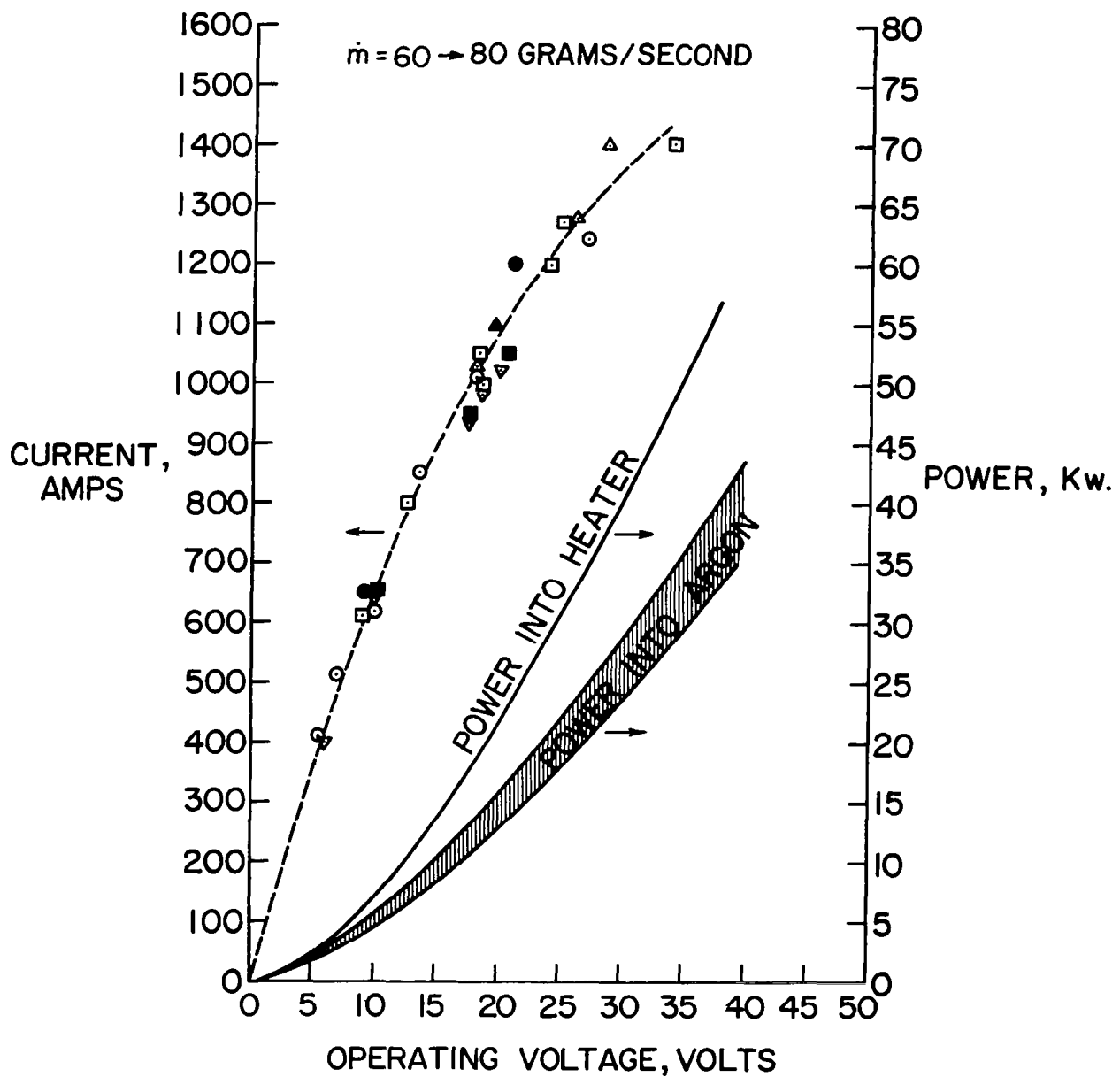


Figure 8. Operating Characteristics for Molybdenum Mesh Heater

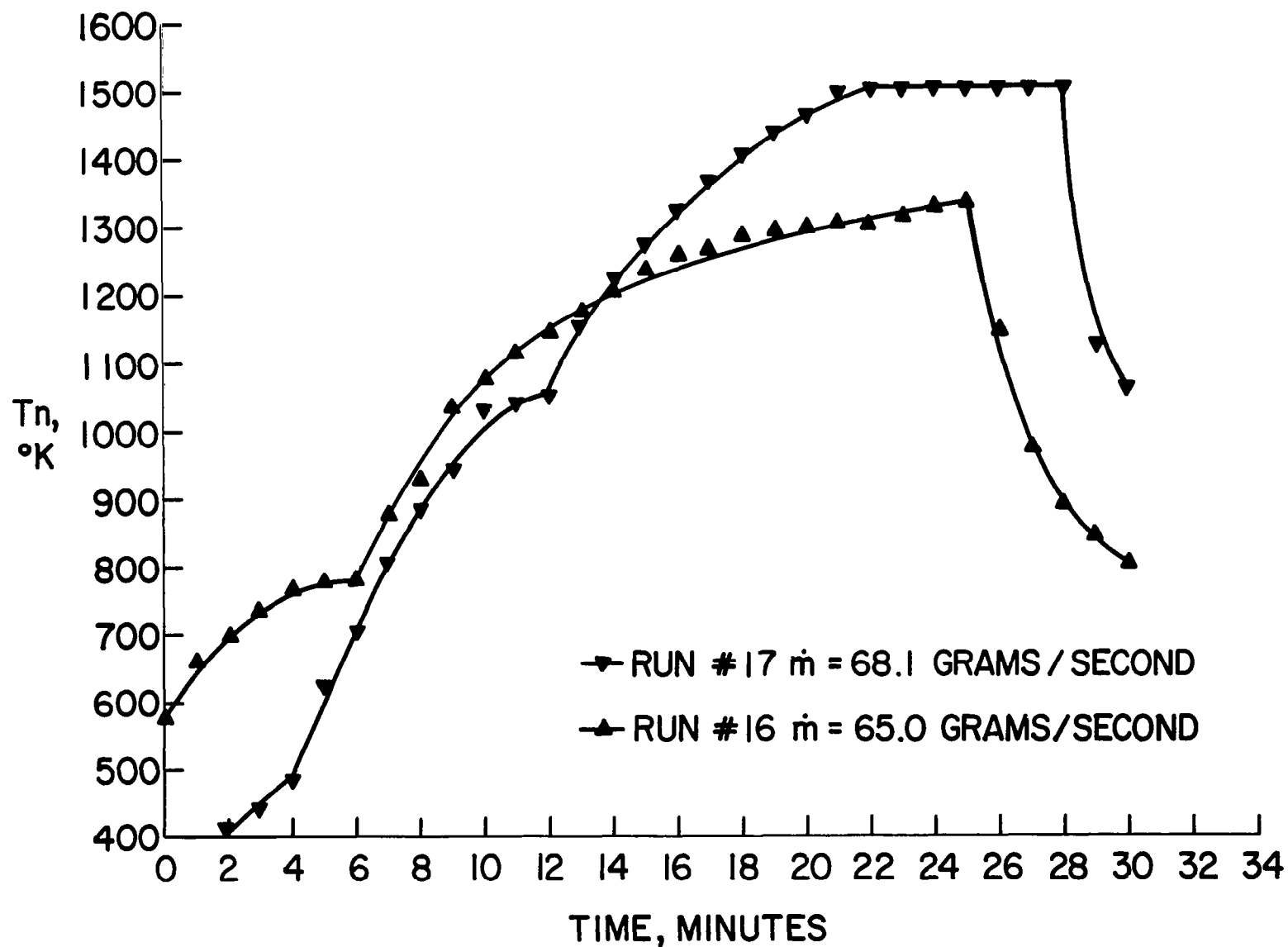


Figure 9. Temperature - Time Curves for Runs #16 and #17 (Typical)

4. Local "hot-spots" within the heater core are inherently reduced due to the strong temperature dependence of the electrical resistivity of the refractory metal.
5. A uniform temperature is produced within the gas.
6. Impurities imparted to the gas are kept to a minimum as opposed to an arc jet.

## C. COLD CATHODE ELECTRON BEAM

A cold cathode electron beam, developed by the GE Advanced Technology Laboratory (see Reference 3), was used to pre-ionize the seeded argon 22 cm. downstream of the nozzle throat. A 0.25 mil aluminum window, (used with special cooling techniques), proved to be the most attractive method for maintaining a low pressure in the cathode chamber. If a differential pumping system were used, pumping speeds  $\sim 600$  CFM and  $\sim 100$  CFM would be needed (see Appendix C). To reduce the energy losses of the electron beam as it passes through a foil, the foil had to be made very thin, and of metal with a very low atomic number.

The beam must have the right amount of energy to first penetrate the foil, and then to take part in ion-electron pair production within the flowing gas; the beam incident to the gas must have an average range of 1 cm (for the existing M-4 duct). If the range is much smaller than 1 cm, only the boundary layer will be ionized. If the range is much larger than 1 cm, utilization is not made of the fact that the cross-section for electron-ion pair production increases as the incident electrons near the end of their range. In addition to having the correct range (determined by the beam voltage), the beams must have enough ionizing electrons (the beam current) to produce a conductivity of at least 10 mhos/meter within the plasma.

### 1. General Discussion of Energy Loss Mechanisms

There are four major mechanisms by which the beam electrons will lose their kinetic energy (Reference 6):

1. Elastic collisions with atomic electrons
2. Elastic collisions with a nucleus
3. Inelastic collisions with a nucleus
4. Inelastic collisions with atomic electrons

Case 1. In this case, energy and momentum are conserved. The energy transfer is usually less than the lowest excitation potential of the atom. Since such collisions are only significant for incident electrons whose energy is  $< 100$  e.v., such collisions will be neglected.

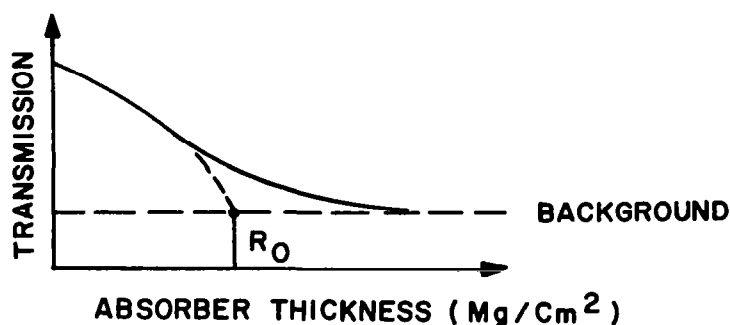
Case 2. The cross-section for nuclear scattering and the cross-section for electron scattering (Case 1) are of the order  $(e^2/m_0 v^2)^2$  for  $Z=1$ , where  $Z$  is the atomic number. However, the cross-section for nuclear scattering increases with  $Z^2$  whereas the cross-section for electronic scattering increases with  $Z$ . Consequently the cross-section for nuclear scattering is around  $Z$  times that for electronic scattering. Thus, the nuclear scattering cross-section of molybdenum for a 50 Kev

beam is around  $4 \times 10^{-21} \text{ cm}^2$ ; whereas the electronic scattering cross-section is approximately  $9 \times 10^{-23} \text{ cm}^2$ . However for beams with energies near 50 kev, this case can be neglected with respect to Case 4.

Case 3. In this case, the incident electron has a close, noncapture encounter with the nucleus. The probability of nuclear excitation is usually quite small and the energy transfer (resulting from deflections) usually appears as bremsstrahlung radiation. However, beam energies around 50 kev are too low for this case to be significant.

Case 4. During collisions of this case, one or more atomic electrons experience a transition to an excited or unbound state. This case is by far the most significant mechanism for energy transfer from electrons with energies around 50 kev. Consequently only inelastic collisions will be considered for the beam specification.

The "practical range,"  $R_0$ , of a monenergetic electron beam is obtained by the extrapolation of the transmission curve as shown below:



The background is primarily due to gamma rays and bremsstrahlung radiation from the absorber. The range-energy expression given by Katz and Penfold (see Reference 14) is shown in Figure 10. The required material properties necessary for the calculations are presented in Table 2. The results of the range calculations are presented in Figure 11.

Although beryllium has obvious advantages because of its low atomic weight and relatively high melting point, it was ruled out because of the ever present possibility that it might be vaporized and thus present a major danger to personnel. Instead, a 0.25 mil aluminum foil was used. A 1 x 30 mm slit (water cooled) was found to be adequate in cooling the 0.25 alumina foil from the heat generated due to a 55 Kev beam with a current  $\sim 60 \text{ m.a.}$  Two stainless steel tubes, slotted in such a manner as to buffer the aluminum foil with cool argon from the high temperature ( $1500^\circ\text{K}$ ) gas flow, have enabled successful operation of the electron beam in the MGD facility. Results are discussed later in the report. The amount of injection of cool argon amounted to less than 0.1% by weight of the total plasma flow.

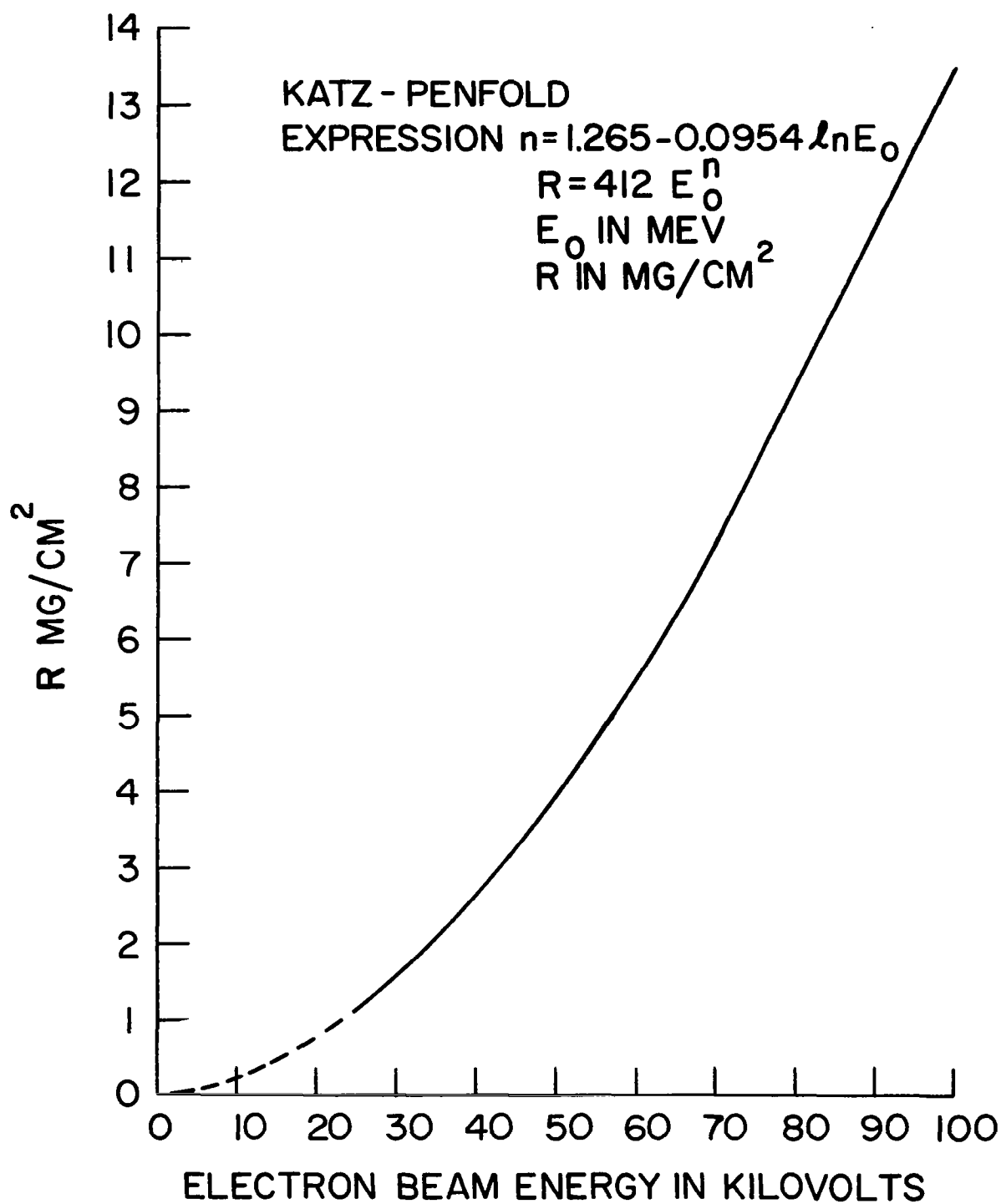


Figure 10. Beam Range vs. Beam Energy as Given by the Katz-Penfold Expression



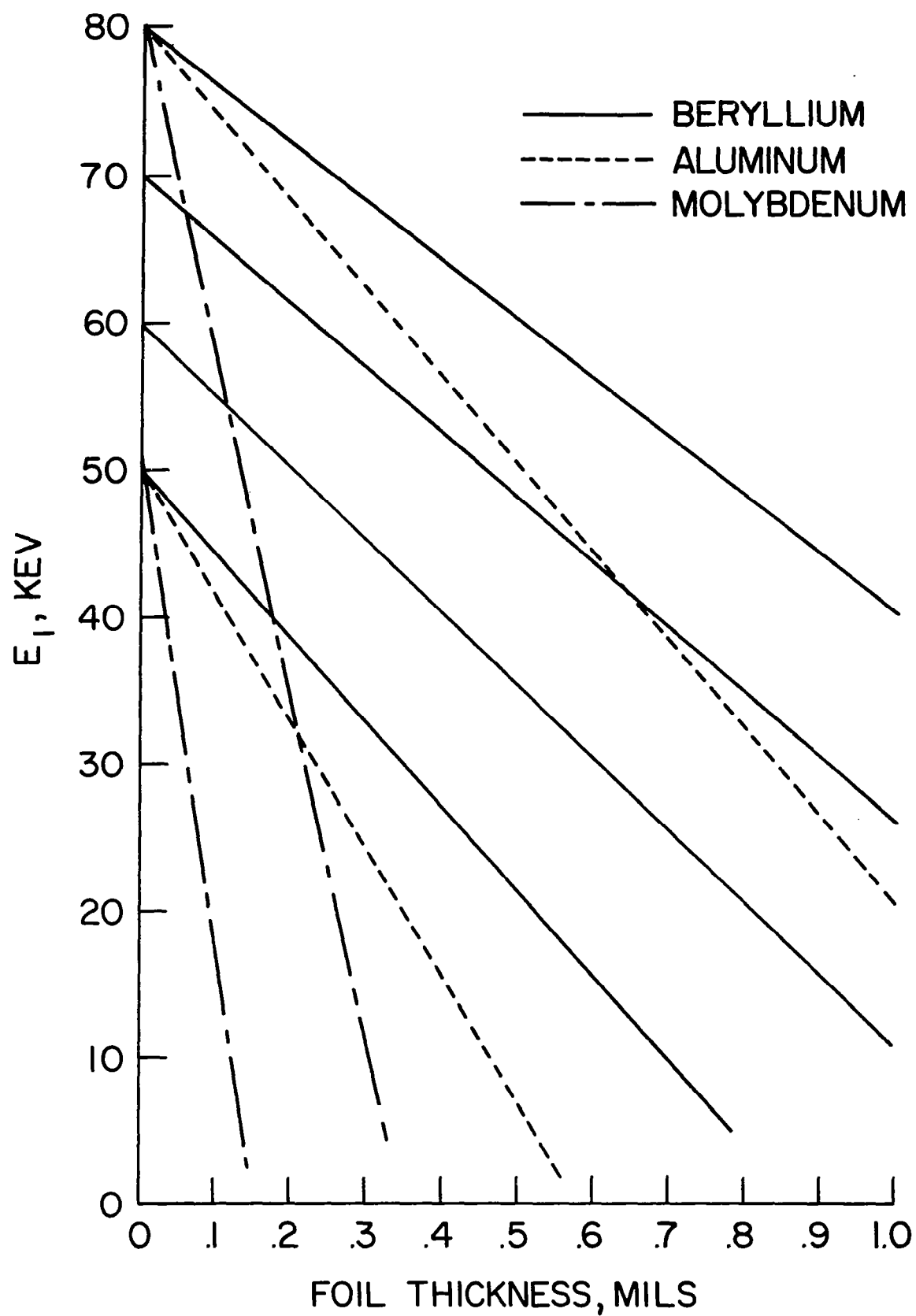


Figure 11. Most Probable Beam Energy Emerging from Foil vs. Foil Thickness (First Approximation)

TABLE 2. TABLE OF USEFUL PROPERTIES

<u>Metal</u>	<u>Density gr/cm<sup>3</sup></u>	<u>M. P. °K</u>	<u>Thermal Conductivity* at 300°C watts/cm<sup>2</sup> - °K/cm</u>
Be	1.8	1280	1.25
Al	2.7	660	2.26
Mo	10.2	2620	1.2 (approx.)
Ta	16.6	3000	0.4 (approx.)
W	19.3	3370	1.5

\*Data from American Institute of Physics Handbook, Second Edition, 1963

## 2. Description of Electron Beam System

The electron beam system attached to the M-4 duct is shown in Figure 12. Here the electron beam is created within a large Bell Jar and focused into a 3 cm. diameter beam at the aluminum window region. Part of the circular beam passed through the water-cooled aperture slit (see Figure 13) and then through the aluminum window which is held in place by the foil retainer shown in Figure 14. Holes have been drilled in the foil retainer to accept slotted tubes for argon cooling. The cover opening is much larger than the exit aperture so as not to intercept any of the electron beam which is scattered by the foil. The cathode chamber in actual operation is shown in Figure 15. Figure 16 is a drawing of the "Tee Assembly" which is the adapter section necessary to modify the original MGD duct for the introduction of the electron beam. The material (nickel) was chosen so as to keep non-magnetic materials along the beam path. The two threaded holes at the junction of the tee are necessary for the introduction of the tubing through which cool argon is introduced to form a thermal insulator between the aluminum window and the hot argon stream.

The "Water-Cooled Aperture Slit" (See Figure 13) shows the pieces from which the exit apperture was constructed. The circular groove in the piece mates with the circular ridge in the foil retainer cap so as to give a vacuum seal with the foil in place. The two piece construction was needed to give the proper water flow channel to insure proper cooling.

Figure 17 "Tube Details." Here are given the details of the path of water flow from the "Water Passage Flange" (Figure 18) to the apperture cooling and back as well as the separators needed to separate the inlet from the exit passage. The water passages are designed such that the total cross sectional area presented by the five of them, for each flow direction, equals the cross sectional area of the inlet.

Figure 18 "Water Passage Flange." The water inlet and exit ports are given as well as the o-ring grooves and bolt holes needed for mounting the total assembly.

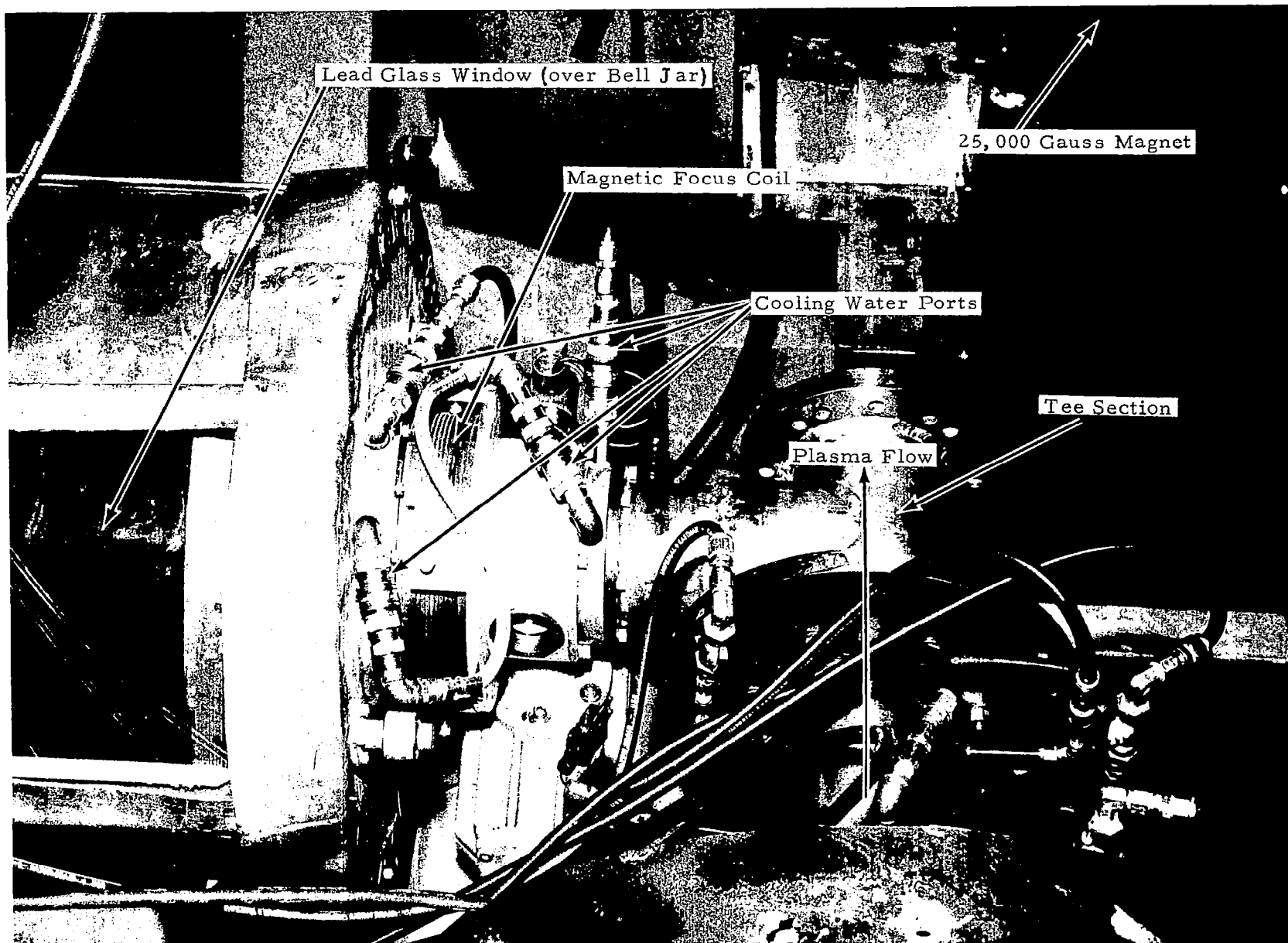


Figure 12. Electron Beam System Attached to M-4

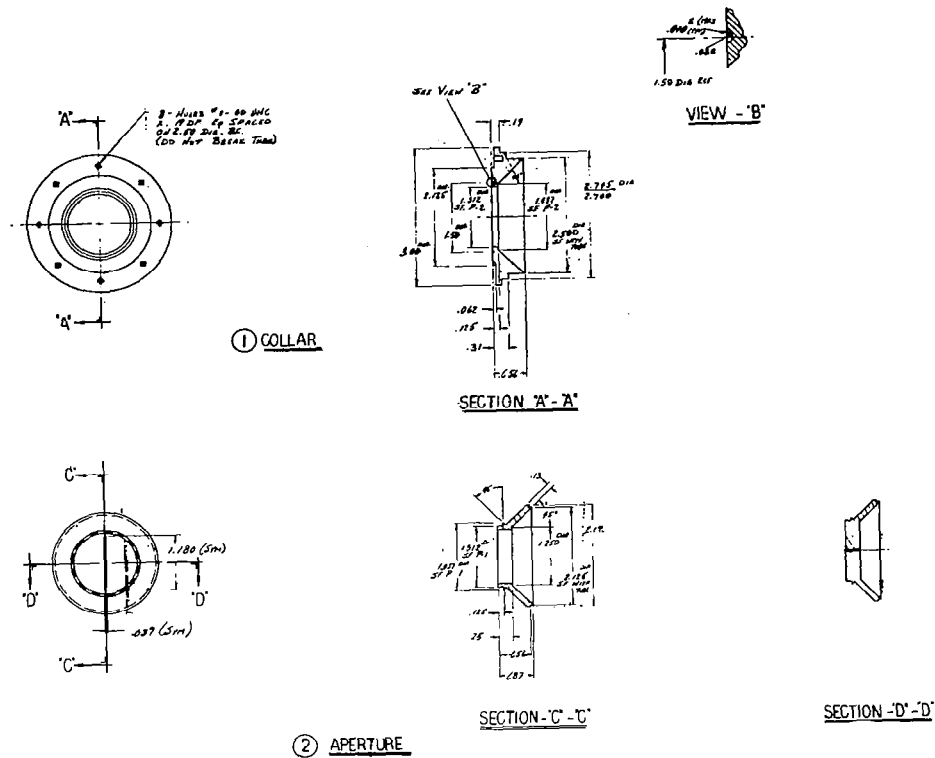


Figure 13. Water Cooled Aperture Slit

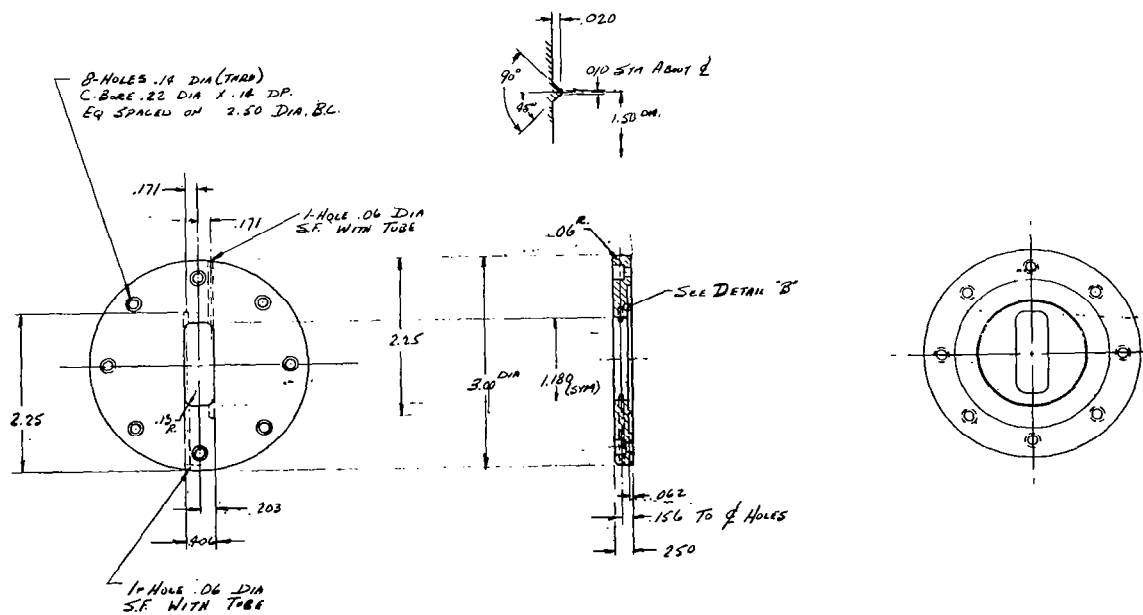


Figure 14. Foil Retainer

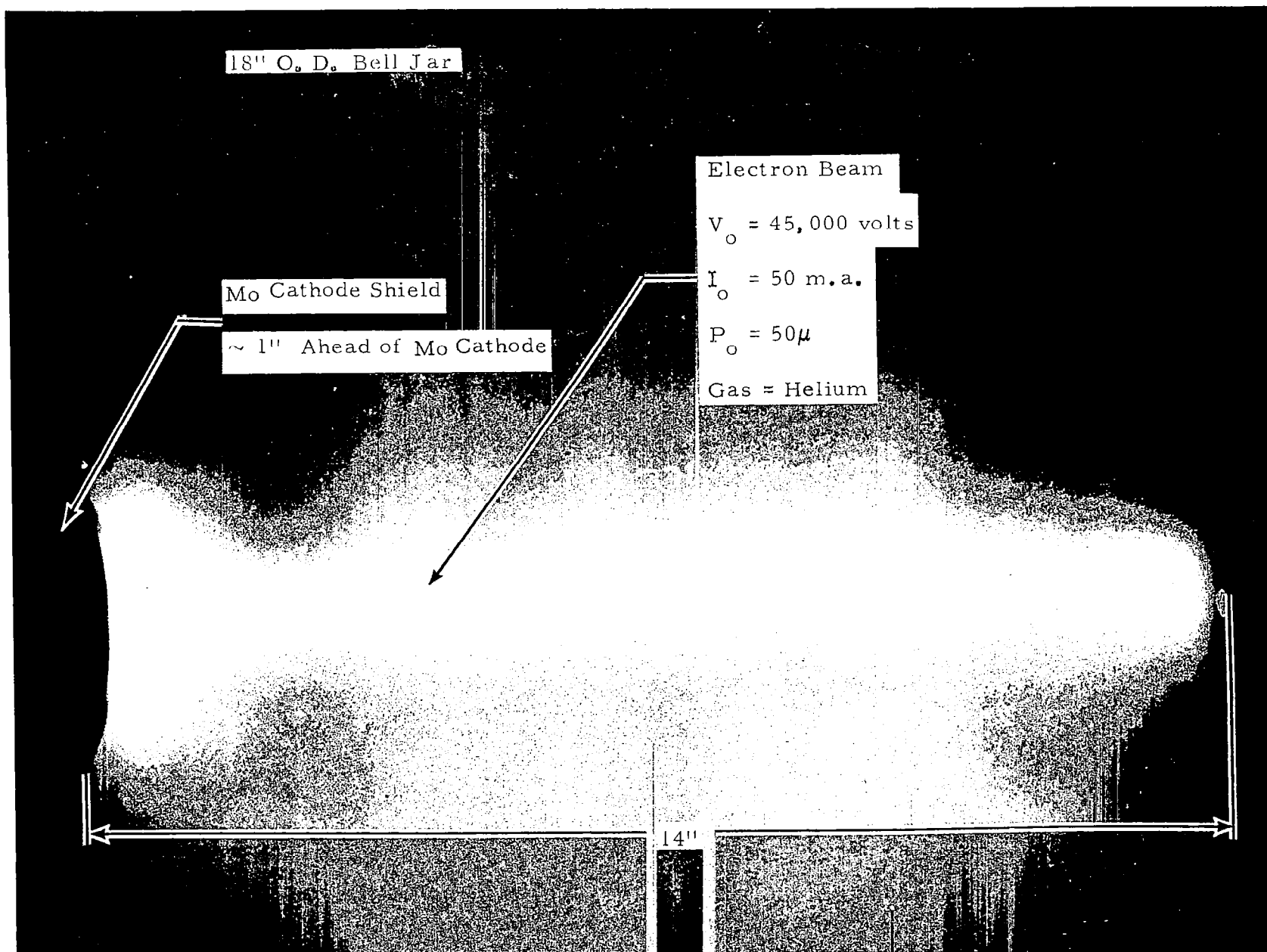


Figure 15. Electron Beam in Cathode Chamber

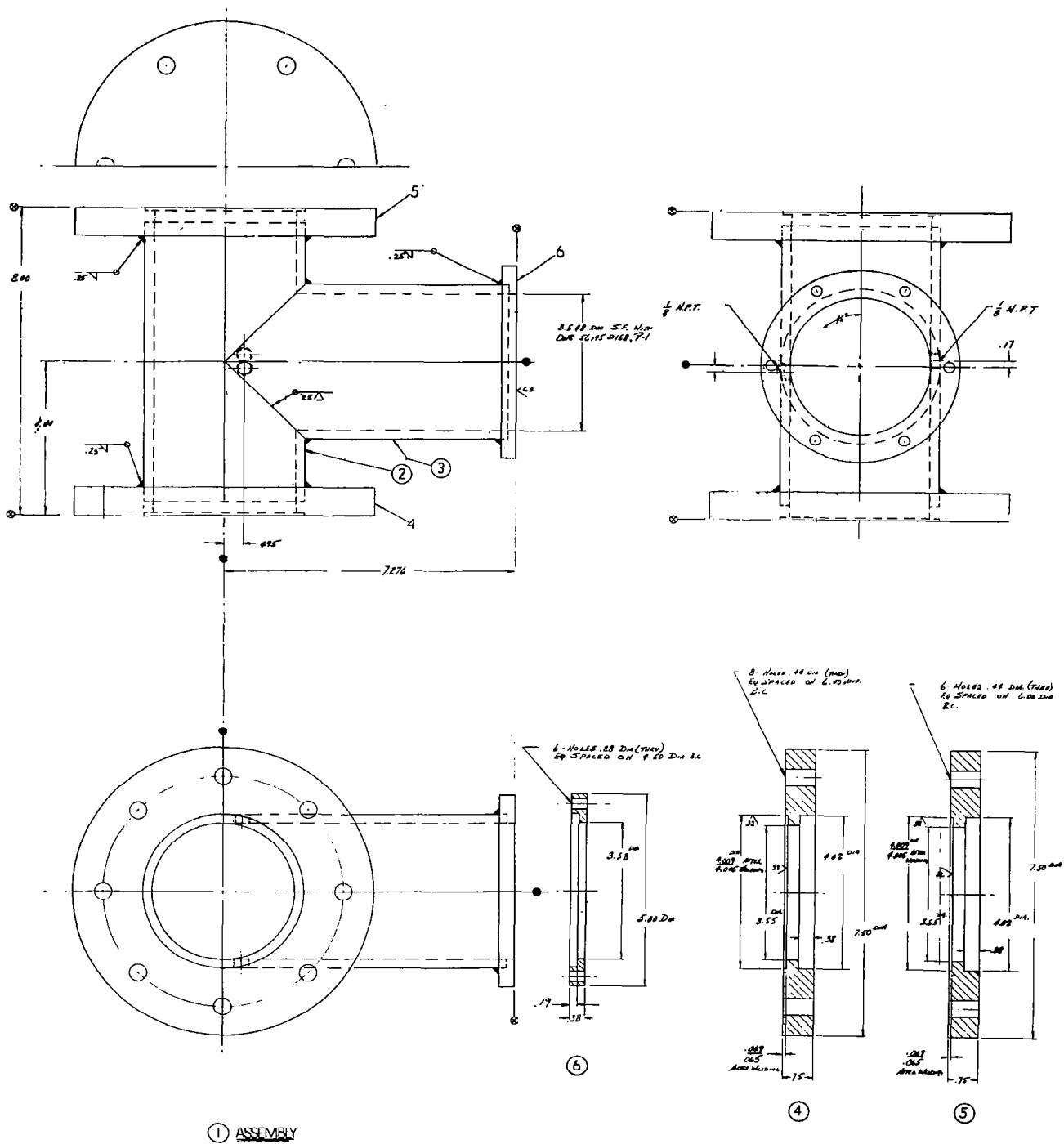


Figure 16. Tee Assembly

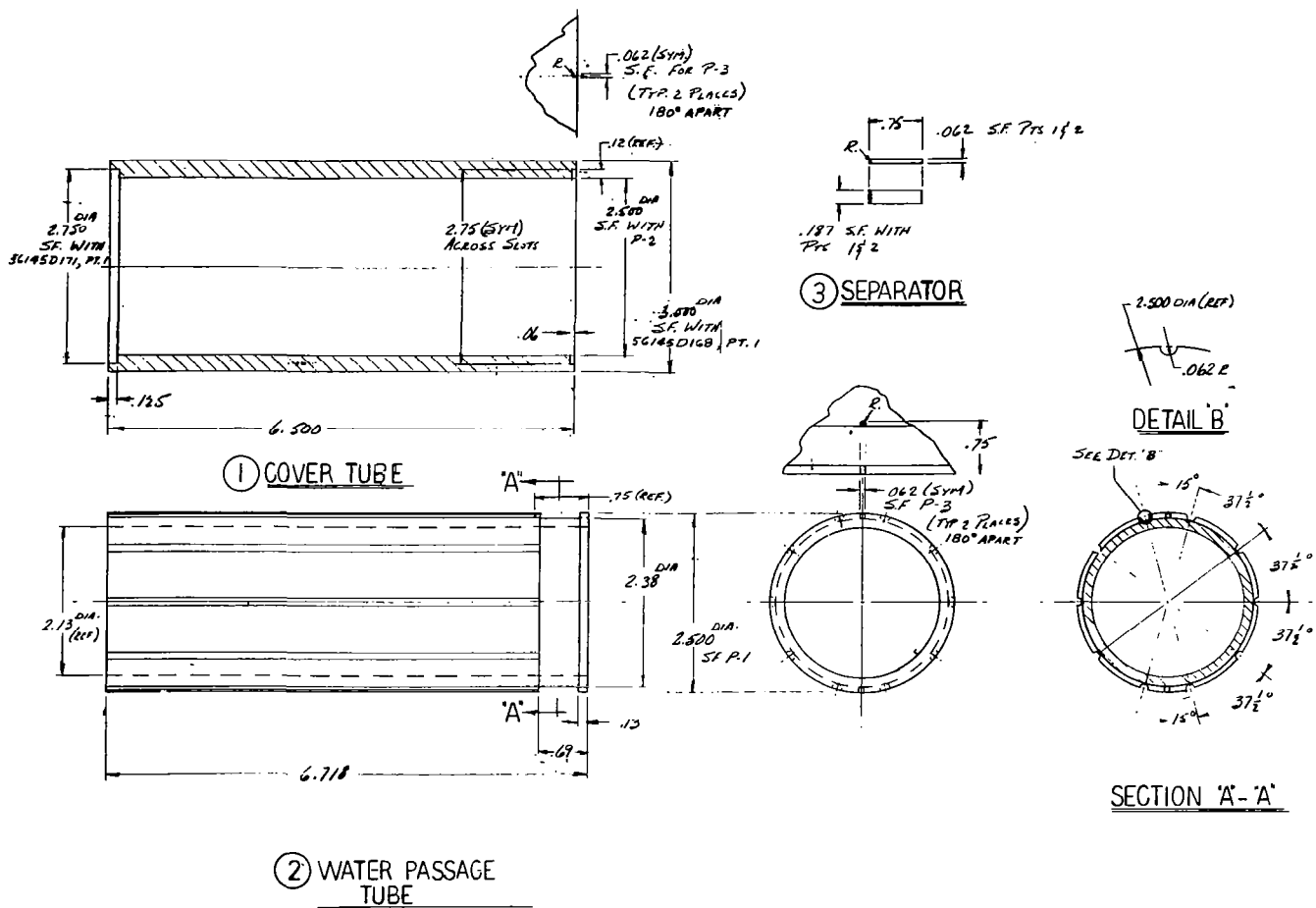


Figure 17. Tube Details

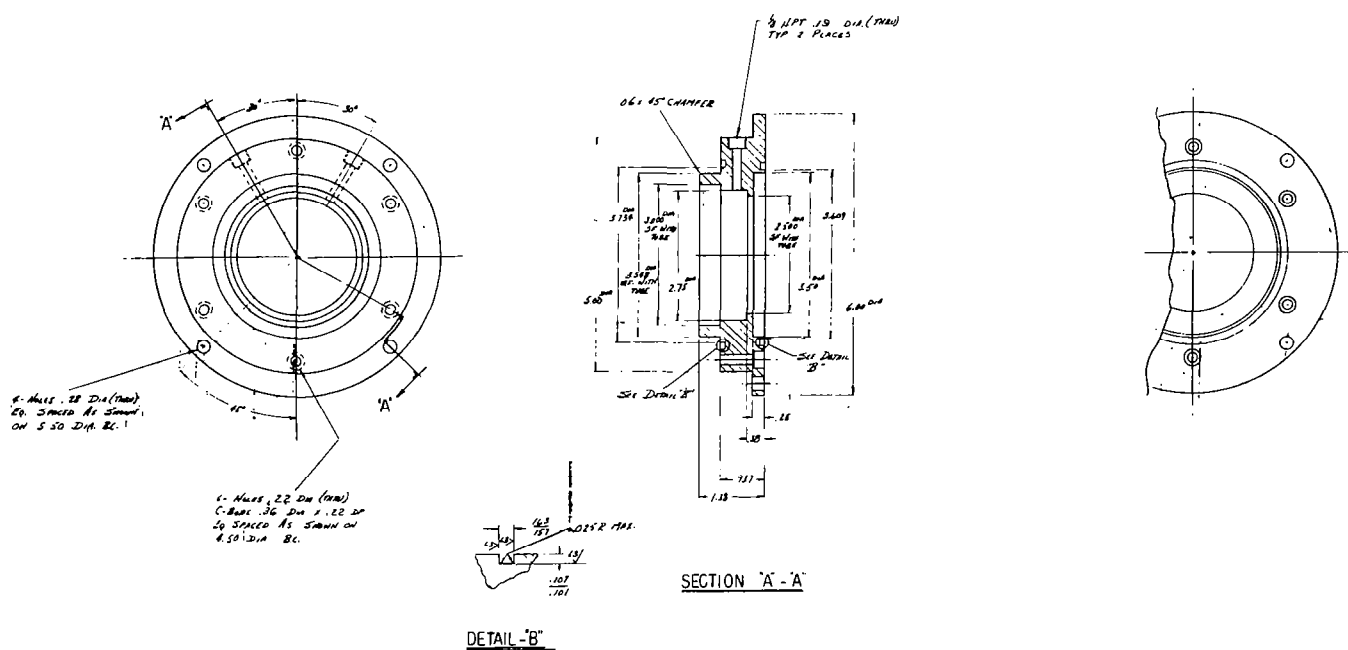


Figure 18. Water Passage Flange

Figure 19 and 20 are detailed drawings of the pumping station.

Figure 19 "Flange Assembly." This is designed to mate with a 2" gate valve.

Figure 20 "Electron Beam Details." In this block is a view port which allows one to see the beam cross over point which is visible due to the presence of the working gas pressure. The two other side ports lead to the gate valve flange and the vacuum gauge holder.

Figures 21, 22, 23, 24 are the drawings of the magnetic section, including 21 "Adapter," 22 "Adapter Assembly," 23 "Flange Detail" and 24 "Adjusting Block." The design is such as to allow the magnetic coil (Figure 25) to be outside of the evacuated region, thereby easing cooling requirements. The "Adjusting Blocks" (Figure 24) are needed to allow fine adjustment of the focusing coil position relative to the central ray of the beam.

Figures 25 and 26 "Magnet" and "Magnet Housing," respectively, give the specifications for the focusing coil and its shroud. Also noted on Figure 26 are the heat treating requirements for the Armco iron used in the shroud. The "Water Cooled Aperture Assembly" is used as the image for the electron optics which follow. It is water cooled since it will intercept a portion of the beam exiting through it from the cathode housing.

### 3. Expected Performance of Electron Beam

#### a. MGD Channel Electron Density

It is desired to calculate the electron beam and power supply characteristics needed to produce a 10 mho/meter conductivity in the flowing MGD channel gas. The first step is to calculate the electron density needed to yield a plasma with 10 mho/meter conductivity:

#### (1) General Method

Since ions carry a negligible plasma current compared to electrons, the total conductivity,  $\sigma$ , is (References 7, 8)

$$\sigma = \left[ \sigma_i^{-1} + \sigma_n^{-1} \right]^{-1} \quad (1)$$

where  $\sigma_i$  is the electron-charged particle collision-limited conductivity.

Now, (References 7, 9)





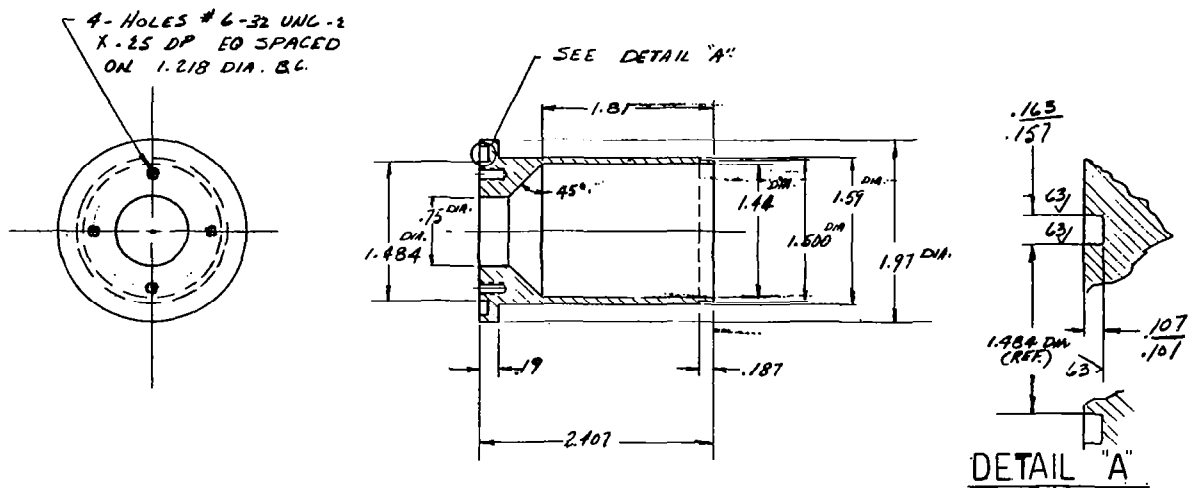


Figure 21. Adapter

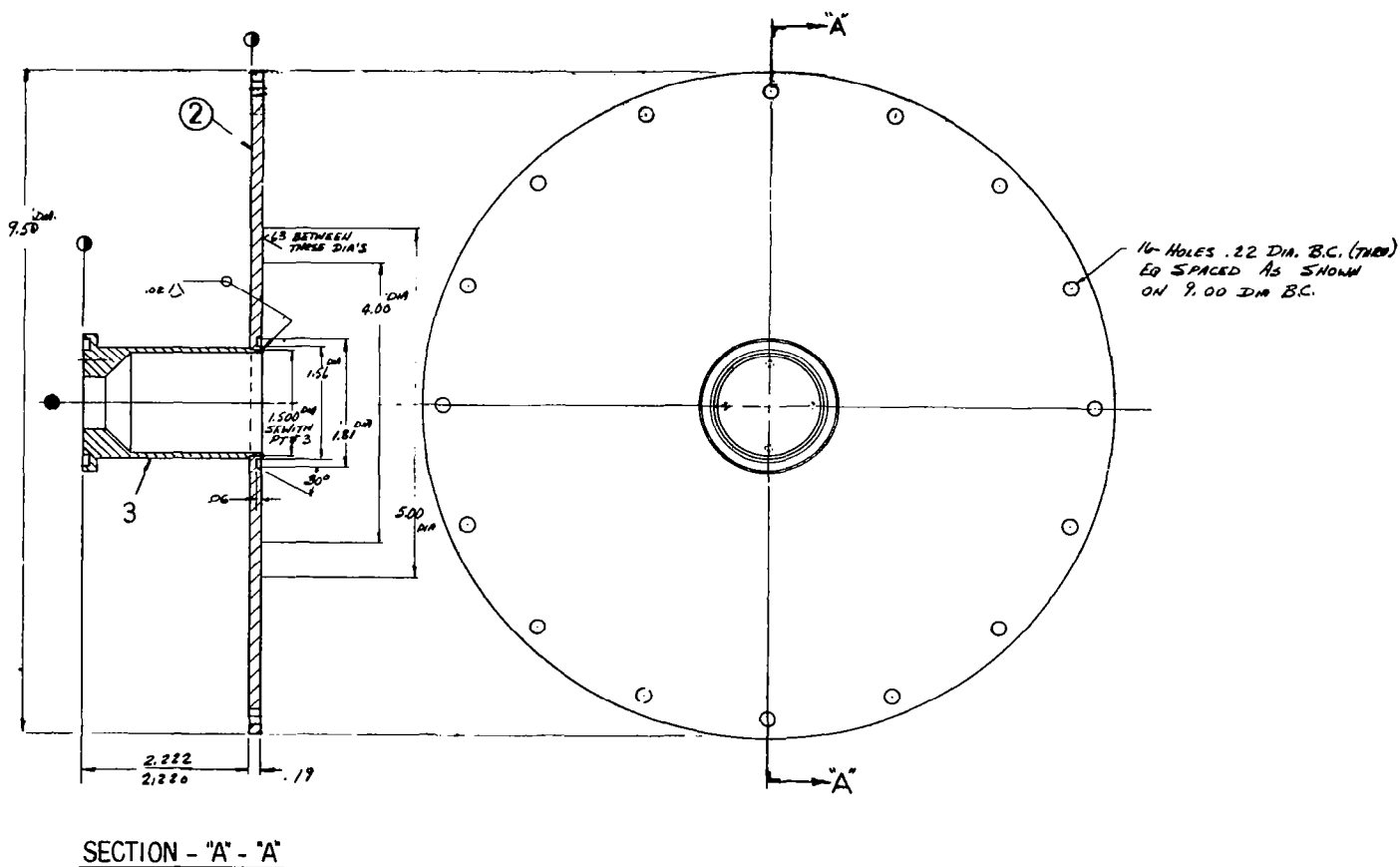


Figure 22. Adapter Assembly

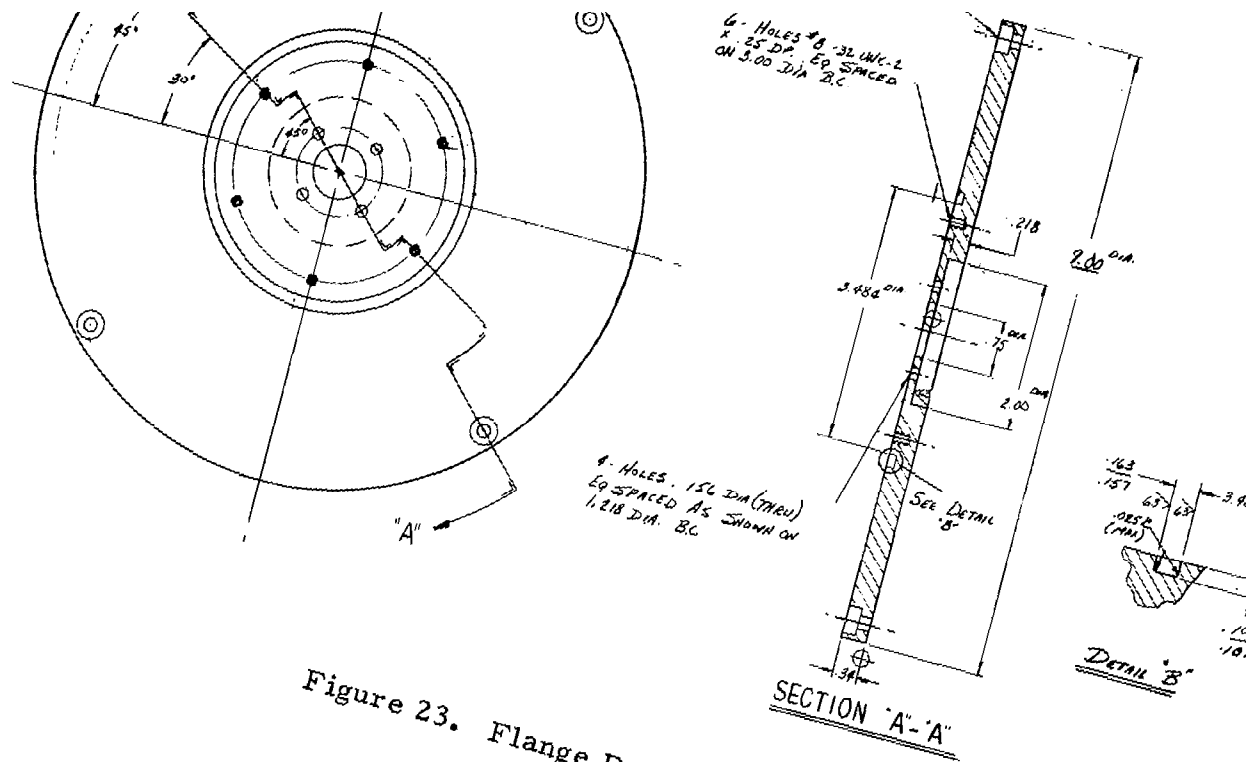


Figure 23. Flange Detail

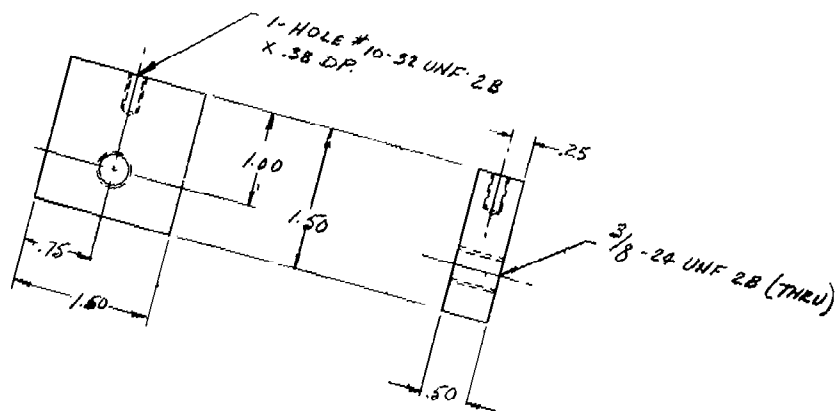


Figure 24. Adjusting Block



$$\sigma_i = 0.591 (kT_e)^{3/2} (m^{1/2}/e^2 \ln \Lambda) \quad (2)$$

$$\sigma_i = 1.53 T_e^{3/2} / (\ln \Lambda) \text{ mho/cm} \quad (3)$$

where (References 7, 10)

$$\Lambda = \frac{3}{e^3} \left( \frac{k^3 T_e^3}{8\pi n_e} \right)^{1/2} \quad (4)$$

$$\Lambda = 1.24 \times 10^4 T_e^{3/2} / n_e^{1/2} \quad (5)$$

In equations 2-5,  $k$  is the Boltzmann constant,  $T_e$  is electron temperature ( $^{\circ}\text{K}$ ),  $m$  is electron mass,  $e$  is the electronic charge, and  $n_e$  is the electron density (electrons/cc).

For electron-atom conductivity, Chapman and Cowling give (References 7, 8, 11)

$$\sigma_n = 0.532 \alpha e^2 / [(mkT_e)^{1/2} Q] \quad (6)$$

$$= 3.85 \times 10^{-6} \alpha / (T_e^{1/2} Q) \text{ mho/cm} \quad (7)$$

where

$$\alpha = n_e / N \quad (8)$$

Here,  $\alpha$  is the degree of ionization,  $N$  is the preionization particle density, and  $Q$  is the electron-atom collision cross section ( $\text{cm}^2$ ). Chapman and Cowling's equation (equation 6 above) assumes a  $Q$  which is constant with electron velocity while most real gases have  $Q$  varying considerably with electron velocity. However, for each temperature, a Maxwell-averaged  $Q$ ,  $Q_T$  may be used in equation 6, where (References 7, 8)

$$Q_T = \frac{kT/m_e}{\int_0^{\infty} \frac{c}{Q(c)} e^{-m_e c^2/2kT} dc} \quad (9)$$

Here,  $c$  is the electron velocity and  $Q(c)$  in the un-averaged  $Q$  which is a function of  $c$ .

Although equations 1-9 may be solved for  $n_e$ , the solution is a function of both  $\sigma$  and  $T_e$ , of which only  $\sigma$  is predetermined (at 10 mhos/m).

However, this choice can be resolved, since  $T_e$  and  $n_e$  must satisfy not only  $\sigma$ , but can also be made to satisfy the Saha (equilibrium) ionization equation: Although this "enhanced" plasma is not at complete thermal equilibrium, the  $T_e$  (and  $n_e$ ) should be in a quasi-equilibrium with the atoms and ions if  $T_e$  and  $n_e$  are to avoid further change through direct recombination or secondary ionization. Of course,  $T_e$  and  $n_e$  will start decrease due to other energy and electron losses since the system is far from true equilibrium.

For neutral atoms, singly charged ions, and electrons in true equilibrium at temperature  $T$ , the Saha equation gives (Reference 12)

$$\frac{n_e \cdot n_i}{n_o} = \frac{U_i}{U_o} \frac{2 (2\pi mkT)^{3/2}}{h^3} \exp -E_o/kT \quad (10)$$

Here,  $n_i$  is ion density,  $n_o$  is neutral particle density,  $U_i$  and  $U_o$  are the partition functions of the ions and the neutral particles respectively,  $h$  is the Planck constant, and  $E_o$  is the energy required to ionize the neutral atom to the single charged ion. If we now assume that  $n_e = n_i$ , use  $T_e$  in place of  $T$ , and express the number densities in particles/cc,  $E_o$  in electron volts, and  $T$  in  $^{\circ}K$ , we can then re-write the Saha equation as

$$\frac{n_e^2}{n_o} = 4.83 \times 10^{15} \frac{U_i}{U_o} T_e^{3/2} \exp - \frac{11605 E_o}{T_e}, \text{ cm}^{-3} \quad (11)$$

We now see that given the MGD channel gas, gas density, conductivity desired ( $\sigma = 10 \text{ mho/m}$ ), and  $Q$  or  $Q_T$ , the simultaneous solution of equations 1, 3, 5, 7, 8, and 11 will give us both  $n_e$  and  $T_e$  in the channel. However, this calculation can be simplified if  $\sigma_i \gg \sigma_n$  because then we can say  $\sigma = \sigma_n$ . This assumption was made for the actual calculations, and, using the final results, was justified for all cases treated. Now using equations 7 (re-arranged) and 8, letting  $\sigma_n = \sigma$ , and assuming  $N = n_o$  (correct if  $\alpha \ll 1$  as if the case), we have

$$\frac{n_e^2}{n_o} = n_o \alpha^2 = n_o T_e (\sigma \cdot Q)^2 / (3.85 \times 10^{-6})^2, \text{ cm}^{-3} \quad (12)$$

We now have only two equations (11 and 12) which can be solved simultaneously for  $n_e$  and  $T_e$ , but the form of these equations makes this difficult.

The actual calculations for helium and argon were made as follows: Equation 11 was plotted as  $n_e^2/n$  vs.  $T_e$  for both helium and argon, this first being done crudely for  $T_e \cong 5000^\circ - 10,000^\circ\text{K}$ , and then carefully in the subsequently determined exact  $T_e$  region of interest. The  $T_e$  was then assumed to be  $10,000^\circ\text{K}$  and equation 12 solved for  $n_e^2/n_0$ , this  $n_e^2/n_0$  giving a new  $T_e$  value from the equation 11 graph. This new  $T_e$ , plus (if equation 12 and the result compared with the graph. This process was repeated until  $T_e$  repeated to within  $3^\circ\text{K}$  or less, these iterations converging very quickly. Finally,  $n_e$  was determined from equations 7 and 8 using the last value of  $T_e$  and its  $Q_T (=Q)$ .

## (2) The Calculations

Specifically, we wish to calculate the  $n_e$  and  $T_e$  needed to give both helium and argon conductivities of 10 mho/meter at plasma atom temperature ( $T_a$ ) of  $1000^\circ\text{C}$  ( $1273^\circ\text{K}$ ) and  $1500^\circ\text{C}$  ( $1773^\circ\text{K}$ ), and at pressures of 1 and 2 atmospheres.

### a. Helium Input and Results

For the calculation and graphing of  $n_e^2/n_0$  by equation 11,  $E_0 = 24.58$  ev,  $U_i = 2$ , and  $U_0 = 1$  ( $U$  values are from Reference 6). Helium has been found to have a relatively constant electron collision cross section at low electron energies, Phelps, Pack, and Frost<sup>13</sup> finding a constant  $Q = 6.2 \times 10^{-16} \text{ cm}^2$  for average electron energies from about 0.1 ev to 2 ev = ( $T_e = 775^\circ$  to  $15,500^\circ\text{K}$ ). The calculated results of  $N (\cong n_0)$ ,  $T_e$ ,  $\alpha$ , and  $n_e$  are shown in Table 3.

### b. Argon Input and Results

For the calculation and graphing of  $n_e^2/n_0$  by equation 11,  $E_0 = 15.755$  ev,  $U_i = 6$ , and  $U_0 = 1$  ( $U$  values are from Reference 13). Since the Ramsauer effect is very pronounced in argon, its electron-collision cross section varies strongly with (low) electron temperatures. Consequently  $Q_T$  for argon (Reference 8) varies from a minimum of about  $2 \times 10^{-17} \text{ cm}^2$  at  $T_e = 3000^\circ\text{K}$ , to very much larger values at higher temperatures. At  $T_e$  about  $5000^\circ\text{K}$ ,  $Q_T$  was taken (Reference 8) to be  $2.5 \times 10^{-17} \text{ cm}^2$ . The calculated results for argon are also in Table 3.

TABLE 3

Plasma Conditions for Conductivity = 10 mho/meter.  
A number in parentheses means "times" that power of ten.

Gas Pressure		1 atm.		2 atm.	
Gas Temperature ( $T_a$ )		1273°K	1773°K	1273°K	1773°K
$N \cong n_o$ (atoms $\text{cm}^{-3}$ )		5.75 (18)	4.14 (18)	1.150 (19)	8.27 (18)
He	$T_e$ (°K)	9675	9573	9904	9797
	$\alpha$	1.58 (-5)	1.58 (-5)	1.60 (-5)	1.59 (-5)
	$n_e$ ( $\text{cm}^{-3}$ )	9.11 (13)	6.52 (13)	1.84 (14)	1.32 (14)
Ar	$T_e$ (°K)	4986	4942	5081	5037
	$\alpha$	4.59 (-7)	4.57 (-7)	4.63 (-7)	4.61 (-7)
	$n_e$ ( $\text{cm}^{-3}$ )	2.64 (12)	1.89 (12)	5.33 (12)	3.81 (12)

### (c) Electron Beam Current and Energy

From the required conductivity (10 mho/m), given the gas, its temperature and pressure, one may calculate the needed number density of electron-ion pairs/cc.  $N_e$ : The gas volume swept out in the channel per second (V) is equal to the gas velocity (w) times the cross sectional area of the duct A. Making use of the average energy of creation per electron-ion pair ( $I_o = 31$  ev/ion pr for Helium and 25 ev per ion pr for Argon) and the energy of the primary electron (E), one obtains the number of electron-ion pairs per primary electron ( $\beta = E/I_o$ ). The number of primary electrons necessary per second is given by the number of electron-ion pairs per second divided by the number of electron-ion pairs created per primary electron ( $N_e V/\beta$ ). The required electron beam current in amperes (I) is just this number times the number of coulombs/electron ( $I = N_e V/\beta$ )  $1.6 \times 10^{-19}$  amperes), which, making the appropriate substitution for w, and a duct cross section of  $3 \text{ cm}^2$ , yields:

$$I = \frac{I_o N_e V \cdot 4.8 \times 10^{-19}}{E} \quad \text{amperes}$$

Thus given  $N_e$  and working fluid (hence I and the sonic velocity w are determined) one need only place a requirement on the initial energy of the electrons (E) and the required beam current is entirely determined.

In order to make optimum use of the energy of the primary electrons, let it be required that the range of the electron shall be equal to the dimension of the duct across which the beam is being fired plus 1 cm to allow for the beam to spread before entering the channel. Using this criterion one may calculate the initial beam energy from the Katz and Penfold (Reference 14) relation



$$R_o \text{ (mg/cm}^2\text{)} = 412 E^N$$

$$\text{where } N = 1.265 - 0.0954 \ln E$$

$$0.01 \text{ Mev} \leq E \leq \sim 3. \text{ Mev}$$

for all conditions which give an initial energy within the region of validity for this equation. Below 0.01 Mev one may use the so-called Thomson-Whiddington law (Reference 6)  $\bar{S} \approx \text{const} (E^2/NZ)$  which when normalized to the above relation at 10 kev yields:  $E = \sqrt{R \times 10^{-3}/1.66} \text{ mev}$  where R is the range in  $\text{mg/cm}^2$ .

Making use of this, plus the number density  $N_e$  for electron ion pairs calculated above, one obtains the values for electron energy and beam current given in Table 4.

TABLE 4

		<u>Helium</u> I = 31 ev		<u>Argon</u> = 25 ev	
<u>pressure</u>	<u>distance</u>	<u>E (kev)</u>	<u>I (in ma)</u>	<u>E (kev)</u>	<u>I (in ma)</u>
<u>at 1273°K</u>					
1 atm.	{ 2 cm	6.78	42.0	21	0.101
	{ 4 cm	9.59	29.7	31	0.0682
2 atm.	{ 2 cm	9.6	60.0	30	0.142
	{ 4 cm	13.6	42.4	44	0.0967
<u>at 1773°K</u>					
1 atm.	{ 2 cm	5.74	42.0	18	0.0988
	{ 4 cm	8.12	29.7	25	0.0711
2 atm.	{ 2 cm	8.13	60.0	25	0.143
	{ 4 cm	11.5	42.4	36	0.0996

#### 4. Calibration of Electron Beam

A typical calibration curve for relatively high pressure helium is presented in Figure 27. A water cooled Faraday cup, (consisting of an electrically isolated aluminum tube  $\sim 7''$  long with an I.D. =  $2\text{-}3/8''$  and in which the bottom was slanted  $44^\circ$  from the side), was used to calibrate the electron beam. The cup chamber was pumped down below 0.1 microns to eliminate errors due to secondary electron formation. A typical calibration curve of the exit beam leaving the aluminum window is shown in Figure 28. An ammeter, placed between the cup and ground, was used to measure the current. The average energy of the emergent beam was calculated from the rise in temperature of the cooling water, once the current was known. A typical temperature rise vs current curve is shown in Figure 29. Values of the average energy of the emergent beam agreed within 5% of the value obtained from Figure 11 (calculated from the Katz-Penfold relation). A solenoid magnetic focus, between the cathode chamber and the injection port, was used to vary the diameter of the electron beam. The influence of the magnetic focus is shown in Figure 30. The actual power into the plasma is around 5 watts since only a 1 mm x 3 cm section of the circular beam passes into the channel. The actual beam power into the plasma can be greatly increased by the use of a quadrupole focus which can create a sheet beam to pass through the aperture slit.

#### 5. Modulation of Electron Beam

Modulation of the electron beam can be achieved by using the modulating circuit (shown in Figure 31) to modulate the magnetic focus. Typical oscillogram wave forms delivered to the focus coil are shown in Figure 32. By using the modulating circuit, the electron beam current collected by the Faraday cup was found to be properly modulated. This will enable the beam to be used for A-C studies to be conducted in future tests.

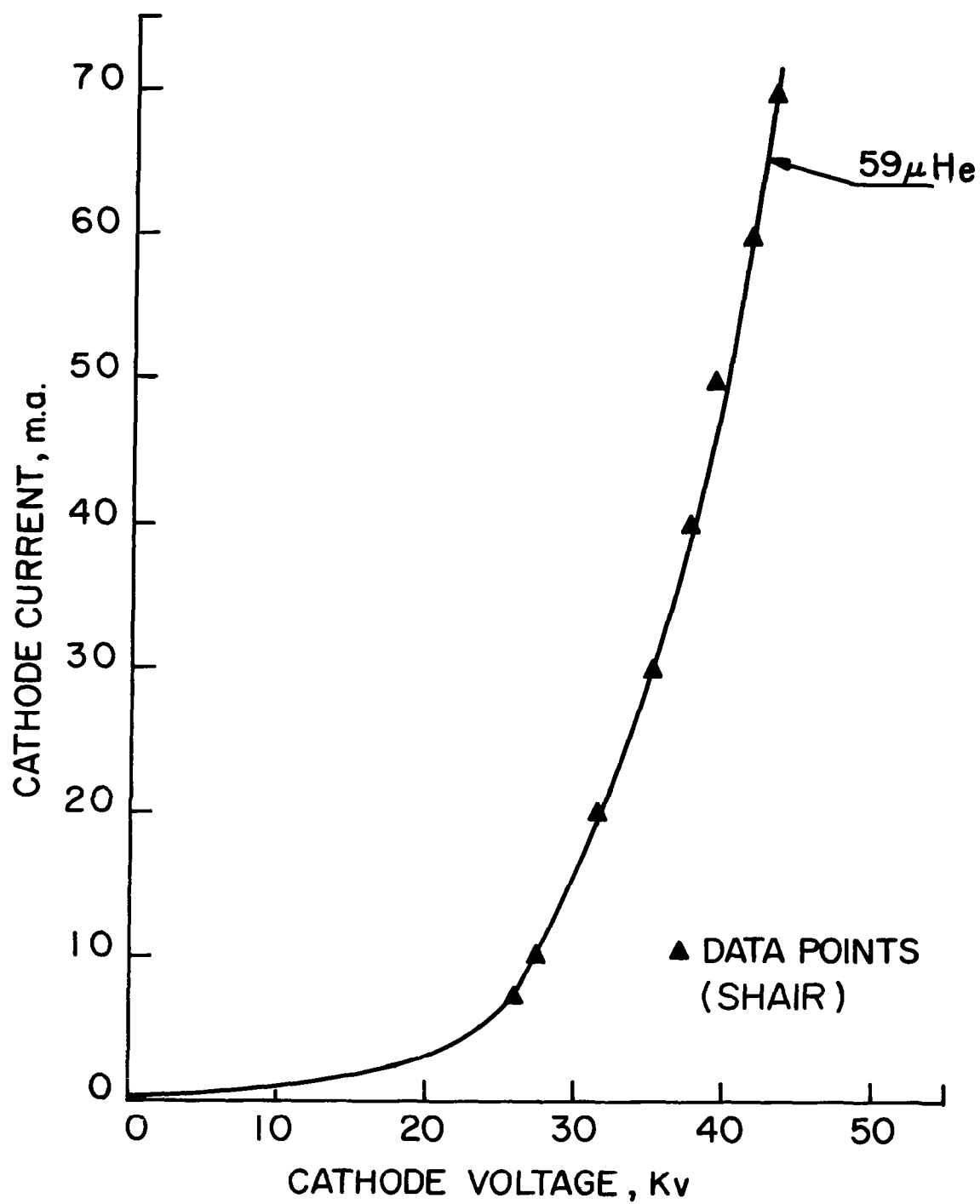


Figure 27. Electron Beam Calibration Curve for Helium (High Pressure)

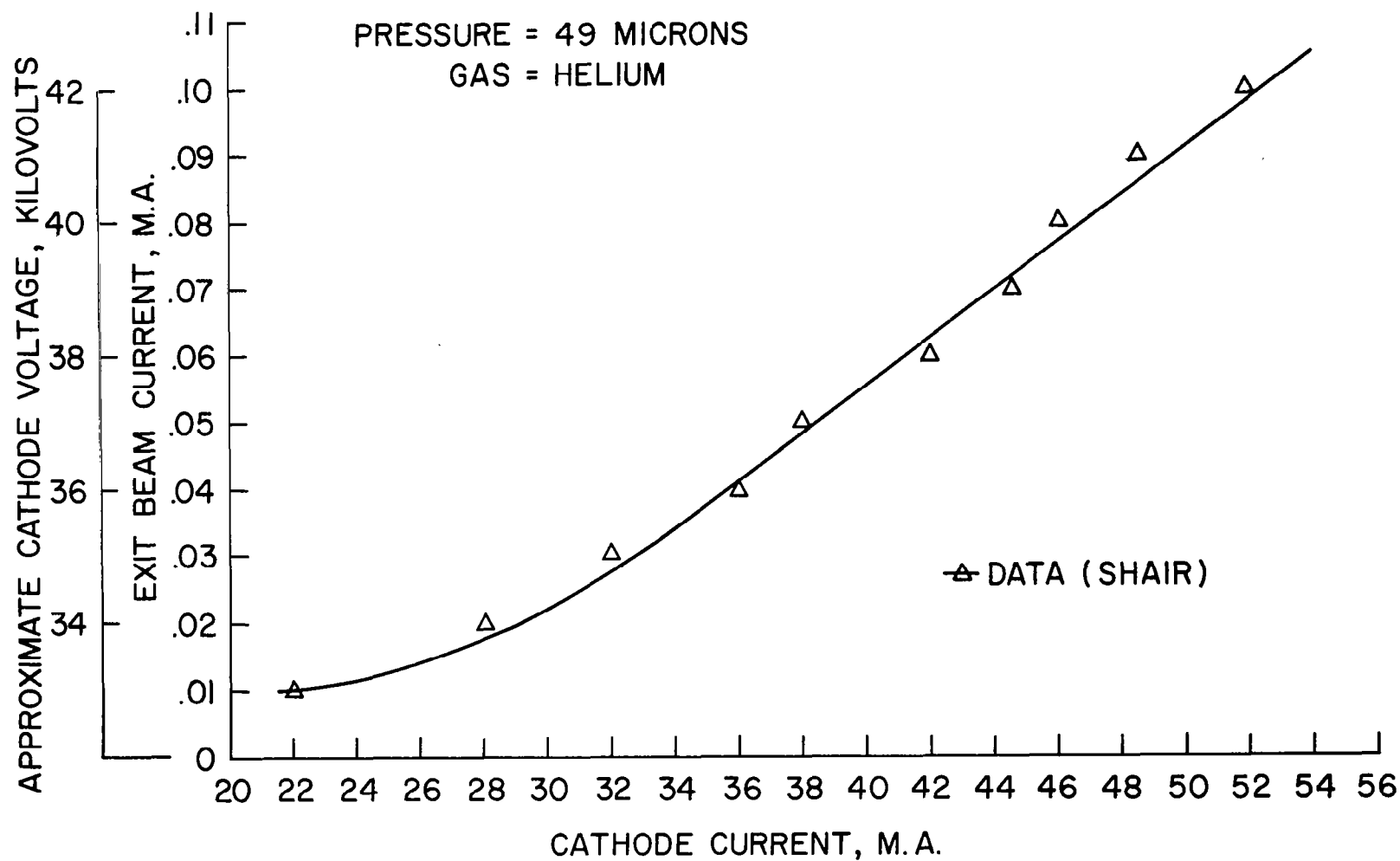


Figure 28. Calibration of Exit Electron Beam

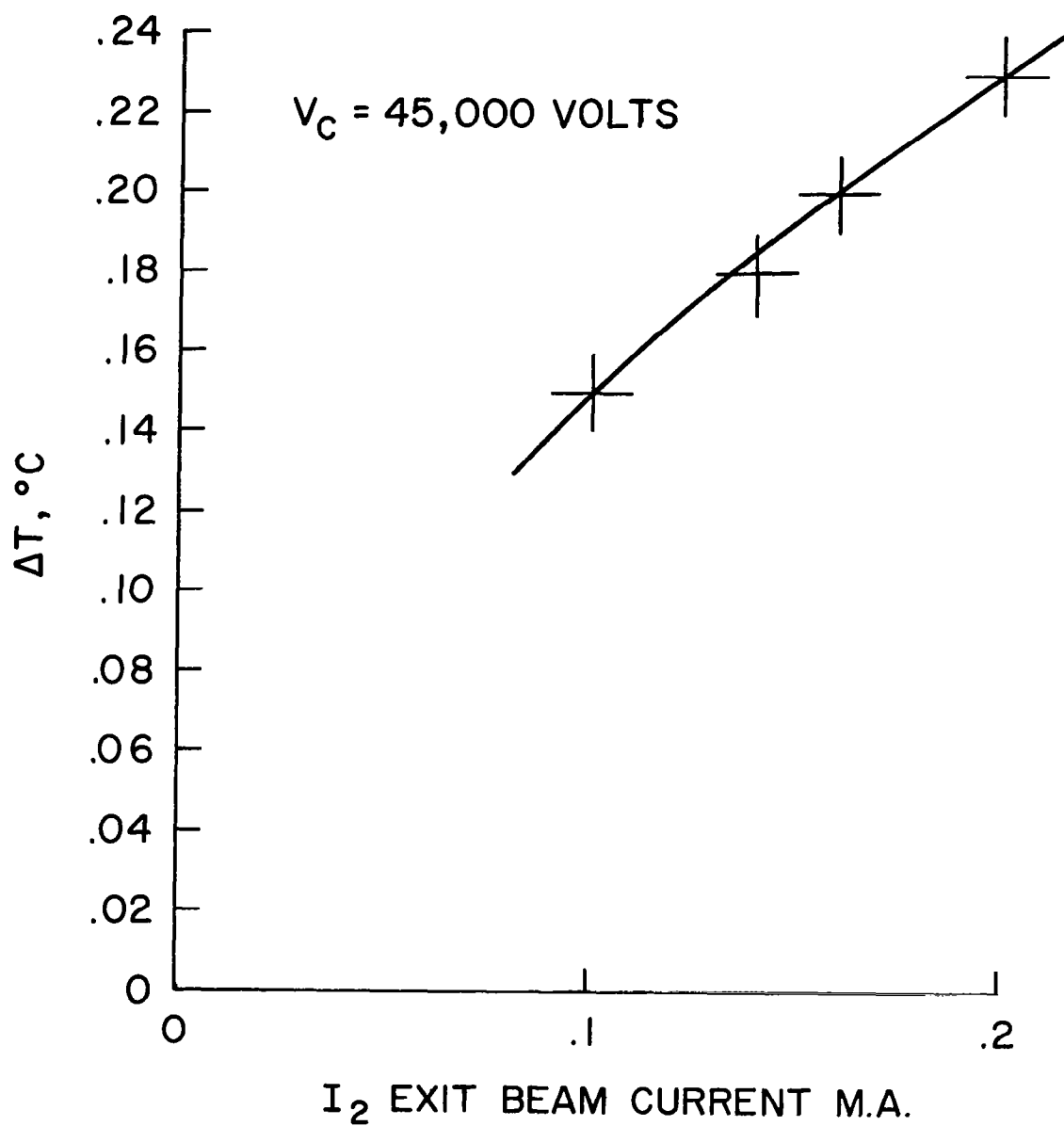


Figure 29.  $\Delta T$  vs  $I_2$

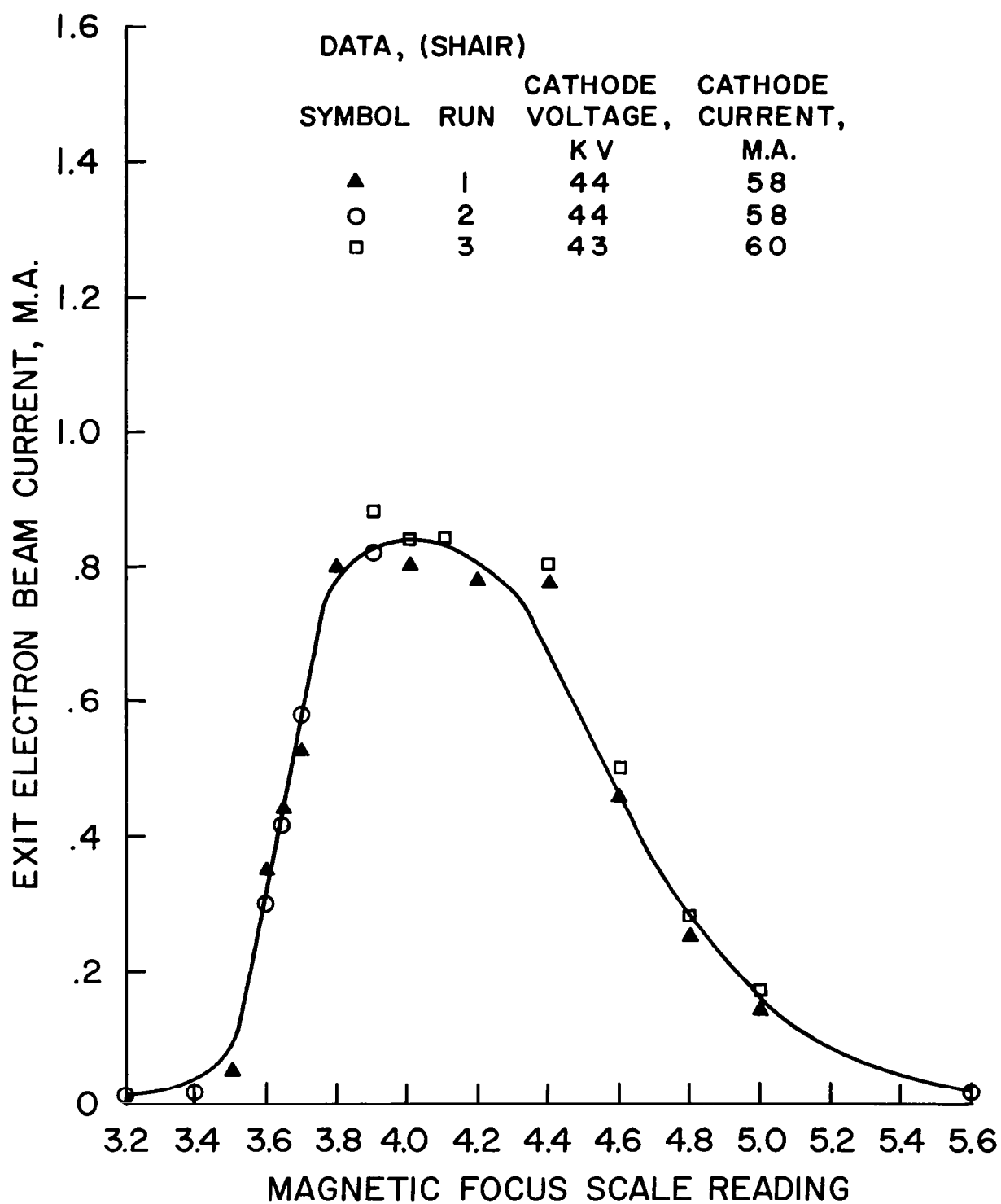


Figure 30. Exit Electron Beam Current vs Magnetic Focus Scale Reading

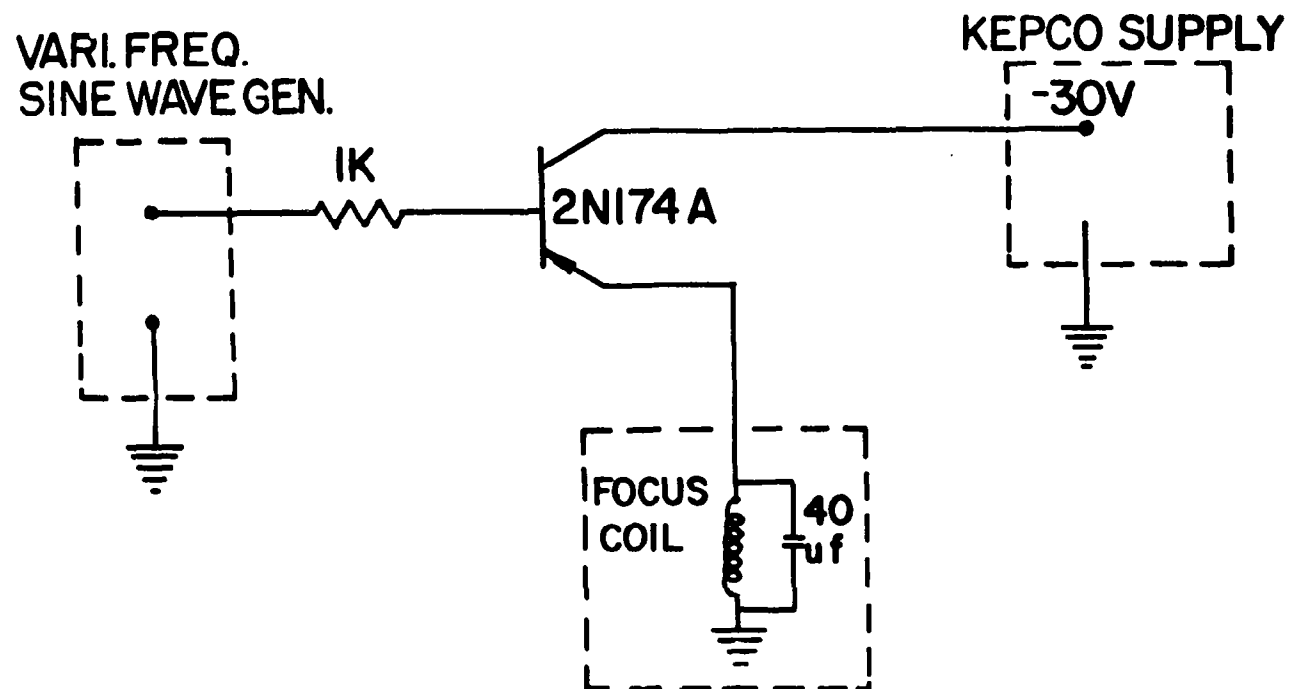
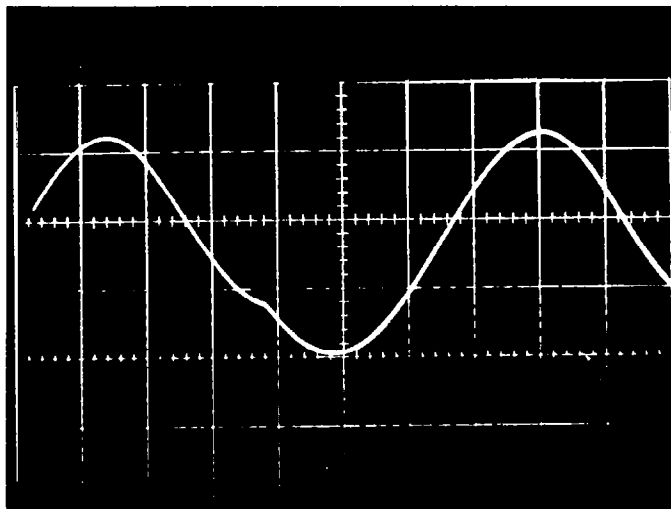
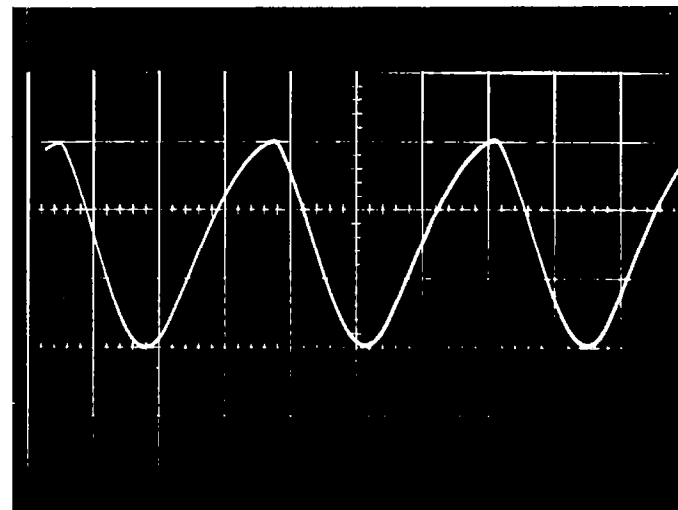


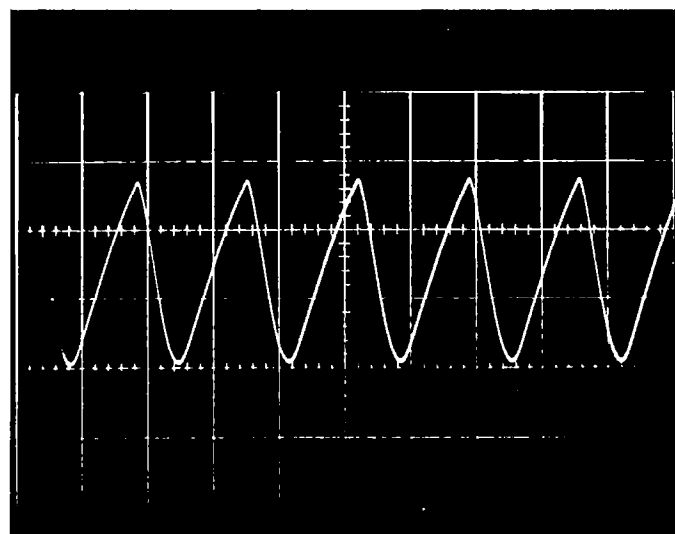
Figure 31. Electron Beam Modulator CKT



a)



b)



c)

Figure 32. Oscilloscope Wave Forms of Voltage Delivered to Electron Beam Magnetic Focus



#### D. MICROWAVE INTERFEROMETER

A two-station 60 KMC microwave interferometer, (with a distance of  $\sim 138$  cm between the two stations), was attached to the M-4 MGD facility in order to independently measure electron densities at positions on either side of the magnetic field region (see Figures 33 and 34). The electron temperature may be estimated from the Saha equation and the measured electron density; the electrical conductivity may then be calculated from the scalar conductivity expression once the collision frequency is calculated.

The use of the microwave interferometer to measure the electron density of a plasma has been discussed by several authors, including Ernst (Reference 21), Jahn (Reference 22) and Wharton and Slager (Reference 23); thus only a brief discussion will be presented. Assuming plane electromagnetic waves of frequency,  $\omega$ , incident on a plasma slab of thickness,  $d$ , the total phase change of the transmitted wave through the plasma is given by

$$\Delta\phi = \frac{\omega}{c} d \left[ 1 - \left( 1 - \frac{\omega_p^2}{\omega^2} \right)^{1/2} \right] \quad (13)$$

where  $c$  is the velocity of light

$$\omega_p = \frac{4\pi e^2 n_e}{m_e}, \text{ the plasma frequency} \quad (14)$$

Solving Equations (13) and (14) for  $n_e$

$$n_e = \frac{\Delta\phi}{d} \frac{m_e c}{4\pi e^2} \left( 2\omega - \frac{\Delta\phi}{d} c \right) \quad (15)$$

For a 60 KMC interferometer the cut-off electron density is  $\sim 4.5 \times 10^{13}$  electrons/cm<sup>3</sup>. The relationship between electron density and phase shift is shown graphically in Figure 35.

It is quite important that the distance between the sending and receiving horns be kept constant during the run; (a variation of distance will cause a phase shift as do variations in electron densities). Problems associated with thermal expansion during the run (causing the horns to move apart, have been solved by various clamps and by water cooling the supports.

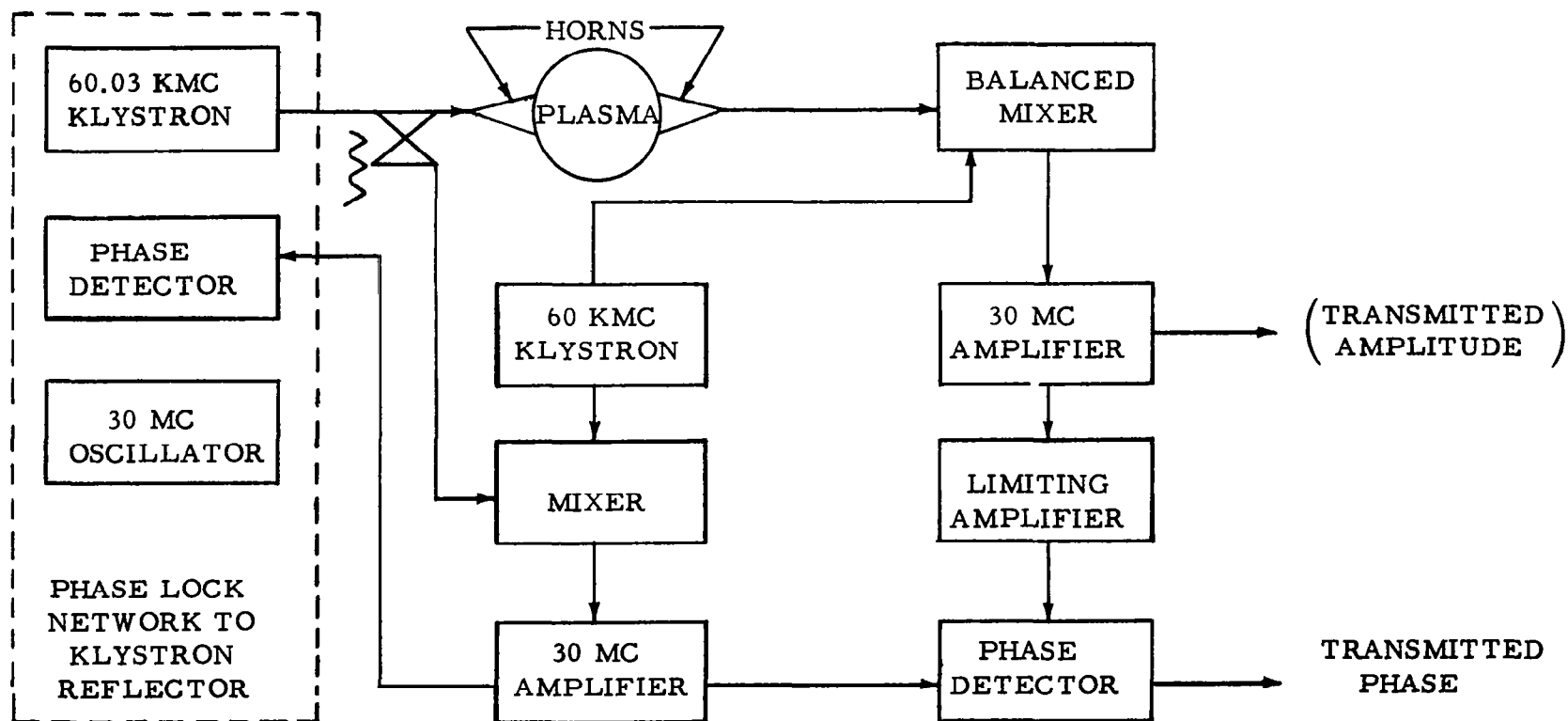


Figure 33. 60 KMC Microwave Probe

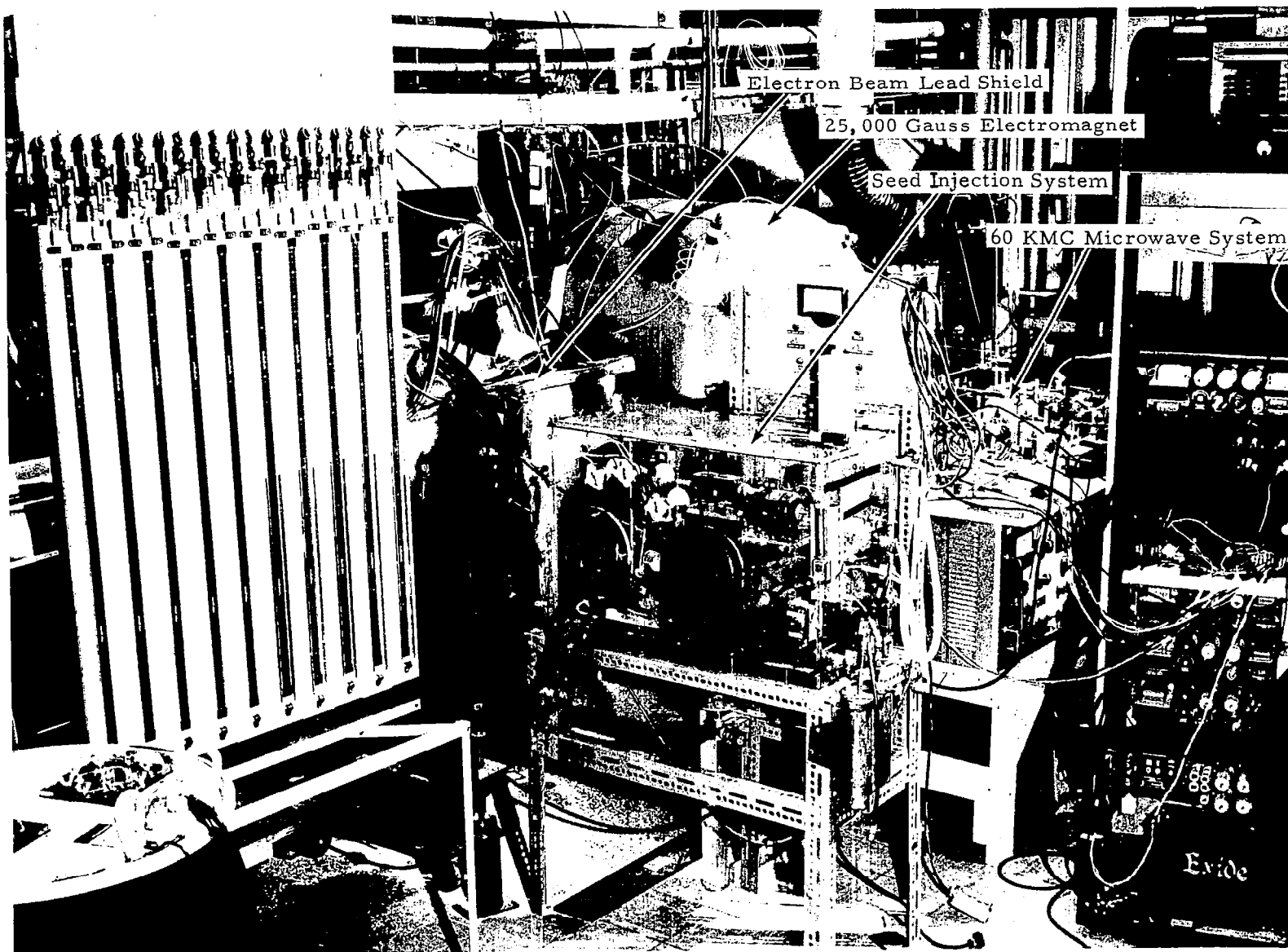


Figure 34. Upstream Region of M-4

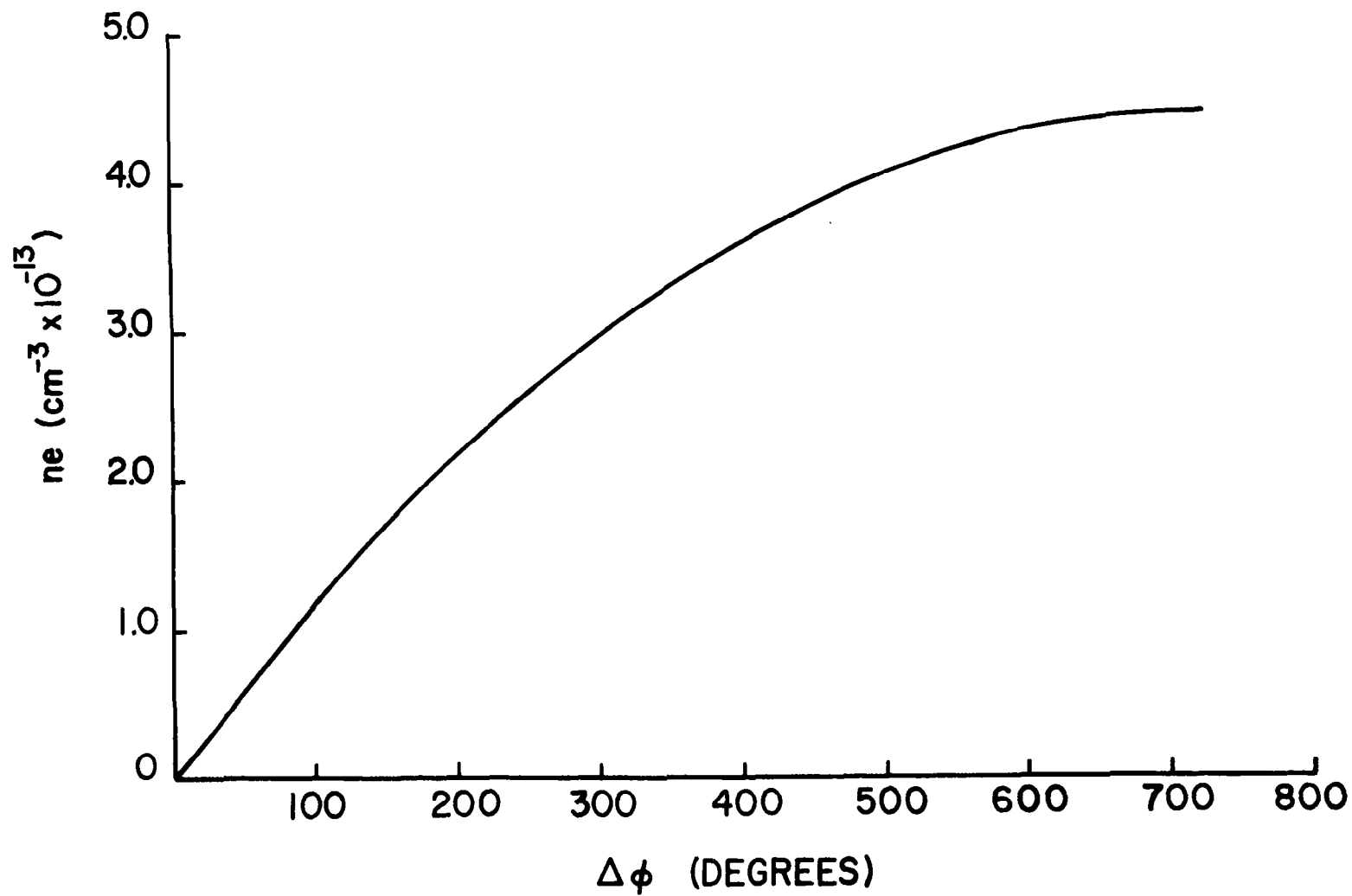


Figure 35. Electron Density vs. Phase Change (60 kMc, 1.0 cm Plasma)

A small jet of cool gas was found to adequately cool the microwave ports enough to keep the silver solder in the horns from melting. Laminated layers of dense aluminum oxide discs were cemented together to provide a barrier to cracks which result from the thermal gradients during full scale tests. Dense alumina, amounting to around 1/2" in total thickness between the horns, was found not to attenuate appreciably 60 KMC waves.

#### E. TEST SECTION

Early test sections fabricated from porous and from medium porous alumina, permitted electrical shorting between the electrodes, and were severely damaged from thermal shock and erosion.

Test sections fabricated from GE A976 dense aluminum oxide were found to withstand the test conditions extremely well. The test section (Shown in Figure 36) has 8" sections of GE A976 channel jointed together by means of an external 20 mil molybdenum sleeve. The channel is then potted with alumina cement (Resco AA22 Cement) in a 316 stainless steel case. The inside dimensions of the rectangular duct are 1 cm x 3 cm. Cracks which developed due to thermal gradients caused no problem since the cracks are backed up with a laminated cement layer. Also, the cesium and mercury vapors do not visibly attack the dense alumina at temperatures up to 1500°K. It should be noted that the silicon dioxide content of the GE A976 dense aluminum oxide is well below 0.1%.

Electrodes which are easily fabricated, and which stand up satisfactorily under full scale MGD experiments, have been made by press-fitting a 316 stainless steel rod into a 1/16" thick disc of thoriated tungsten and then spot welding the joint. The electrode discs are 1/2" in diameter.

Other electrodes (made by spot welding a 316 stainless steel rod to 10 mil molybdenum and tungsten sheets) were 1 cm x 3 cm in dimension. Thermocouples placed on the back side showed that these electrodes (heated directly from the hot gas) followed the main gas temperature within 20°K.

Indirectly heated cathodes were fabricated and tested (see Figure 37). A typical temperature-time curve for such an electrode is shown in Figure 38. Several of these electrodes were tested to 1020°K for several hours in a glass tube filled with argon at 20°K, with no apparent damage. These were not tested in M-4 facility.

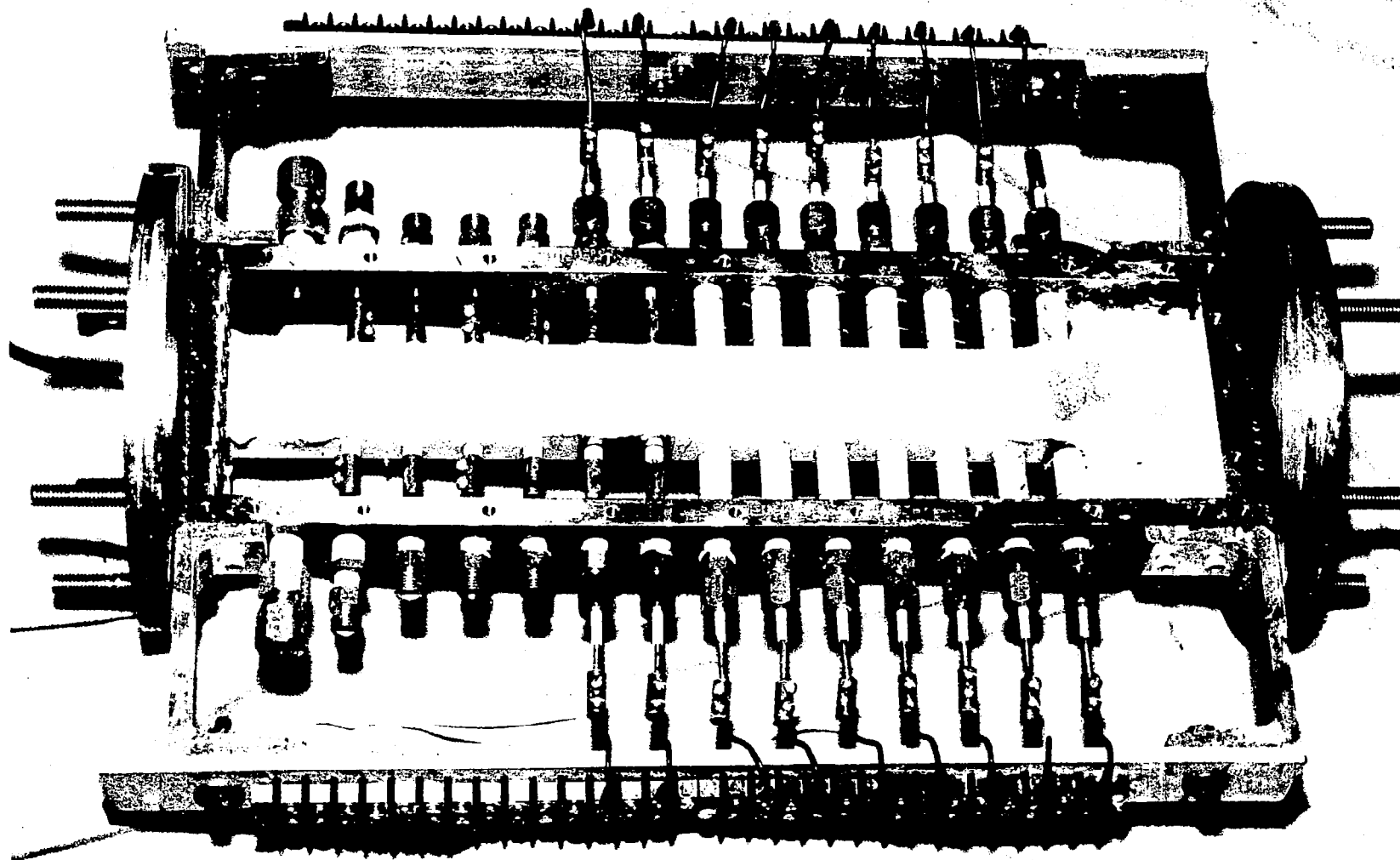


Figure 36. M-4 Test Section

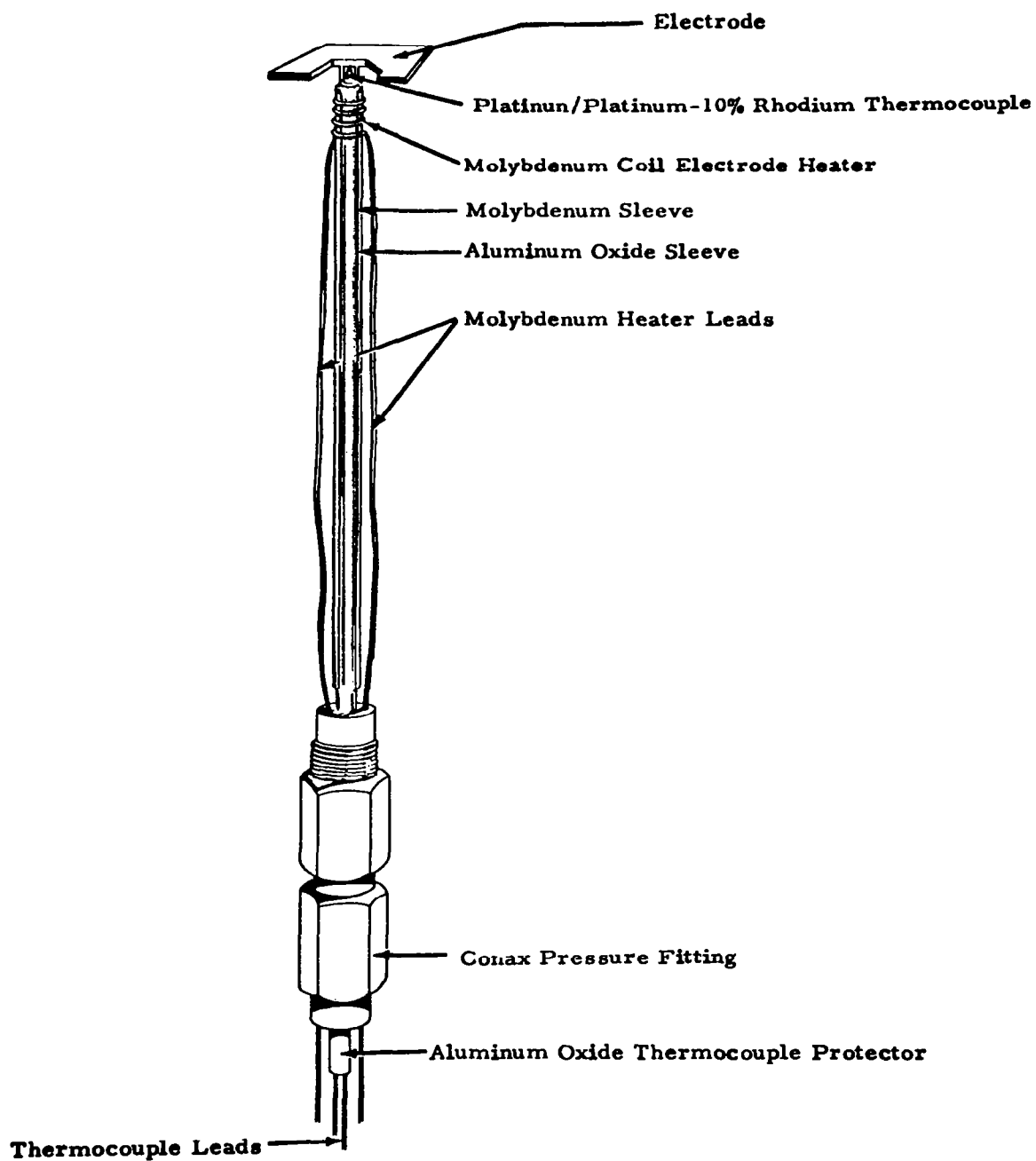


Figure 37. Indirectly Heated Electrode Note: Small Piece of Mica is Placed Between the Thermocouple Junction and the Electrode

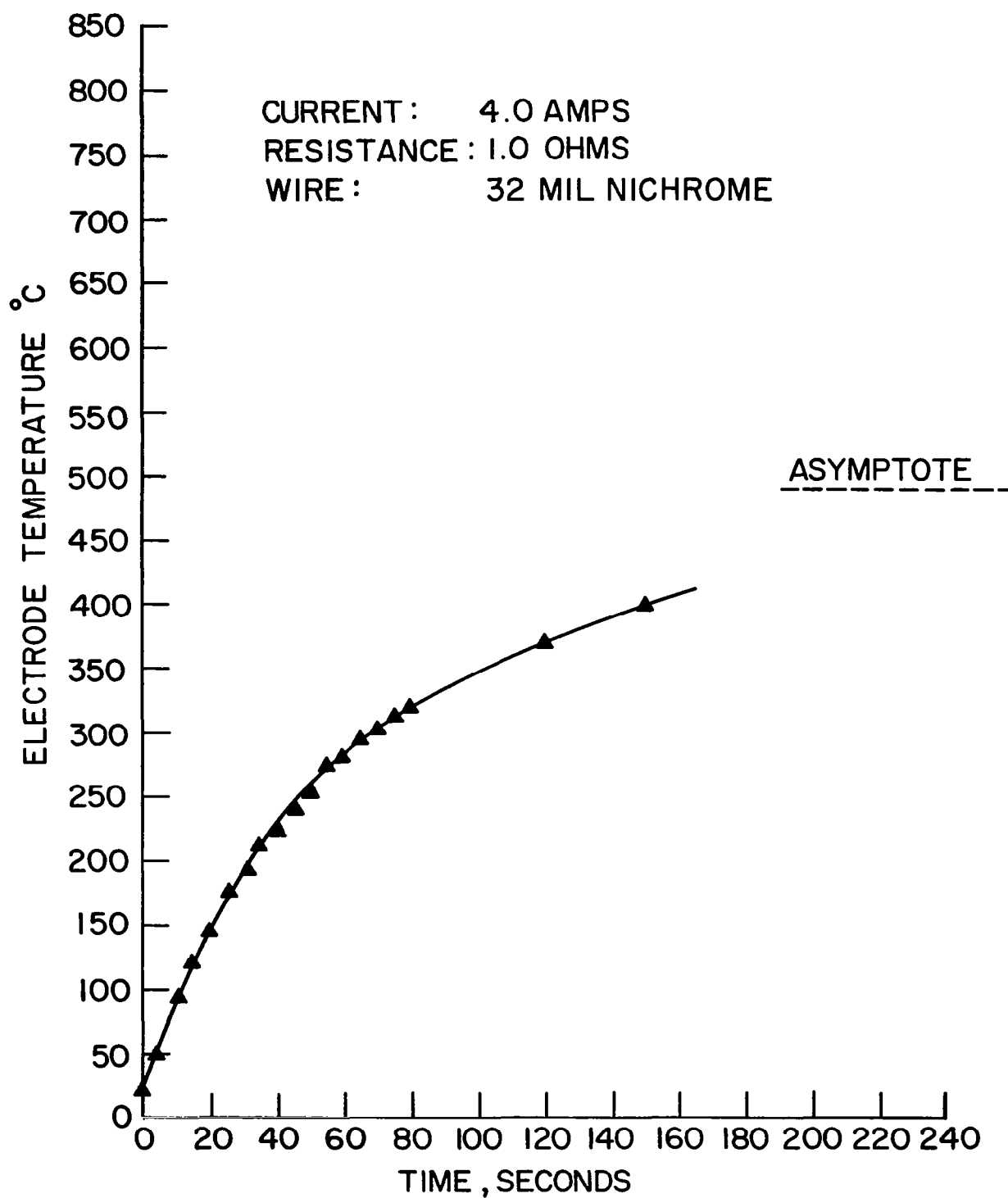


Figure 38. Temperature vs Time Curve for Indirectly Heated Electrodes



#### IV. EXPERIMENTAL RESULTS

The following experimental results, although pointing to several interesting trends, should be considered preliminary. Runs are numbered in chronological order.

##### A. ARGON SEEDED WITH CESIUM

Runs #1, #2, #3, and #4 were conducted at total temperatures  $680^{\circ}\text{K} - 900^{\circ}\text{K}$ . During the first three experiments, leakage currents from the pre-ionization electrodes were observed and no reliable MGD data were obtained. During run #4 ( $T_n = 900^{\circ}\text{K}$ ) no pre-ionization was employed and short-circuit currents  $\sim 0.2$  m.a. were generated in each of the first four electrode pairs. This short-circuit current is equivalent to an electrical conductivity of  $\sim 3.6 \times 10^{-5}$  mhos/cm. based upon the  $(UB1)_{\text{calc.}}$ . This conductivity is at least an order of magnitude higher than that predicted from the Saha equation based upon the neutral particle temperature. The operating conditions for run #4 are presented in Table 5.

TABLE 5. OPERATING CONDITIONS FOR RUN #4

Temperature at Test Section Entrance = $925^{\circ}\text{K}$
Temperature at Test Section Exit = $855^{\circ}\text{K}$
Argon Flow Rate = 1.3 gr. moles/second
Mole Fraction of Cesium Seed = $1.4 \times 10^{-3}$
Static Pressure of Argon at Test Section Entrance = 18.1 p.s.i. a.
Average Velocity in Test Section = $2.6 \times 10^4$ cm/sec.
Magnetic Field = 20,000 gauss
Maximum Short-Circuited Current = - 19 m.a. in each of first 4 electrode pairs
Equilibrium Plasma Conductivity $\sim 2 \times 10^{-4}$ mhos/cm
Inferred Plasma Conductivity from Short-Circuited Current = $3.6 \times 10^{-5}$ mhos/cm (Inferred from $(UB1)_{\text{calc}}$ )
UB1 (calculated) = 15.6 volts
$V_{\text{oc}}$ (measured) $\sim 1$ volt
Internal resistance of voltmeter $\sim 10^6$ ohms
Type of electrodes: molybdenum
Electrode Geometry: Rectangular 1 cm x 3 cm and 0.010 inches thick

During the second quarter period experiments #6 - #10 were conducted. The total gas temperature ranged from  $1150^{\circ}\text{K} - 1400^{\circ}\text{K}$ . Non-equilibrium conductivities were again observed; however, cesium attack upon the porous alumina insulators made the data invalid and impossible to reproduce. This problem was solved by designing and building the test section shown in Figure 36. During run #10, the electrodes were insulated

with dense alumina sleeves; during this run higher open circuit voltages and short circuit currents were observed. In all these runs, open circuit voltages ranged from 5% to 10% of the UBl. Similar problems have been reported by other researches, see Reference 25 for example.

Runs #11 - #15 were conducted during the third quarter period, see Table 6. In runs #11 and #12 short circuit currents indicated non-equilibrium conductivities as have been observed in previous runs. In run #12, Hall voltages were observed to be much less than those expected (see Figure 39). During the 14th experiment, the 100 ml steel syringe failed to operate and no seed was injected. However, during this run it was determined that the 0.25 mil aluminum window in the electron beam could be adequately cooled by means of external impinging jets. The steel syringe was replaced with a polypropylene syringe which has operated perfectly and completely trouble free.

During run #12, a molybdenum pitot tube was placed in the test section exit. These velocities and flow rates were consistent with those obtained by means of the rotameter readings (see Figure 40). The slightly higher values obtained from the pitot tube are due to a reduction in the flow area by the momentum boundary layer. Temperature, velocity, and Mach number time curves, are presented in Figures 41 and 42. After about 35 minutes several cracks developed in the test section which lowered the main stream velocity from 405 meters/second to 229 meters/second. This problem was eliminated in future runs by potting the test section within a strong layer of AA22 ceramic cement similar to that in the electron beam Tee-section.

Runs #16 and #17 were conducted in which both the electron beam and externally applied electrical fields were used to pre-ionize. In run #16 relative movement of the microwave horns from thermal expansion prevented any microwave data from being obtained. In run #17, at a distance 19 cm. downstream of the electron beam port an electron density  $\sim 3.0 \times 10^{12}$  electrons/cm<sup>3</sup> was measured with the microwave; this electron density corresponds to a plasma conductivity of  $\sim 5$  mhos/m.; in these calculations of the electrical conductivity, the electron-neutral collision frequency was estimated from the expression,

$$\gamma_e = \left( \frac{8kT_n}{\pi m_e} \right)^{1/2} \sum_j n_j Q_{ej},$$

where the indicated summation is only even neutral particles. The quantity  $T_n$  is the neutral particle temperature;  $m_e$  is the electron mass;  $n_j$  is the number density of the  $j^{\text{th}}$  species;  $Q_{ej}$  is the average collision cross-section for the  $j^{\text{th}}$  species. At a distance 77 cm. downstream of the electron beam port the electron density (inferred from the applied electric field and

TABLE 6

<u>Run</u>	<u>Date</u>	<u>Time Main Heater is On Minutes</u>	<u>T<sub>max</sub> °K</u>	<u>B gauss</u>	<u>U<sub>ave</sub> m/sec</u>	<u>ṁ gr/sec</u>	<u>X Mole Fraction of Seed</u>	<u>I<sub>max</sub> Measured</u>	<u>Based Upon UBl<sup>calc.</sup></u>	
									<u>σ mhos/m</u>	<u>Volts</u>
11	1-20-64	70	1180	13,800	250	54.5	$4.1 \times 10^{-3}$	~0.1 ma	$2.9 \times 10^{-3}$	10.4
12	1-24-64	90	1475	15,000	430	68.1	$3.3 \times 10^{-3}$	~4.0 ma	$6.3 \times 10^{-2}$	19.4
13	2-18-64	65	1185	21,800	600	85.5	0	-	-	39.2
14	3-2-64	60	1480	21,500	400	78.0	0	-	-	25.8
15	3-16-64	40	1440	21,500	404-229	83.4	$8.89 \times 10^{-4}$	$1.9 \times 10^{-3}$	2.4	26.1 → 14.8

Note: The maximum currents were measured at the first four electrode pairs.

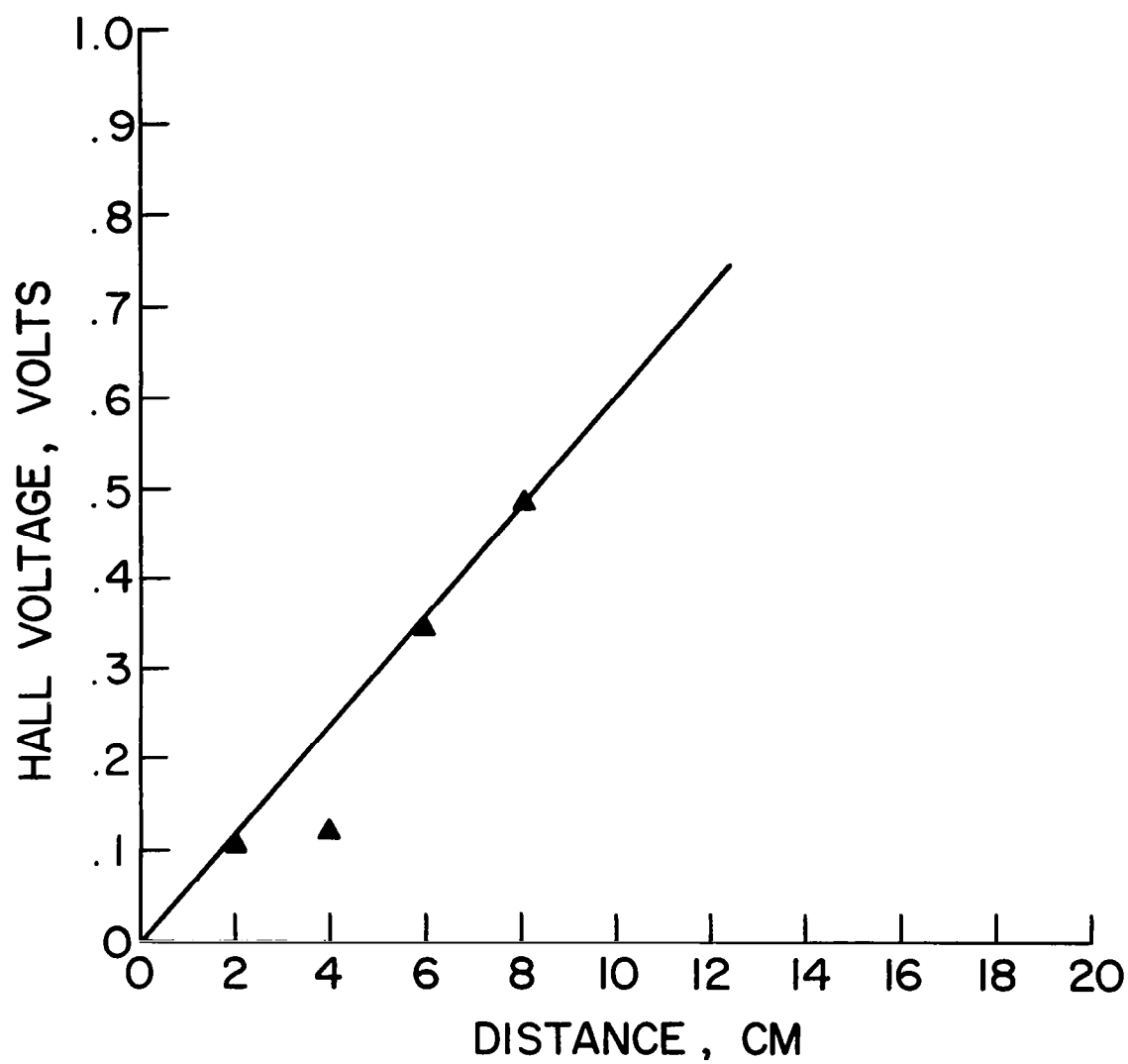


Figure 39. Hall Voltage vs. Distance for Run #12

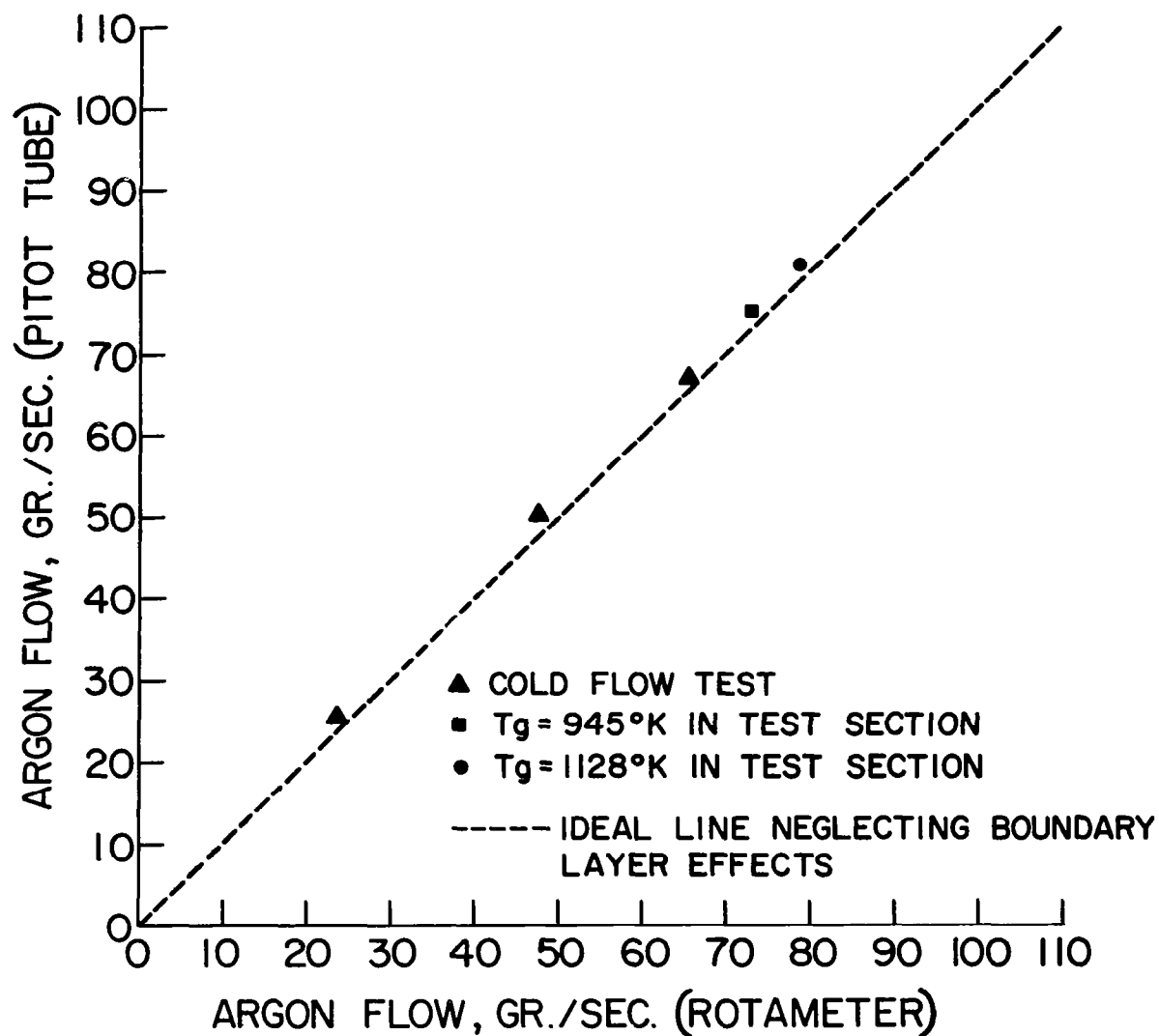


Figure 40. Consistency Check for Run #12

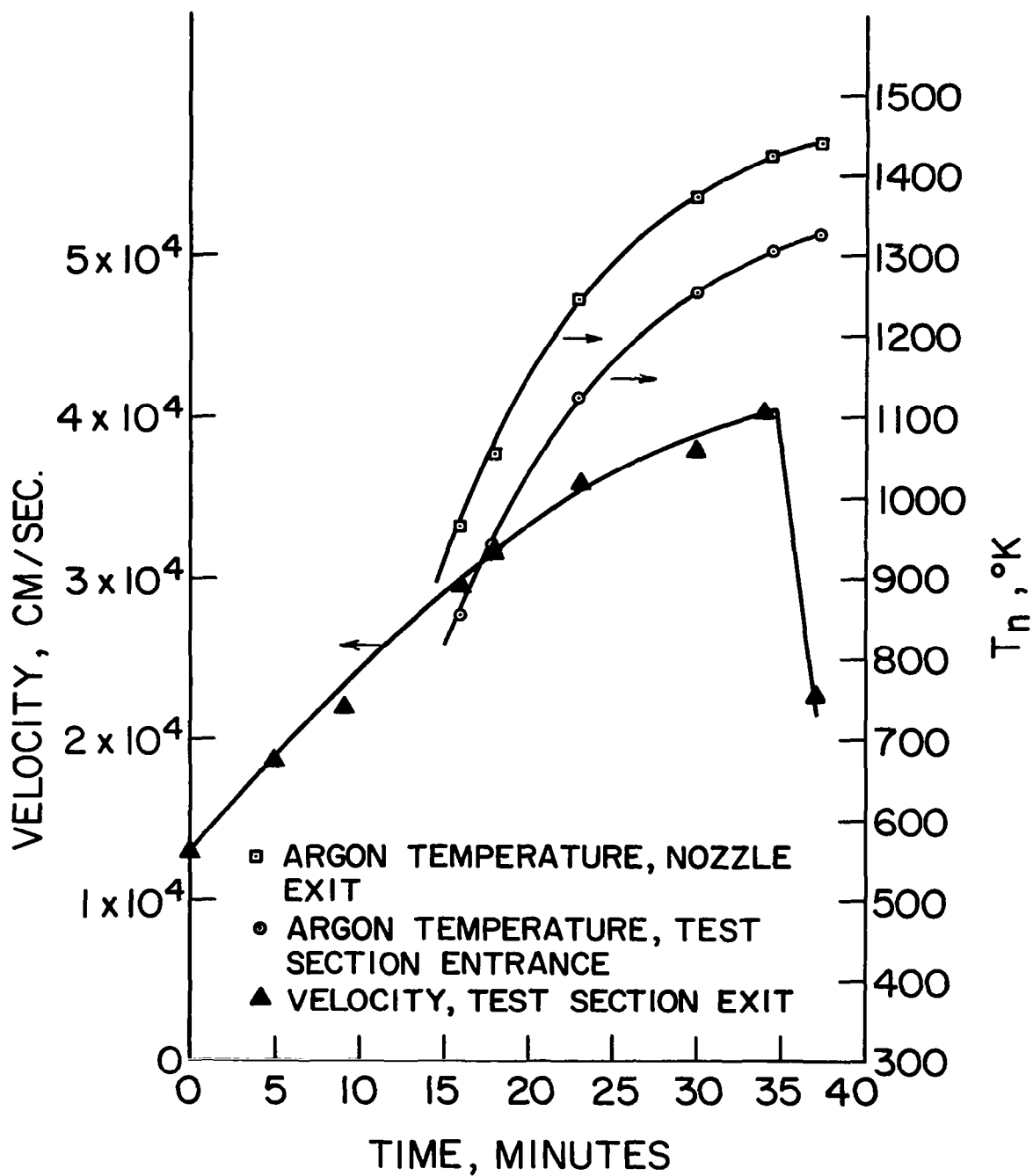


Figure 41. Velocity and Temperature vs. Time for Run #12

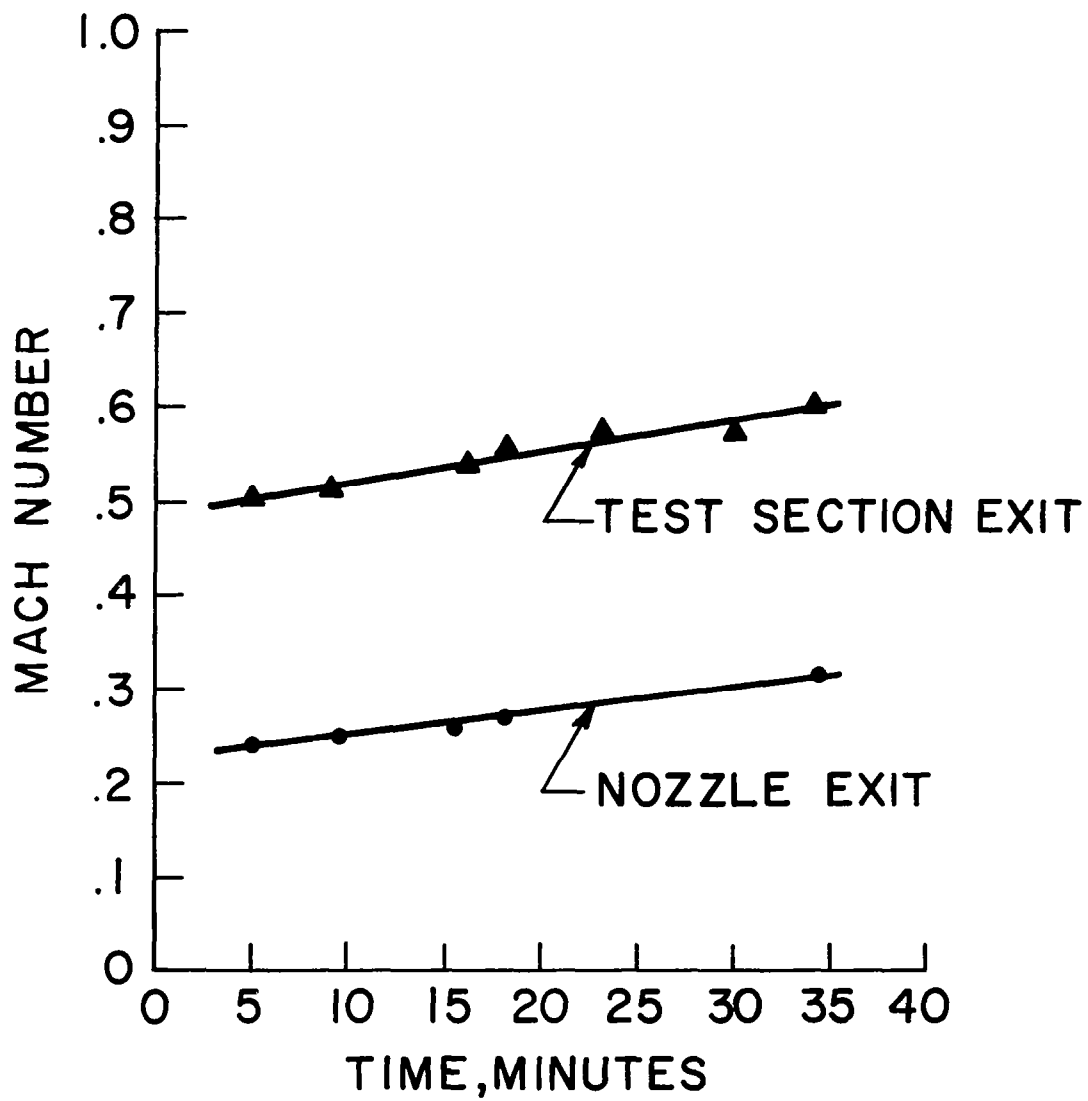


Figure 42. Mach Number vs. Time for Run #12

current value) was  $\sim 2.5 \times 10^{12}$  electron/cm<sup>3</sup> which corresponds to an electrical conductivity of  $\sim 3$  mhos/m. At a distance of 157 cm. downstream of the electron beam port an electron density was measured  $\sim 1.3 \times 10^{12}$  electrons/cm<sup>3</sup> which corresponds to an electrical conductivity of  $\sim 2$  mhos/m. The total electron "disappearance rate" closely followed a two-body volume recombination expression with the recombination coefficient  $\sim 1.5 \times 10^{-10}$  cm<sup>3</sup>/sec. The electrical conductivity at the electron beam (obtained from extrapolation of the "disappearance rate" curve) was  $\sim 6$  mhos/m; this value is in fair agreement with the 12 mhos/m calculated from the number and energy of electrons entering the duct. The net result of the pre-ionization was to create electrical conductivities within the test section which were between 50 and 100 times the Saha equilibrium value determined from the neutral particle temperature (See Figure 43). With seeding and with both pre-ionization techniques employed, open circuit voltages were increased from 1.8 volts to 7.5 volts, or from 6% to 25% of the (UB1) value. These voltages were measured on the 3rd pair of electrodes from the entrance. When the electron beam was on, open circuit voltages increased from 4.8 volts to 7.5 volts or from 16% to 25% of the (UB1) value. Using the compatibility equation developed below (Section V), the electron temperature was estimated at the first three pre-ionization electrodes and at the first generator electrode. The generated current of 8.0 m.a. (at the first generator electrode) is compatible with an electron temperature 150-200K<sup>0</sup> above the neutral particle temperature. The current passing through the plasma at the pre-ionization electrode region is "compatible" with an electron temperature  $\sim 750^{\circ}\text{K}$  greater than the neutral particle temperature.

Photographs were taken of an apparent high pressure glow discharge which appeared within the test section while both pre-ionization techniques were used during cesium seeding (see Figure 44). These pictures were taken with a Linhof 4 x 5 single lens reflex with a polaroid adapter back. The film was Polaroid type 52 with a speed of ASA 200. A 270 mm lens was used with an f number of 5.5 and an exposure time of one second. The electrodes were 2% thoriated tungsten.

Temperature-time curves for the total gas temperature are shown in Figure 9. In both experiments the electron beam was operated near 40 Kev and 50 m.a. as shown on characteristic curve in Figure 15. Under these conditions, the electron beam created electrical conductivities around 6 mhos/meter at the point of electron injection. A summary of the operating conditions and data for runs #16 and #17 is presented in Table 7. In run #17 generated currents within the test section are compatible with electron temperatures 150 -200<sup>0</sup>K above the neutral particle temperature calculated from the compatible equation in the theoretical section. Currents in the 208 A.C. pre-ionization system are compatible with electron temperatures around 750<sup>0</sup>K greater than the neutral particle temperature. In run #16 linear expansion of the MHD duct with respect to the microwave horns prevented any microwave data from being obtained.



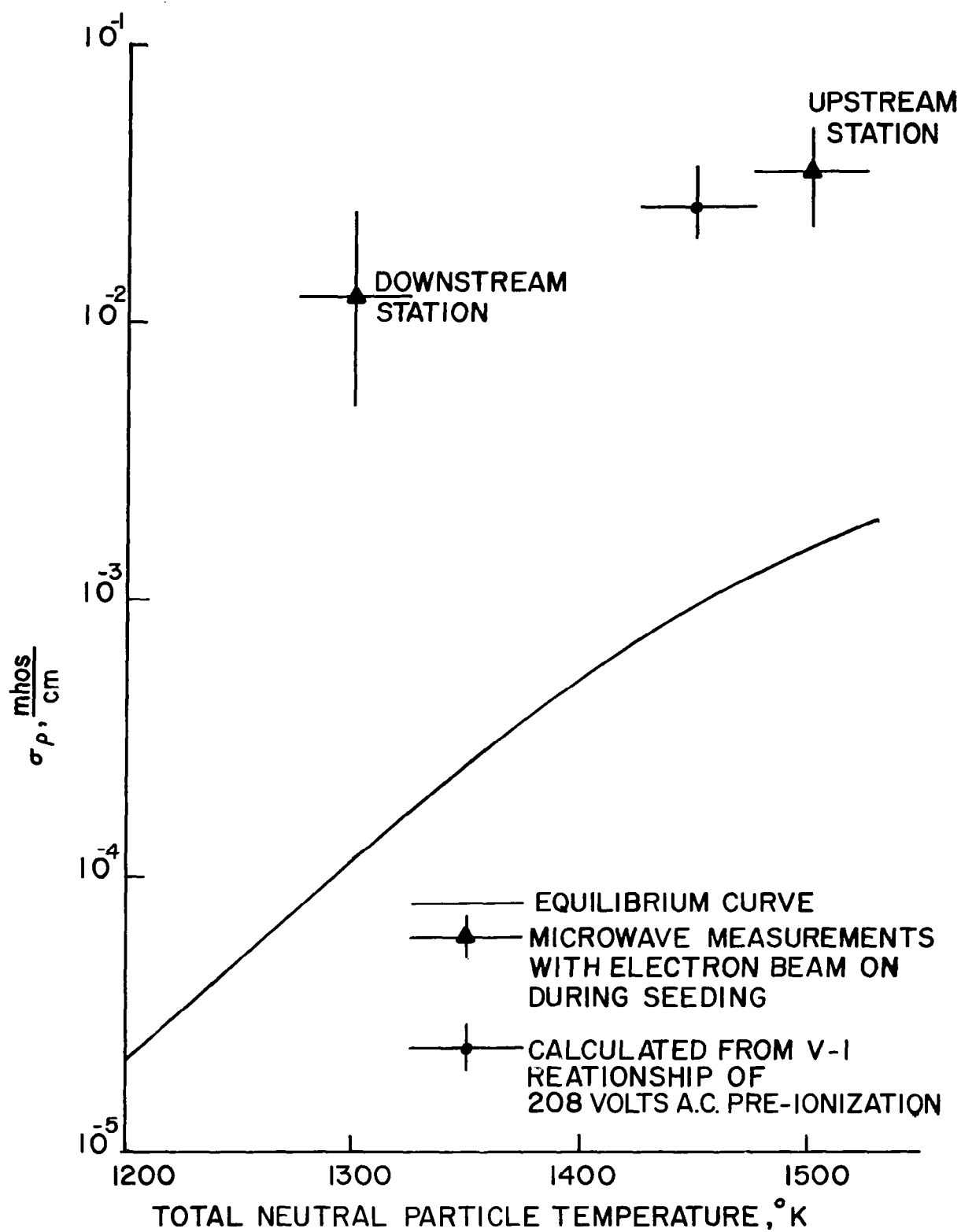


Figure 43. Conductivity Temperature Curve for Run 17

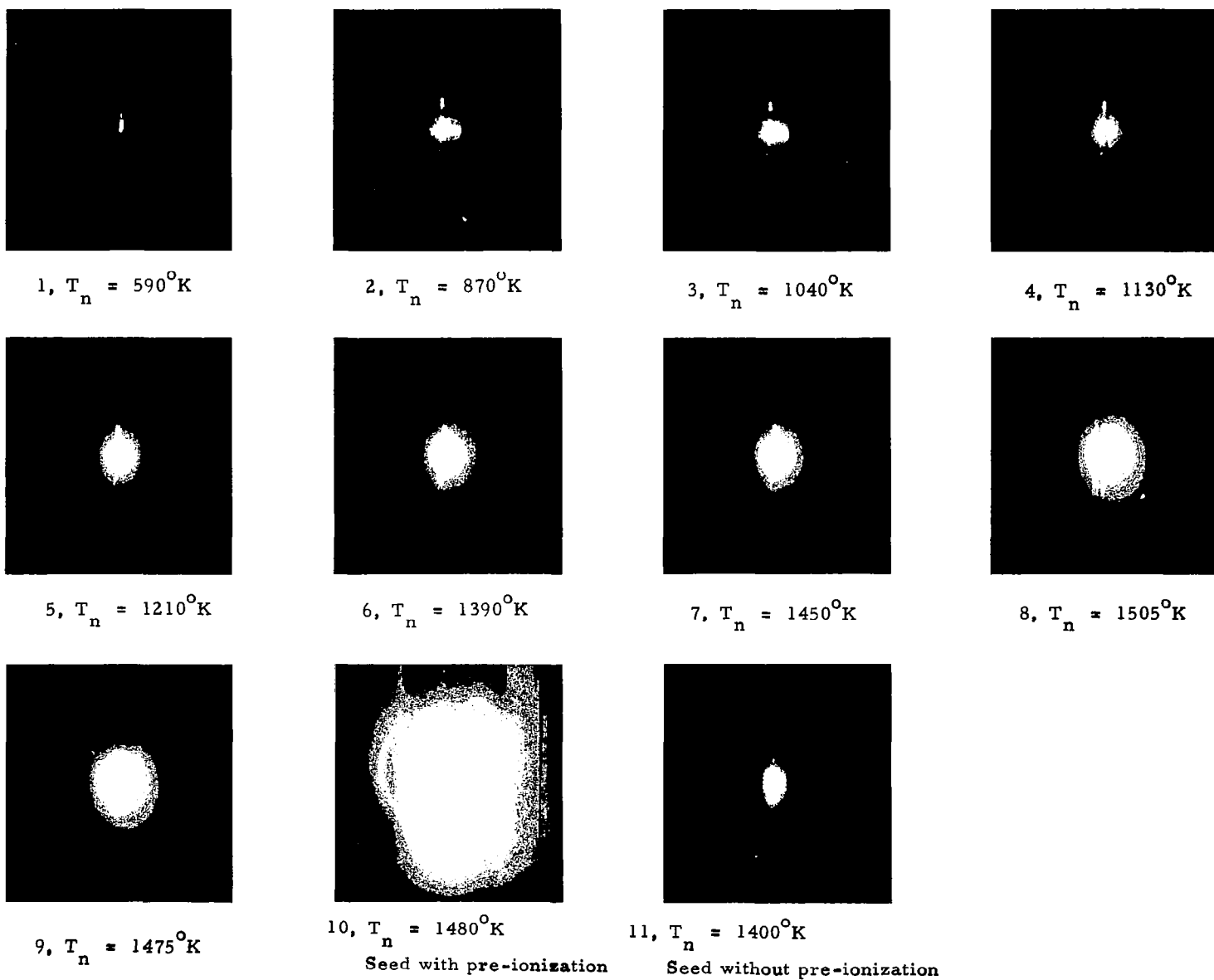


Figure 44. Photographs of MHD Duct Interior

TABLE 7

<u>Run</u>	<u>Date</u>	<u>Time Main Heater is On Minutes</u>	<u>T<sub>max</sub> °K</u>	<u>B gauss</u>	<u>U<sub>ave</sub> M/sec</u>	<u>M gr. Argon sec.</u>	<u>X Mole Fr. of Seed</u>	<u>I<sub>max</sub> Measured*</u>	<u>σ Mhos/ Meter**</u>	<u>UB1 Theory, Volts</u>
16	5-22-64	25	1340	22,000	410	65	$1 \times 10^{-3}$	--	--	27
17	6-4-64	28	1505	22,000	468	68.1	$2.9 \times 10^{-3}$	8.0 m.a.	~0.7	30

<u>Run</u>	<u>UB1 measured 208 pre-ionization w/ E-beam***</u>	<u>UB1 measured 208 pre-ionization only ***</u>	<u>UB1 measured no pre-ionization ***</u>	<u>Hall Voltage between 5th and 13th Electrodes (with 208 pre-ionization)</u>
16	~10	~10	--	~20
17	8	5	3	--

Run #17

Power input to electron beam cathode = 216 watts  
Average time from electron beam port to first microwave station = 427 μsec.  
Power input to 208 AC pre-ionization = 360 watts  
Electron temperature in generator region = ~ 1700°K  
Electron temperature in pre-ionization region = ~ 2500°K

\* I<sub>max</sub> measured with 208 pre-ionization on V<sub>pre</sub> ~ 120 Volts, I<sub>pre</sub> ~ .8 amps

\*\* σ calc. from measured open circuit voltage = 5 volts

\*\*\* measured while seeding with cesium

In run #17 the horns were rigidly attached to the channel. Although thermal expansion of the support brackets caused a phase change of the transmitted microwave signal, it was possible to estimate electron densities from the data obtained.

The total phase change, as indicated by the interferometer, was the sum of three components:

1. The increase in distance with temperature between the sending and receiving horns.
2. The increase in the length with temperature of the waveguide.
3. The increase of electron density in the MHD channel.

While it is impossible to separate the three contributing terms to the resulting total phase change during the main course of the run, it is possible to estimate the electron density induced phase change near the end of the run. When the electron beam was turned off and the seeding had stopped the total phase change decreased from  $264^\circ$  to  $240^\circ$ , indicating an electron density of  $3.0 \times 10^{12}$  electrons/cm<sup>3</sup> at the upstream station. The downstream station showed a density of  $1.3 \times 10^{12}$  electrons/cm<sup>3</sup>. Using these measured electron densities, the bounds of the plasma scalar conductivity were calculated from the possible extremes of the electron collision frequencies. At the upstream station, the scalar conductivity was between 2.3 mhos/meter and 4.9 mhos/meter. At the downstream station, the scalar conductivity was between 0.5 mhos/meter and 2.5 mhos/meter. It should be noted that these conductivities were measured with the electron beam on during seeding. The electron "disappearance rate" in run #17 closely follows a two body recombination expression with the recombination coefficient  $1.5 \times 10^{-10} \frac{\text{cm}^3}{\text{sec}}$ . This was determined from the two-body recombination expression. Not only was the open circuit voltage much less than the (UBL) value but the short circuit currents were much less than the best non-equilibrium value.

#### B. ARGON SEEDED WITH MERCURY (METASTABLE MIXTURE)

The operating conditions are presented in Table 8. The mercury attacked the aluminum foil (electron beam port) and prevented pre-ionization by means of the electron beam. A port was drilled through the Tee section to allow mercury to be injected 5 cm downstream of the electron beam injection port. After a high pressure discharge was established at the pre-ionization electrodes, the electron density at the upstream microwave position was observed to be  $\sim 10^{12}$  cm<sup>-3</sup>. This is an 8 order of magnitude

TABLE 8

Run	Date	Time Main Heater is on, Minutes	T <sub>max</sub> °K	B gauss	U <sub>ave</sub> m/sec.	. m gr./sec.	X Mole Fraction of Mercury	* I <sub>max</sub> Measure amps	σ ** mhos/meter
	7/16/64	40	1080	23,000	500	90	.01	5 x 10 <sup>-6</sup>	6

\* The low currents indicate a thermionic - limited condition. Future runs with mercury will be conducted with cesium seed also present in an attempt to reduce the work function. Heated cathodes will also be used.

\*\* Measured by means of the microwave system ~ 55 cm. upstream of an intense discharge.

increase over the Saha equilibrium value, which is  $\sim 10^4$  electrons/cm<sup>3</sup>, ( $T_{\text{gas}} \sim 1080^\circ\text{K}$ ). Calculations were performed in an attempt to reach a plausible explanation for such a large increase in electron density. The first mechanism considered, upstream diffusion of electrons from the glow discharge, was ruled out because of small values of ambipolar diffusion coefficients at pressures  $\sim 1\text{-}1/2$  atmospheres.

However, an extremely crude model involving the second mechanism, (photoionization), does predict electron densities in the order of  $6 \times 10^{13}$ .

An upper limit model was used because it lends itself to quick calculation. If the result of this calculation had produced an electron density lower than that observed, photoionization would have been ruled out as the primary mechanism. However, the upper limit model does yield electron densities upstream  $\sim 6 \times 10^{13}$  electrons/cm<sup>3</sup>. This result is a necessary, (but of course not a sufficient), condition for the photoionization mechanism to be of primary importance. However, until a better mechanism is proposed, (or until a more detailed analysis proves otherwise), photoionization will be considered the dominate mechanism. The details of the calculation follow.

#### Photoionization Model:

A certain fraction,  $\sim 10^{-2}$ , of the power fed into the pre-ionization electrodes is assumed to be converted into upstream photons possessing the mercury ionization energy of 10.39 ev. Photons, absorbed and re-emitted upstream, are assumed to be re-emitted in the upstream direction only. The channel walls are assumed to be perfect photon reflectors in the upstream direction. The number of upstreaming photons, (crossing any plane perpendicular to the flow), is assumed to be equal to the number of electrons traveling downstream, (crossing the same plane); that is, at any point the photon flux is equated to the electron flux.

#### Photon Flux:

Power into pre-ionization electrodes = (3 amps) (100 volts) =	300 watts
Power which is transferred to photons	$\sim 60$ watts
Power which is transferred to photons which possess ionization energy	$\sim 6$ watts
Power which is transferred to ionization photons which diffuse upstream	$\sim 3$ watts

From this point on, only upstream difusing photons possessing the ionization energy will be considered.

Ionization energy of mercury	= 10.39 e.v.
Cross-sectional area of duct	= 3 cm <sup>2</sup>
Gas Velocity	~ 10 <sup>4</sup> $\frac{\text{cm}}{\text{sec}}$

Thus, the photon flux is

$$(3 \text{ watts}) \left[ \frac{1 \text{ erg/second}}{10^{-7} \text{ watts}} \right] \left[ \frac{1 \text{ e.v.}}{1.6 \times 10^{-12} \text{ erg}} \right] \left( \frac{\text{photon}}{10.4 \text{ e.v.}} \right) \left( \frac{1}{3 \text{ cm}^2} \right)$$

$$= 6 \times 10^{17} \text{ photons/cm}^2 - \text{second}$$

It is interesting that this value is probably much greater than that necessary to create a population of  $6^3 \text{ P}_0$  mercury metastables greater than 1% of the total mercury atoms present, (see Reference 16).

The absorption of energy from the photon beam by the gas and its subsequent reradiation causes the intensity of the photon beam to decrease as the thickness of the gas layer traversed increases, (see Reference 15). For the entrance of N photons per second at a point distant from the beam formation into the gas the number of photons lost per second, dN, in traversing the path dX is proportional to N and to the thickness of the gas layer, dX, or  $dN = -\mu N dX$ , where the proportionality constant,  $\mu$ , is known as the absorption coefficient of the gas.

Thus,

$$N = N_0 e^{-\mu X} \quad (16)$$

Equating the photon flux to the electron flux:

$$n_e U_g = c N_0 e^{-\mu X} \quad (17)$$

where  $n_e$  is the electron density in  $\frac{\text{electrons}}{\text{cm}^3}$

$U_g$  is gas velocity in cm/seconds

$N_0$  is initial photons flux emitted from discharge in photons/cm<sup>2</sup> sec.

C is velocity of photons ~  $3 \times 10^{10}$  cm/sec

$\mu$  is absorption coefficient in cm<sup>-1</sup> =  $N_{\text{Hg}} Q$

$N_{\text{Hg}}$  is density of mercury atoms/cm<sup>3</sup>

Q is the mercury ionization cross-section, cm<sup>-2</sup>

X is distance upstream of discharge in cm

For the case  $X \sim 55$  cm,  $\mu X < 1$  since  $N_{\text{Hg}} Q \sim 10^{17} \times 10^{-19} \approx 10^{-2}$ . Note that the cross-sections for photoionization at their maximum are  $10^{-2}$  to  $10^{-3}$  that for ionization by electron or ion collision (see Reference 17).

$$n_e \approx \frac{N_o}{U_g} = \frac{\left(6 \times 10^{17} \frac{\text{photons}}{\text{cm}^2 \cdot \text{sec}}\right) \left[\frac{1 \text{ electron}}{1 \text{ photon}}\right]}{\left(10^4 \frac{\text{cm}}{\text{sec}}\right)}$$

$$n_e \sim 6 \times 10^{13} \frac{\text{electrons}}{\text{cm}^3}$$

It should be noted that precursor radiation has been observed in shock tubes as early as 1954 (see Reference 18). It should also be noted that under certain conditions photoionization can be an efficient ionization process (see Reference 19). However, if an external u.v. light is used, (the commonly used quartz window absorbs most of the photon energy below  $2000\text{\AA}$ ), thus causing the process to be fairly inefficient (see Reference 20). However, an internal glow discharge negates the necessity of quartz windows and could prove to be an attractive method for the production of a non-equilibrium condition prior to the magnetic field region of an MGD generator.



## V. THEORETICAL ANALYSIS

### A. COMPATIBILITY EQUATION FOR NON-EQUILIBRIUM IONIZATION

In order to facilitate data reduction, an expression of compatibility (independent of the electron collision frequency) was developed from the electron heating equation (discussed in Reference 4) and the Saha equation. By using this compatibility relation, one may compute the profiles of electron temperature, plasma electrical conductivity, and electric field, between the anode and cathode of moderate pressure plasma devices (such as a diode or an MGD generator), once the neutral particle temperature profile and the current density have been measured. The current passing through any plane parallel to the electrodes is assumed constant. The influence of non-uniformities due to insulator walls is neglected. Radiation losses are neglected. As a first approximation, electron diffusion is also neglected.

Starting with the electron heating equation in which very steep spatial gradients are neglected:

$$\frac{j^2}{\sigma} = n_e \nu_e \left( \frac{2m_e}{m_n} \right) \delta \left( \frac{3}{2} kT_e - \frac{3}{2} kT_n \right) \quad (18)$$

where  $j$  is the current density,  $\sigma$  is the plasma scalar electrical conductivity,  $n_e$  is the electron density,  $\nu_e$  is the electron collision frequency,  $m_e$  is the electric mass.

- $m_n$  is the average heavy particle mass  
( $2m_e/m_n$  represents the average fraction of energy loss per electron per elastic heavy particle collision)
- $\delta$  is the loss factor which accounts for inelastic collisions and radiation losses  
( $\delta$  is near unity for monatomic particles but is very large for Polyatomic particles, as discussed in Reference 5)
- $k$  is the Boltzmann constant
- $T_e$  is the average electron temperature
- $T_n$  is the average neutral particle temperature

The scalar conductivity equation is:

$$\sigma = \frac{n_e e^2}{m_e \nu_e} \quad (19)$$

where  $e$  is the electron charge.

The electron collision frequency is eliminated by combining equations (18) and (19). The resulting expression is then substituted into the Saha equation when  $n_e \ll n_s$  and when the ratio of statistical weights equals unity:

$$\frac{n_e^2}{n_s} = \left( \frac{2\pi m_e kT_e}{h^2} \right)^{3/2} e^{-E_o/kT_e} \quad (20)$$

where  $n_s$  is the number density of ionizable particles  
(In the case of a seeded plasma,  $n_s = X_s n$ . Where  $X_s$  is the mole fraction of seed in  $n_n$  neutral particles)

$h$  is the Planck constant

$E_o$  is the ionization potential

This resulting expression (the compatibility equation) is found to be:

$$j^2 = \left( \frac{3e^2 \delta}{m_n} \right) (X_s P_n) \left( \frac{T_e}{T_n} - 1 \right) \left( \frac{2\pi m_e kT_e}{h^2} \right)^{3/2} e^{-E_o/kT_e} \quad (21)$$

The ideal gas law has been assumed.

For convenience of computation, equation (21) is rearranged:

$$\frac{5040 E_o}{T_e} - \log \left( \frac{T_e}{T_n} - 1 \right) - 1.5 \log T_e = 8.05107 - \alpha \quad (22)$$

$$\text{where } \alpha \equiv \log \frac{j^2 M_n}{\delta X_s P_n}$$

$j$  is the current density in amps/cm<sup>2</sup>

$M_n$  is the average neutral particle atomic weight

$P_n$  is the static pressure, atm.

$T_n$  is the neutral particle static temperature, °K

$T_e$  is the average electron temperature, °K

$E_o$  is the ionization potential, e.v.

Consequently, when  $\alpha$  and  $T_n(x)$  are measured,  $T_e(x)$  can be computed from equation (21). (For convenience, a plot of  $T_n$  vs.  $T_e$  can be computed for various  $T_e$ ). Here,  $x$  represents the normal distance from either of the electrodes. The profile of  $T_e$  can then be used to compute  $n_e(x)$ ,  $\sigma(x)$  and  $E(x)$  between the electrodes. The more positive  $\alpha$ , the more out of equilibrium are the electrons from the heavy particles. Figure 45 shows  $T_e$  vs.  $T_n$  necessary for  $\alpha = +3$  (if  $M_n \sim 40$ ,  $X_s \sim 4 \times 10^{-3}$ , and  $P_n \sim 1$  atm, the  $j$  would be around  $0.3$  amps/cm<sup>2</sup>). It is interesting to note that the electron temperature boundary layer is usually less steep than that of the heavy particles. However, this electron temperature profile can still create a variation in the scalar conductivity, which will in turn create apparent electrical sheaths near the electrodes and thus reduce the main stream electric field. Factors which reduce  $\delta$  (such as impurities raising the value of  $\delta$ ), will make this effect more severe. Figure 46 is a typical convenient graphical representation of the compatibility equation which can be used to quickly compute  $T_e(x)$  once  $T_n(x)$  and  $\alpha$  are measured.

Figures 47 and 48 show the functional dependence of  $T_e$  and  $\frac{n_e^2}{n_s - n_e}$  upon  $\alpha$  respectively.

A corresponding expression is derived for the electron density. Recall the logarithmic form of the Saha equation:

$$\frac{5040 E_o}{T_e} - 1.5 \log T_e = 15.38274 - \log \frac{n_e^2}{n_s - n_e} \quad (23)$$

Rearranging the logarithmic form of the compatibility equation:

$$\frac{5040 E_o}{T_e} - 1.5 \log T_e = 8.05107 - \alpha + \log \left( \frac{T_e}{T_n} - 1 \right) \quad (22)$$

Using the ideal gas law:

$$n_s = .734 \times 10^{22} \frac{X_s P_n}{T_n} \quad (24)$$

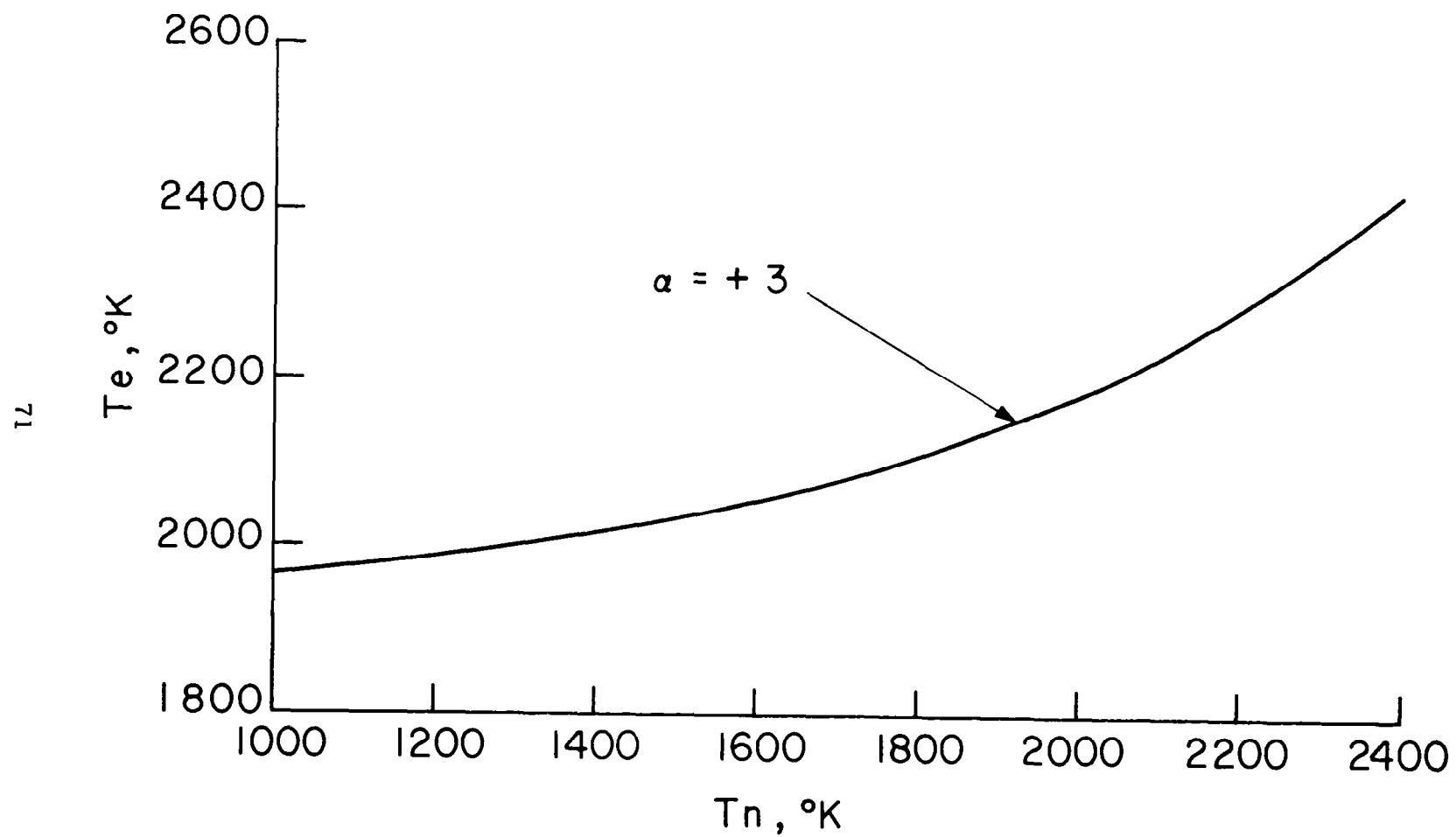


Figure 45.  $T_e$  vs.  $T_n$  for  $\alpha = +3$

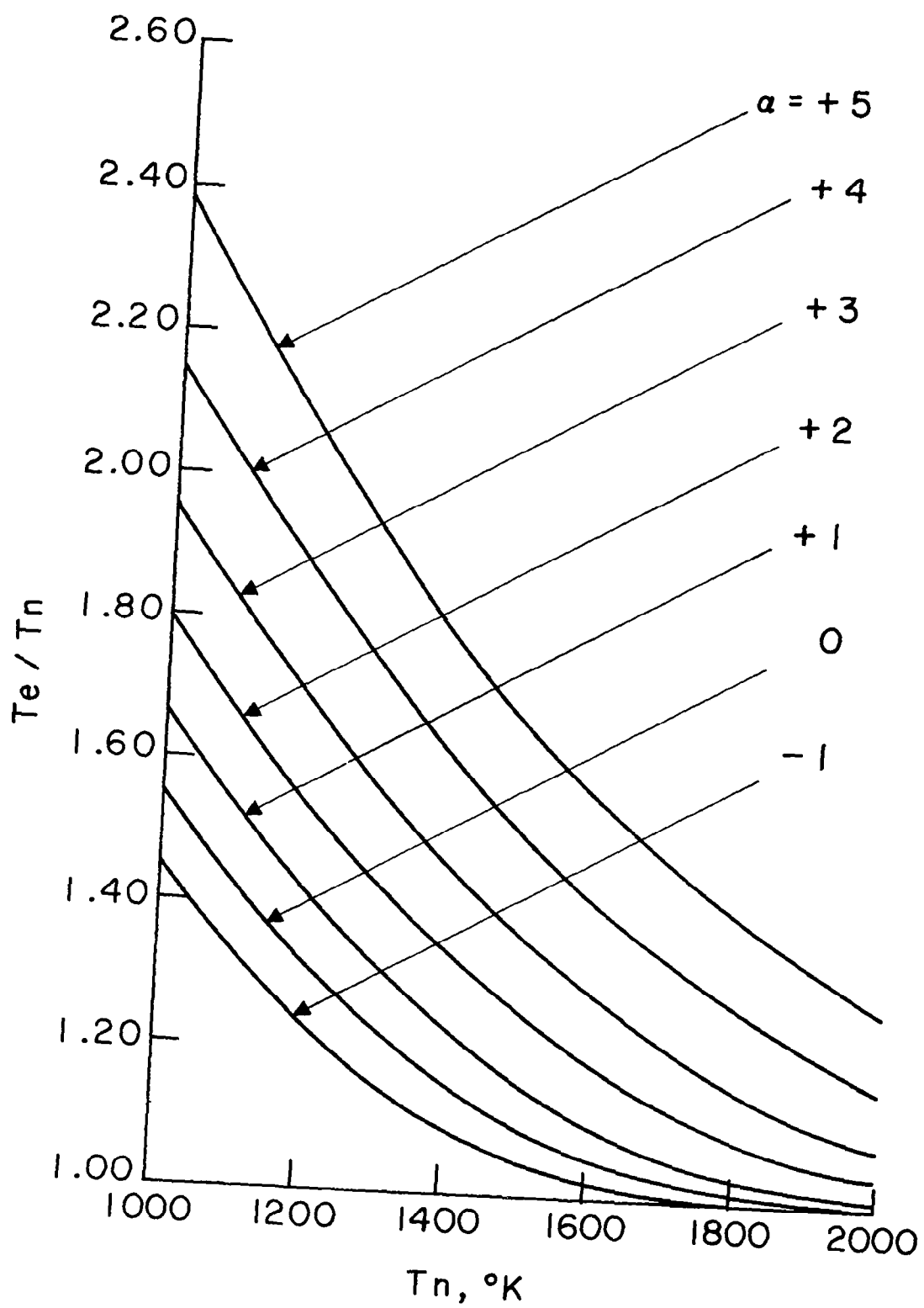


Figure 46.  $T_e/T_n$  vs.  $T_n$  for Various  $\alpha$

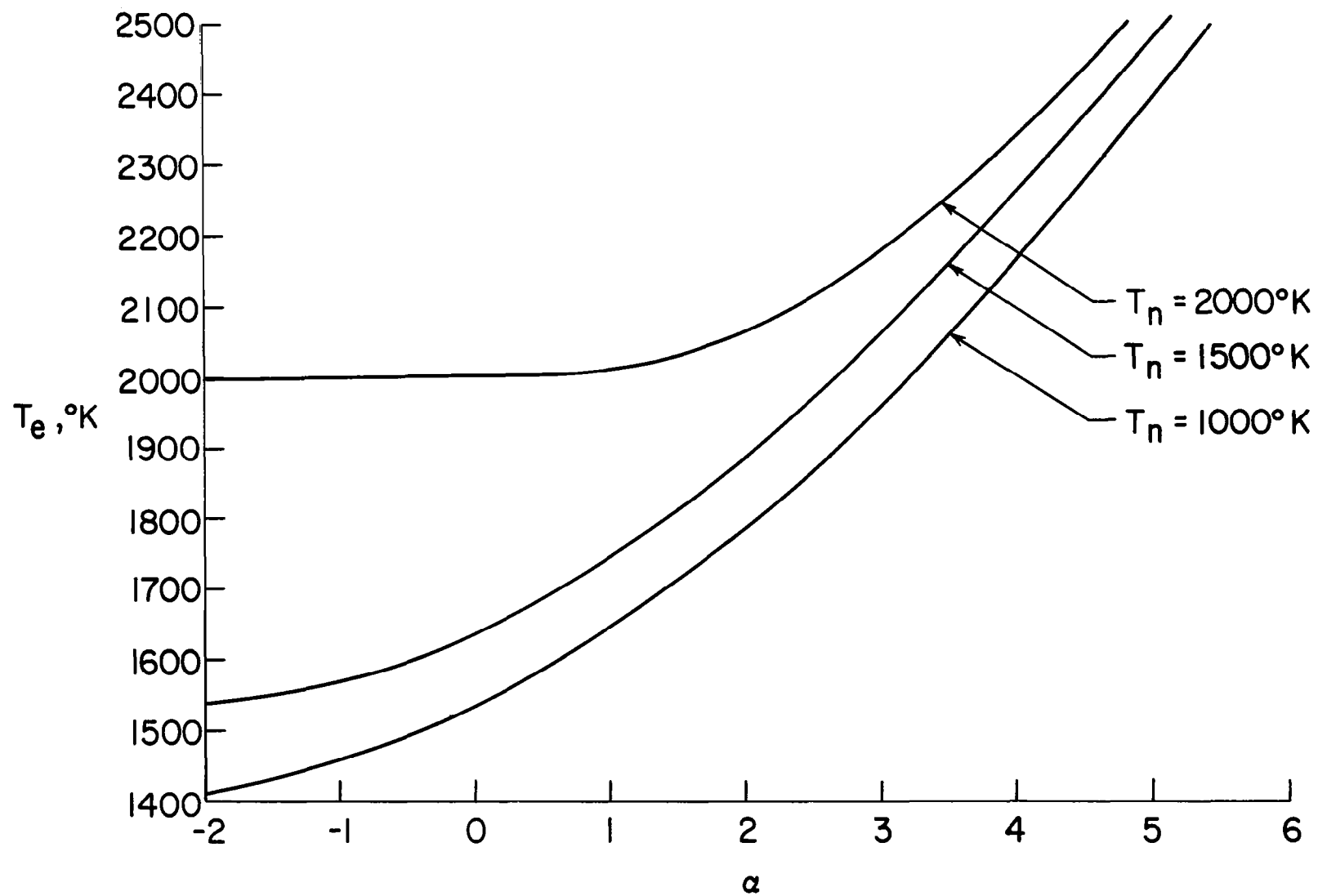


Figure 47.  $T_e$  vs.  $\alpha$  for Various  $T_n$

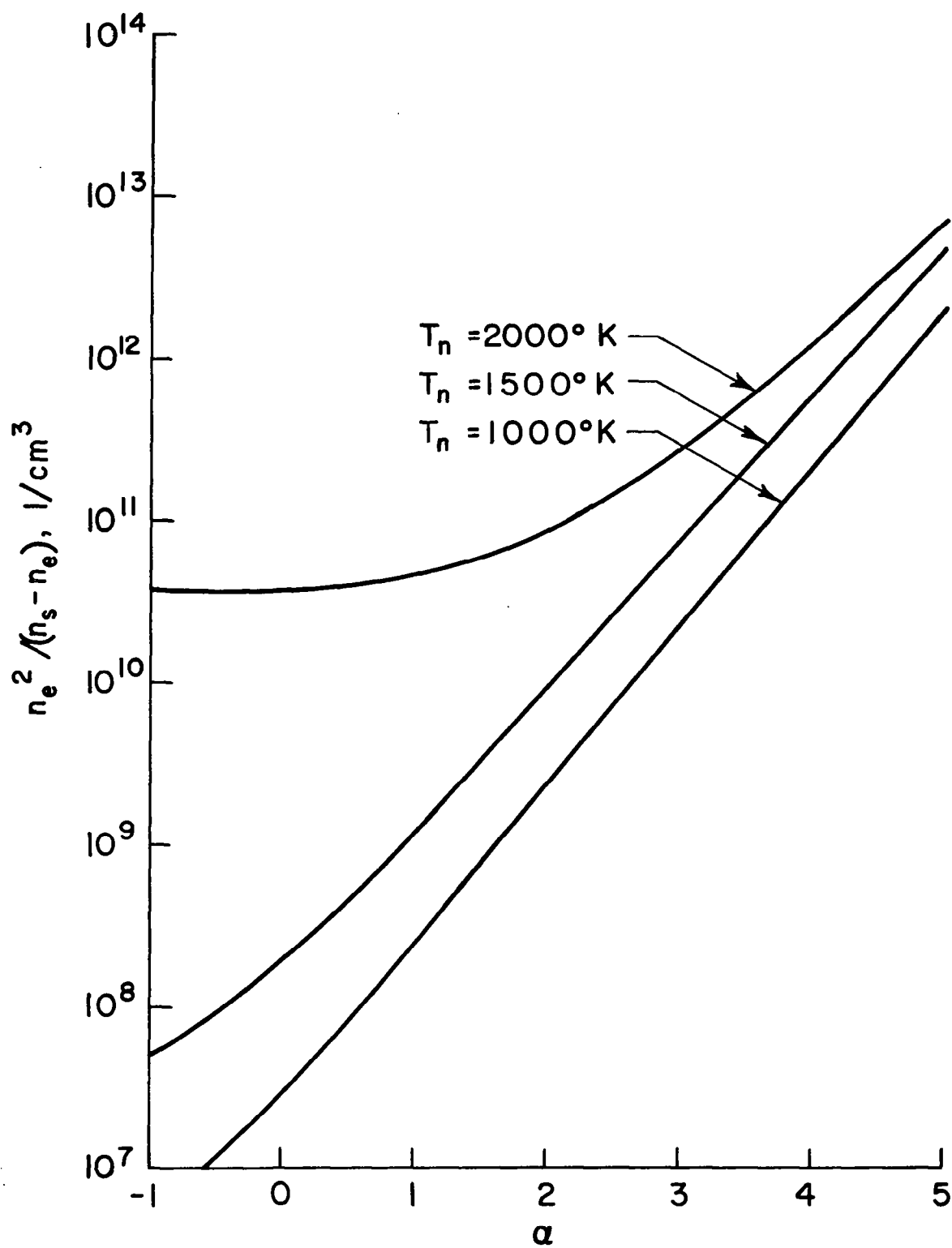


Figure 48.  $n_e^2 / (n_s - n_e)$  vs.  $\alpha$  For Various  $T_n$

and noting that

$$\alpha \equiv \log_{10} \frac{j^2 M_n}{X_s P_n}$$

Then, for the condition  $n_e \ll n_s$ , equations (22) and (23) are combined to yield:

$$n_e = 4.0 \times 10^{14} \left( \frac{j^2 M_n}{\delta T_n} \right)^{1/2} 10^{-1/2 \log \left( \frac{T_e}{T_n} - 1 \right)} \text{ #/cm}^3 \quad (25)$$

where  $j$  is in amps/cm<sup>2</sup> and  $T_n$  is in °K. For the region  $1.3 < \frac{T_e}{T_n} < 3.0$ , equation (25) can be approximated within a factor of two by the following expression.\*

$$n_e = 4.0 \times 10^{14} j \left( \frac{M_n}{T_n} \right)^{1/2}, \text{ #/cm}^3 \quad (26)$$

The plasma scalar conductivity can then be calculated from the hard sphere model in which the electrons are assumed to have a Maxwellian distribution:

$$\sigma_p = \frac{4.528 \times 10^{10} n_e}{T_e^{1/2} \sum_i n_i Q_{ei}}, \text{ mhos/cm} \quad (27)$$

where  $Q_{ei}$  is the elastic electron collision cross section for the  $i^{\text{th}}$  neutral particle species, cm<sup>2</sup>;  $T_e$  is in °K;  $n_e$  is in #/cm<sup>3</sup>;  $n_i$  is in #/cm<sup>3</sup>. Since  $X_i \equiv n_i/n_n$  and  $n_n = 0.34 \times 10^{22} \frac{P_n}{T_n}$ , from the ideal gas law,

$$\sigma_p = \frac{4.528 \times 10^{-32}}{0.734} \left( \frac{T_n n_e}{T_e^{1/2} P_n \sum_i X_i Q_{ei}} \right) \quad (28)$$

---

\* At  $\frac{T_c}{T_n} = 2$ , equation (25) reduces exactly to equation (26).



Combining equations (25) and (28):

$$\sigma_p \approx 2.47 \times 10^{-17} \frac{j}{P_n} \left( \frac{M_n T_n}{\delta T_e} \right)^{1/2} \frac{10^{-1/2 \log \left( \frac{T_e}{T_n} - 1 \right)}}{\sum_i X_i Q_{ei}} \quad (29)$$

where  $\sigma_p$  is in ohms/cm.

Consequently, the associated electric field is:

$$\frac{j}{\sigma_p} = 4.06 \times 10^{16} P_n \left( \frac{\delta T_e}{M_n T_n} \right)^{1/2} \frac{\sum_i X_i Q_{ei}}{10^{-12 \log \left( \frac{T_e}{T_n} - 1 \right)}} \quad (30)$$

For  $\frac{T_e}{T_n} = 2$ , Equation (30) reduces to:

$$\frac{j}{\sigma_p} = 5.74 \times 10^{16} P_n \left( \frac{\delta}{M_n} \right)^{1/2} \sum_i X_i Q_{ei}; \text{ volts/cm} \quad (31)$$

where  $P_n$  is in atm.,  $\delta$  is dimensionless,  $T_e$  is in  $^{\circ}\text{K}$ ,  $T_n$  is in  $^{\circ}\text{K}$ ,  $X_i$  is dimensionless,  $Q_{ei}$  is in  $\text{cm}^2$ .

## VI. CONCLUSIONS

As should be expected, the present investigations have raised more questions than answers. However, the program has resulted in the solution of some difficult technological problems as well as the determination of trends in MGD power generation. To date the following can be listed as accomplishments.

1. It has been demonstrated that a compact, reliable, resistance type heater can operate for long periods of time at gas temperatures of  $1500^{\circ}\text{K}$ .
2. It has also been demonstrated that a thin foil electron beam assembly can be adapted to a MGD facility and successfully operated.
3. The problem of the cesium attack on the porous alumina has lead to the development of a convenient, reliable test section constructed of high density alumina.
4. The data obtained, while still preliminary, has indicated that a conductivity exists in the channel that is greater than the value predicted by the Saha equilibrium value based on the neutral particle temperature and that this non-equilibrium conductivity was created by the application of the pre-ionization techniques.
5. The low open circuit voltages and short circuit currents are a troublesome mystery that does not exist in the combustion products MGD generator work. It has been demonstrated that the experimental voltages do increase with the application of the pre-ionization techniques.
6. The conductivity has been determined at three positions in the test channel and, for the argon-cesium plasma, the electron "disappearance" rate is slow. This rate follows a two-body volume recombination curve for electron densities of  $\sim 10^{12}$  electrons/cm<sup>3</sup> with the recombination coefficient of  $\sim 1.5 \times 10^{-10}$  cm<sup>3</sup>/sec.
7. Three preliminary data have shown good agreement between the microwave and electrode measurements.
8. It appears that photoionization of a metastable mixture (argon-mercury) might be an efficient way of producing a non-equilibrium plasma within an MGD generator.

9. A convenient theoretical analysis relating the current density to the electron temperature has been developed. Use of this relationship has indicated an elevated electron temperature of about 200°K within the duct.

Future work in this investigation should be aimed at the following:

1. Verification of the results obtained to date. This can be done by repeating the tests using a data recording system that simultaneously records all the pertinent information.
2. Determination of the efficiency of each preionization technique separately and together. The power into the channel from the electron beam can be increased by use of quadrapole focus technique to extend range of investigation.
3. Determination of duct size effects on open circuit voltages as well as the other parameters and the expansion of testing into the supersonic flow regime.
4. Investigation of the generation of A.C. power by the technique of preionization with an oscillating electron beam.

## VII. BIBLIOGRAPHY

1. McAdams, W. H., Heat Transmission, McGraw-Hill Book Company, Inc. New York, 1954.
2. Kreith, F., and Margolis, D., "Heat Transfer and Friction in Swirling Turbulent Flow," Heat Transfer and Fluid Mechanics Institute, Stanford University Press, Palo Alto, Calif., 1958.
3. Stauffer, L. H., and Boring, K. L., "Hollow Cathode Enhances Plasma Electron Gun," Electronics 35, No. 49, p. 60, 1962.
4. Hurwitz, H. Jr., Sutton, G. W. and Tamor, S., ARS J., 32, 1237 (1962).
5. Massey, J. and Burhop, E., Electronic and Ionic Impact Phenomena, Oxford, 1952.
6. Evans, R. D., The Atomic Nucleus, McGraw-Hill Book Co. Inc., 1955.
7. Sherman, A., ARS Journal, page 559, June 1960.
8. Lin, S. C., Resler, E. L., and Kantrowitz, A. R., J. Appl. Phys. 26, 95 (1955).
9. Spitzer, L., "Physics of Fully Ionized Gases", Interscience Publishers, Inc., N. Y., 1956.
10. Spitzer, L., and Harm, R., Phys. Rev. 89, 977 (1953); also Cohen, Spitzer, and Routly, Phys. Rev. 80, 230 (1950).
11. Chapman, S. and Cowling, T., "The Mathematical Theory of Non-Uniform Gases," University Press, Cambridge, England, 1952.
12. Allen, C. W., Astrophysical Quantities, Essential Books Press, Fairlawn, New Jersey, 1955, p. 51.
13. Phelps, A. V., Pack, J. L., Frost, L. S., Phys. Rev. 117, 470 (1960).
14. Katz, L. and Penfold, A. S., "Range-Energy Relations for Electrons and the Determination of Beta-Ray End-Point Energies by Absorption", Reviews of Modern Physics, 24, 28 (1952).

15. Cobine, J. D., Gaseous Conductors, Dover Publication Inc., New York, 1958.
16. Zito, Jr., R., "Rate Analysis of Multiple-Step Excitation in Mercury Vapor", J. of Applied Optics, May 1963.
17. Francis, Gordon, Ionization Phenomena in Gases, Academic Press Inc., New York, 1960.
18. Schreffler, G., and Christian, R. H., J. of Applied Physics 25, p. 324, 1954.
19. Maitland, A., "A Criterion for Assessing Methods of Producing Non-Equilibrium Ionization." Magnetoplasmadynamic Electrical Power Generation, I. E. E. Conference Report, Series No. 4, 1963.
20. Balfour, D., and Harris, J. H., "Photoionization in MPD Generators," I.R.D. Report 64-36 Newcastle upon Tyne 6, England, 1964.
21. Ernst, W. P., "An Electron Density Measuring System for Hot Plasma Research," Microwave Journal, p. 49, February 1961. Also AEC R&D Report MATT-47.
22. Jahn, Robert G., Physics of Fluids, 5, 678 (1962).
23. Wharton, C. B. and Slager, D. M., J. Appl. Physics, 31, 428 (1960).
24. Lindley, B. C., Brown, R. and I. R. McNab, "MPD Experiments with a Helium-Cesium Loop", presented at the International Symposium on MHD Electrical Power Generation, paper 108, page 14, (July 1964).
25. Rosa, R. J., "Nonequilibrium Ionization in MHD Generators," Proceedings of the I. E. E. E. Vol. 51, No. 5, May 1963, p. 774.
26. Kerrebrock, J. L., "Conduction in Gas with Elevated Electron Temperature," presented at the 2nd Symposium on Engineering Aspects of MHD, Philadelphia, Penna.; March 9-10, 1961.

## APPENDIX A

### PURITY OF ARGON

A typical analysis of the argon follows:

Argon	0.999,989	} 11 p.p.m. total impurity
Oxygen	0.000,003	
Hydrogen	0.000,000	
Nitrogen	0.000,006	
Carbon Dioxide	0.000,001	
Hydrocarbons	0.000,001	
Dew Point	-90°F	

The above analysis was supplied by the vendor.

The oxygen content of the argon flowing through the M-4 has been measured by means of a Beckman Oxygen Analyzer. The oxygen content of the cold gas emerging at the M-4 exit has always been between 0.6 and 2.0 p.p.m. During the beginning of an experiment, (as the system heats up), the oxygen content usually rises to ~4000 p.p.m. but then rapidly fall back to ~1 p.p.m. for the remainder of the run.

APPENDIX B  
NOZZLE COMPOSITION

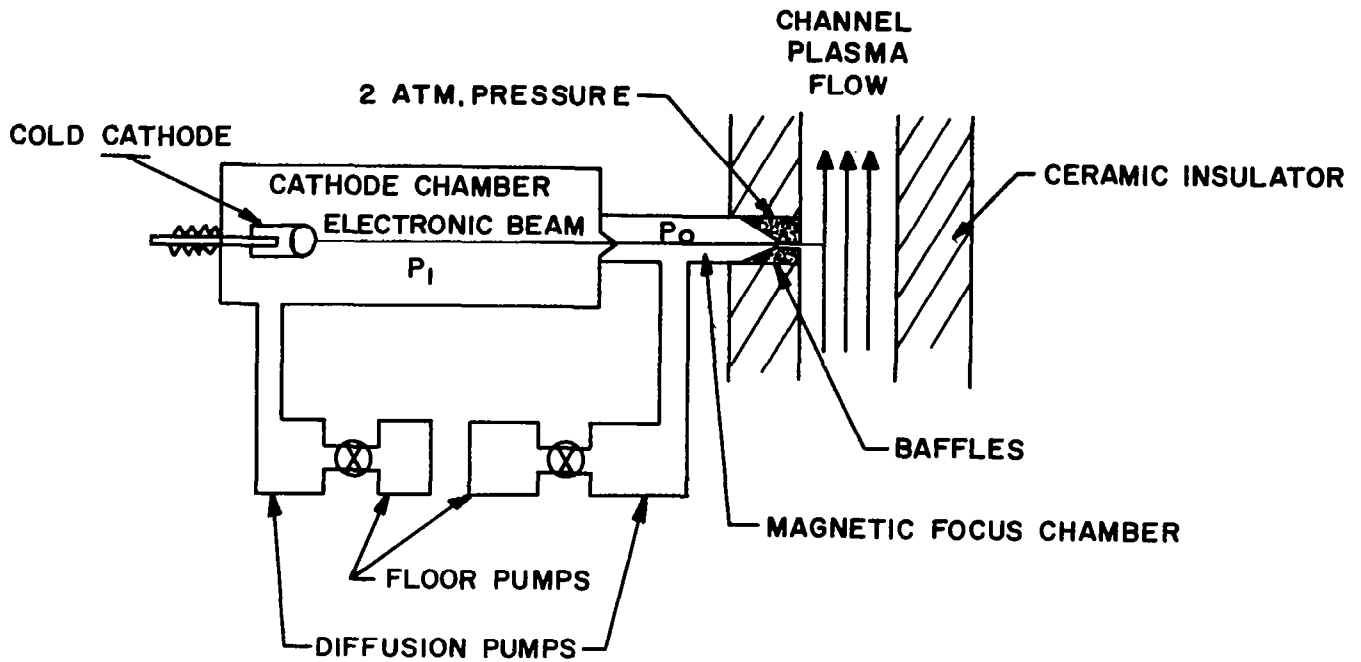
(Norton Alundum)

Aluminum	52.41%
Silicon	0.22%
Iron	0.07%
Sodium	0.07%
Oxygen	47.23%
	<hr/> 100.00%

The above are the results of chemical analysis performed by LEDOUX and COMPANY. Spectrographic analysis showed trace amounts of the following elements: Barium, Calcium, Chromium, Gallium, Lithium, Magnesium, Manganese, Nickel, Titanium, Vanadium, Zirconium, and Potassium.

## APPENDIX C PUMPING SPEED REQUIRED FOR ELECTRON BEAM DIFFERENTIAL PUMPING SYSTEM

For this system, a choked flow orifice with baffles would be differentially pumped. Argon at 2 atmospheres pressure in the nozzle tip would provide the pressure barrier, (see below):





The following flow equation is obtained from the expression for continuity, the ideal gas law, and the isentropic expansion equation:

$$\dot{m} = \frac{P_o}{T_o^{1/2}} \left[ \frac{\left( \frac{m_n \gamma g}{R} \right)}{\left( 1 + \frac{\gamma-1}{2} M^2 \right)^{\frac{\gamma+1}{\gamma-1}}} \right]^{1/2} MA \quad (32)$$

where  $\dot{m}$  is the mass flow rate of argon, #mass/sec.

$P_o$  is the static pressure in the focus chamber,  $\frac{\# \text{ force}}{\text{ft}^2}$

$T_o$  is the static temperature in the focus chamber,  $^{\circ}\text{R}$

$m_n$  is the molecular weight

$\gamma$  is the ratio of specific heats,  $CP/CV$

$g$  is  $32.17 \frac{\# \text{ mass-ft}}{\# \text{ force-sec}^2}$

$M$  is the Mach number in the nozzle

$A$  is the throat area,  $\text{ft}^2$

Equation (32) reduces to the maximum flow equation when the flow is choked at the throat.

For the case

$$m_n = 39.9 \# \text{ mass}/\# \text{ mole}; (\text{Argon})$$

$$R = 1545 \# \text{ force-ft.}/\# \text{ mole } ^{\circ}\text{R}$$

$$\gamma = 5/3$$

$$\text{then } \dot{m} = 0.662 \frac{P_o A}{T_o^{1/2}}, \# \text{ mass argon/second.}$$

For a sharp edge orifice, a correction factor must be applied. Since the exit pressure is less than 1/10, the correction factor will be taken as 0.84.

$$\text{Thus } \dot{m} = 0.556 \frac{P_o A}{T_o^{1/2}}, \# \text{ mass argon/second.}$$

One  $\text{ft}^3$  of argon at standard conditions weighs 0.111 # and contains 760,000  $\mu\text{ft}^3$ . Thus, 1 # of argon contains ~ 6,840,000 micron cubic feet.

Therefore:

$$\dot{m} = \left( 0.556 \frac{P_o A}{T_o^{1/2}} \frac{\# \text{ mass argon}}{\text{second}} \right) \left[ \frac{6,840,000 \mu \text{ft}^3}{1 \# \text{ argon}} \right] \left[ \frac{60 \text{ sec}}{\text{min.}} \right]$$

$$\dot{m} = 2.282 \times 10^8 \frac{P_o A}{T_o^{1/2}} \mu \text{ CFM}$$

Since  $1 \mu = 2.785 \times 10^{-3} \# \text{ force/ft}^2$

and  $A = \frac{\pi d^2}{4}$

$$\text{Then } \dot{m} = 5.373 \times 10^2 \frac{P_o d^2}{T_o^{1/2}} \mu \text{ CFM}$$

where  $P_o$  is in microns pressure

$d$  is diameter of orifice in cm.

$T_o$  is static temperature in chamber in  $^{\circ}\text{R}$

For  $T_o = 519^{\circ}\text{R}$ ,

$$\dot{m} = 23.57 P_o d^2 \mu \text{ CFM}$$

The pressure in the chamber behind the orifice,  $P_1$ , will be determined by the pumping speed  $S$ , (in CFM).

$$\text{Thus } P_1 = \dot{m}/S = 23.57 \frac{P_o d^2}{S} \text{ microns.}$$

For the case where  $P_o = 2 \text{ atm} = 1520 \text{ mm Hg}$   
 $d = 0.05 \text{ cm}$   
 $P_1 = .152 \text{ mm Hg}$   
 $P_o/P_1 = 10^4$

the pumping speed must be  $\sim 590 \text{ CFM}$ .

For the case where  $P_1 = .152 \text{ mm Hg}$   
 $P_2 = 1.52 \mu$   
 $d = .2 \text{ cm}$   
 $P_1/P_2 = 10^2$

the pumping speed must be  $\sim 95 \text{ CFM}$ .

Needless to say these pumping systems would be quite expensive.  
Consequently an aluminum foil window was used.

## Acknowledgment

The author wishes to acknowledge the continual help of Dr. Arthur Sherman, (manager of the MHD Power Generation Group), throughout this study.

Dr. H. E. Hall and Dr. G. W. Bethke calculated the specification of the electron beam. Dr. Hall fabricated the electron beam system from a cold cathode which was designed and built by the G. E. Advanced Technology Laboratory. Mr. A. Reuss obtained the microwave data and assisted in its reduction.

This opportunity is also taken to acknowledge the valuable help given by the machine shop and especially by Mr. George Crolus.

Thanks go to Dr. B. Zauderer, Mr. J. M. Smith, and to Dr. B. Hoffman for many interesting discussions.

And last, but certainly not least, the author wishes to thank Mr. T. Shust and Mr. S. F. D'Abbene for their assistance in conducting the experiments.

# SUMMARY REPORT DISTRIBUTION LIST FOR CONTRACT NAS3-4103

<u>ADDRESSEE</u>	<u>NUMBER OF COPIES</u>
1. NASA Headquarters FOB - 10B 600 Independence Avenue, Northeast Washington, D. C. Attention: RNT/James Lazar	2
RRE/Dr. H. Harrison	1
RNP/Dr. F. Schulman	1
RNP/Mr. J. Lynch	2
RRP/Dr. K. H. Thom	1
2. NASA-Lewis Research Center 21000 Brookpark Road Cleveland, Ohio 44135 Attention: John H. DeFord	1
J. H. Childs	1
N. John Stevens	2
Bernard Lubarsky	1
Robert English	1
L. Nichols	1
Henry Sloan	1
Reports Control Office	1
Library	2
Technology Utilization Officer	1
3. Director, Advanced Research Project Agency Pentagon Washington, D. C. 20025 Attention: Dr. John Huth	1
4. Office of Naval Research Power Branch (Code 429) Washington, D. C. 20025 Attention: Dr. Ralph Roberts	1
John Satkowski/Room 2509	1
5. Aeronautical Systems Division Flight Accessories Laboratory Wright-Patterson Air Force Base, Ohio Attention: Donald Warnock	1
6. U. S. Air Force Office of Scientific Research Washington, D. C. 20025 Attention: Dr. M. Slawsky	1

7. Aeronautical Research Associates of Princeton  
Princeton, New Jersey  
Attention: Dr. J. E. McCune 1
  
8. AVCO/Everett Research Laboratory  
2385 Revere Beach Parkway  
Everett, Massachusetts  
Attention: T. Brogan 1
  
9. Electrical Engineering Dept.  
Massachusetts Institute of Technology  
Cambridge, Massachusetts 02139  
Attention: Dr. J. Kerrebrock 1  
                  Prof. H. H. Woodson 1
  
10. MHD Research, Inc.  
1535 Monrovia Street  
Newport Beach, California  
Attention: Dr. V. H. Blackman 1
  
11. Curtiss-Wright  
Wright Aeronautical Division  
Wood-Ridge, New Jersey  
Attention: Dr. M. C. Gourdine 1
  
12. Thompson Ramo Wooldridge, Inc.  
TAPCO Group  
7209 Platt Avenue  
Cleveland, Ohio 44104  
Attention: W. C. David 1
  
13. Radio Corporation of America  
Astro Electronics Division  
Princeton, New Jersey 1
  
14. Republic Aviation Corporation  
Farmingdale, Long Island, New York  
Attention: Dr. M. S. Sodha 1
  
15. Melpar, Incorporated  
3000 Arlington Blvd.  
Falls Church, Virginia  
Attention: Dr. Roger C. Jones 1
  
16. Westinghouse Research & Development Center  
Beulah Road, Churchill Boro  
Pittsburgh, Pennsylvania  
Attention: Dr. E. V. Somers 1

17. General Atomic Division  
General Dynamics Corporation  
P. O. Box 608  
Attention: A. P. Winters 1  
San Diego, California 92112
18. Giannini Scientific Corporation  
Santa Ana, California  
Attention: Phillip J. Wyatt 1
19. Martin-Marietta Corporation  
Baltimore, Maryland 21203  
Attention: Dr. Bienert 1
20. Aerospace Corporation  
P. O. Box 95085  
Los Angeles, California 90045  
Attention: Library/Technical Documents Group 1
21. Hughes Research Labs.  
Plasma Physics Dept.  
3011 Malibu Canyon Road  
Malibu, California  
Attention: Mr. R. C. Knechtli 1
22. Stanford University  
M. E. Dept.  
Stanford, California  
Attention: Dr. R. Eustes 1
23. NASA Scientific & Technical Information Facility  
Box 5700  
Bethesda, Maryland 20014  
Attention: RQT-2448/NASA Representative 6
24. AFWL  
Kirtland AFB, New Mexico  
Attention: WLPC/Capt. C. F. Ellis 1